# Shape Reconstruction of Deposits Inside a Steam Generator Using Eddy Current Measurements

Lorenzo Audibert, Hugo Girardon, Houssem Haddar


# Shape Reconstruction of Deposits Inside a Steam Generator Using Eddy Current Measurements

**Lorenzo Audibert, Hugo Girardon , Houssem Haddar**

**RESEARCH REPORT**
**N° 9337**
April 2020
Project-Team DéFI

ISSN 0249-6399 ISRN INRIA/RR--9337--FR+ENG

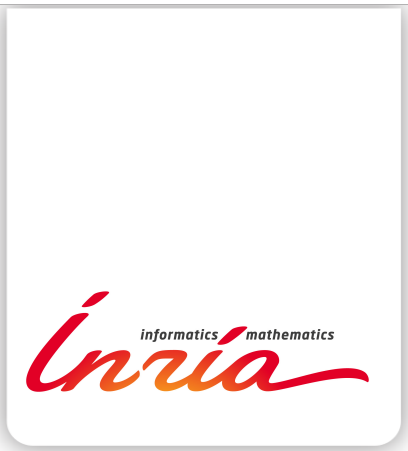


# Shape Reconstruction of Deposits Inside a Steam Generator Using Eddy Current Measurements

Lorenzo Audibert*, Hugo Girardon* †, Houssem Haddar†

Project-Team DéFI

Research Report n° 9337 — April 2020 — 61 pages

**Abstract:** Non-destructive testing is an efficient tool to assess the safety of the facilities within nuclear plants. Here we focus on the detection of clogging deposits on U-shaped tubes inside steam generators. To detect them, eddy-current probes are introduced inside the U-tubes to generate electromagnetic fields and to measure back an impedance signal. We develop a shape optimization technique with regularized gradient descent to invert these measurements and recover the deposit shape. To deal with the unknown, and possibly complex topological nature of the latter, we propose to model it using a level set function.

The methodology is first validated on synthetic axisymmetric configurations and fast convergence is ensured by careful adaptation of the gradient steps and choice of the regularization parameters. Using the actual domain, from which the acquisitions are made, we then consider a more realistic modeling that incorporates a support plate, the presence of imperfections on the tube interior and thin deposits on the tube exterior. We employ in particular an asymptotic model to take into account these imperfections and treat them as additional unknowns in our inverse problem. We shall present various numerical examples with synthetic data showing the viability of our approach. We conclude applying the algorithm on industrial data.

**Key-words:** Shape optimization, eddy currents, finite elements, non-destructive testing, level-set function

* PRISME, EDF R&D, Chatou, France
† CMAP, École Polytechnique, Palaiseau, France

**RESEARCH CENTRE**
**SACLAY – ÎLE-DE-FRANCE**

1 rue Honoré d'Estienne d'Orves
Bâtiment Alan Turing
Campus de l'École Polytechnique

# Reconstruction de dépôts à l'intérieur de générateurs de vapeur à l'aide de courants de Foucault

**Résumé :** Lors d'inspections de routines à l'intérieur de centrales nucléires, l'état des installations est le plus souvent évalué grâce à des méthodes de contrôle non-destructif. Dans le cas présent, il s'agit de détecter la présence de dépôts conducteurs colmatants sur les parois des tubes en U des générateurs de vapeur. Pour les détecter, des sondes composées de bobines à courant de Foucault sont introduites dans les tubes pour en mesurer un signal d'impédance. Nous développons un algorithme d'optimisation de forme avec descente de gradient pour inverser les mesures et retrouver la forme du dépôt. Pour gérer la topologie inconnue et possiblement complexe de la forme, nous proposons de la modéliser à l'aide d'une fonction level-set.

La méthode est dans un premier temps vérifiée sur des données synthétiques dans des cas axisymmétriques. La convergence rapide de l'algorithme est garantie grâce à un choix judicieux des pas de temps et des paramètres de régularisation. La configuration du domaine est ensuite enrichie par la présence de plaques entretoises, de dépôts fins ou d'une épaisseur de tube non constante. Nous utilisons pour les deux derniers des modèles asymptotiques pour prendre en compte ces imperfections et les traiter comme des inconnues supplémentaires à notre problème. Nous terminerons par des résultats numériques sur des données réelles fournies par EDF.

**Mots-clés :** Optimisation de forme, courants de Foucault, éléments finis, contrôle non-destructif, fonction level-set

# Contents

# 1 Context

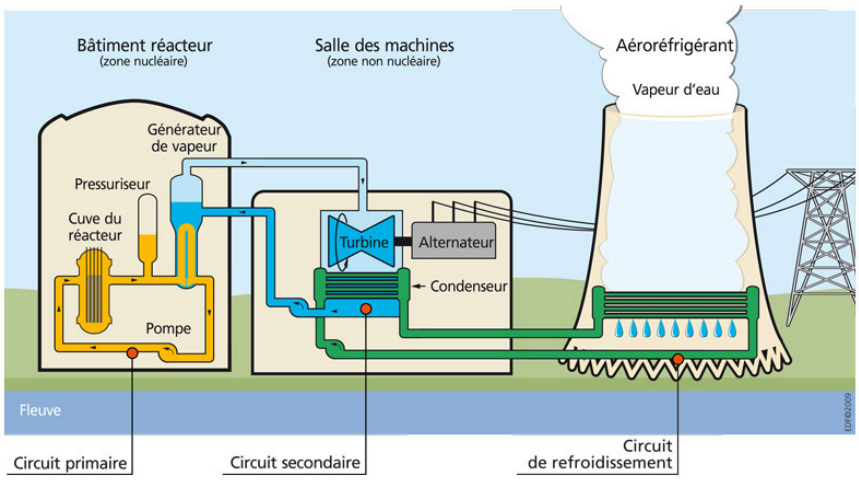


Figure 1.0.1: Schematic operation of a nuclear power plant. Source : IRSN.

Nuclear plants are thermic power stations using heat from the nuclear reaction to vaporize water in order to produce electricity. The plant is composed of three water loops to transfer the heat : the primary loop, transferring the heat from the nuclear reaction to the secondary loop, where the water is vaporized and directed to the steam turbine to produce electricity, and the cooling loop that condense the water vapor. Inside the primary loop, pressure is adapted to ensure the water remains liquid at a high temperature. Water from the cooling loop can come from two sources : a river/sea nearby with/without a cooling tower.

We focus here on the steam generator, where the first heat transfer happens : hot water form the primary loop vaporizes cool water from the secondary circuit. According to Figure 1.0.2, a steam generator consists of U-shaped tubes, where hot water flows, immersed in cool water. In contact of the hot tube wall, the cool water is vaporized and is directed upwards towards the turbine.

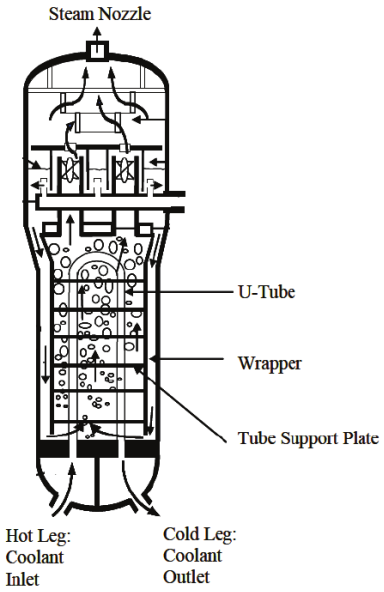


Figure 1.0.2: Sketch of the interior of a steam generator

During vaporization, small metallic conductive deposits may form on the tube wall. Due to the complexity of the steam generator and the presence of residual radioactivity, it is rather impossible to physically check the presence of such artifacts. In such cases, indirect methods such as non-destructive testing are preferred : even though they are not able to give direct information about the state of the configuration, after some processing valuable information can be obtained from it. Here we are talking about eddy-current testing, as the deposits and the tube wall both are conductive. The procedure is the following : a probe consisting of different type of coils is inserted inside the tubes. Subjected to a current, the coils create an electromagnetic field that is distorted in presence of a deposit. By measuring the flow of the distortion through the coils, we are able to derive an impedance signal containing information on the deposit shape and location.

We propose to analyse the signal through the lenses of inverse problem theory. In this paper, we consider a specific probe consisting of two axisymmetric coils (SAX probe).

# 2 Problem modelling

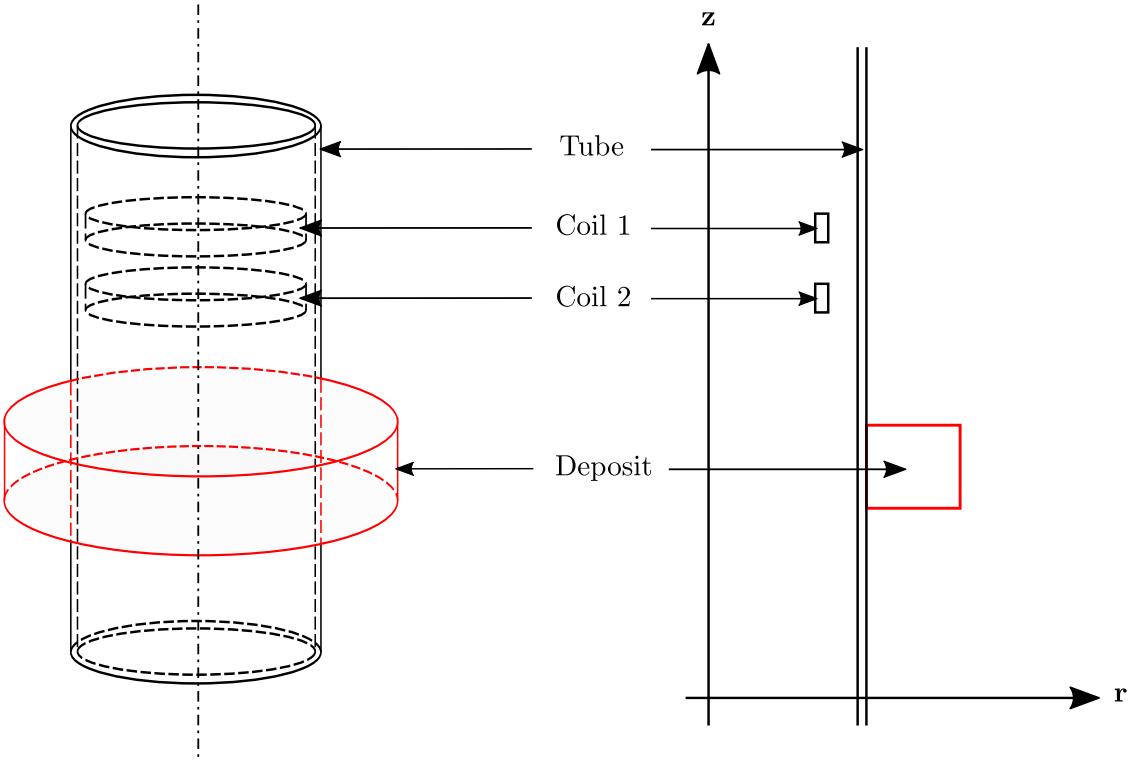


Figure 2.0.1: 3D sketch of the axisymmetric domain and its projection into 2D

Consider a current density $\mathbf{J}$ supported by two axisymmetrical coils (cf Figure 2.8.1). They generate an electromagnetic field $(\mathbf{H}, \mathbf{E})$ satisfying the 3D time-harmonic Maxwell equations :

$$\begin{cases} \mathbf{curl}\ \mathbf{H} + (i\omega\varepsilon - \sigma)\mathbf{E} = \mathbf{J} & \text{in } \mathbb{R}^3 \\ \mathbf{curl}\ \mathbf{E} - i\omega\mu\mathbf{H} = \mathbf{0} & \text{in } \mathbb{R}^3 \end{cases} \tag{2.0.1}$$

Where $\sigma$, $\mu$, $\varepsilon$ and $\omega$ are respectively the conductivity, permeability and permittivity of the medium and the pulsation. The current density $\mathbf{J}$ is supported by the coils and is divergence-free. As the coils have little impact on the electromagnetic fields, we choose to ignore their conductivities : $\sigma$ is null inside the coils.

## 2.1 Impedance signal

In order to detect the presence of deposits on the tube wall, two coils are inserted inside the tube and moved along the $z$-direction to make an impedance measurement between $z_{\min}$ and $z_{\max}$. According to [3], the impedance measured in the coil $k$ when the electromagnetic field is induced by the coil $l$ compares the flow through coil $k$ of the field in a perfect domain and the field distorted by the deposit. For a given coil position it can be rewritten as :

$$\Delta Z_{kl} = \frac{1}{I^2} \int_{\partial\Omega^{3D}_{cond}} \left(\mathbf{E}^0_l \times \mathbf{H}_k - \mathbf{E}_k \times \mathbf{H}^0_l\right) \cdot \mathbf{n}\, \mathrm{d}S \tag{2.1.1}$$

where $\mathbf{E}_l^0$ and $\mathbf{H}_l^0$ are the electromagnetic fields in the deposit-free case, with corresponding permeability and conductivity distributions $\mu^0$ and $\sigma^0$, while $\mathbf{H}_k$ and $\mathbf{E}_k$ are those in the case with conductive deposit. We note $\Omega_{cond}^{3D} = \operatorname{supp}\sigma \setminus \operatorname{supp}\sigma^0$. In the present case, $\Omega_{cond}^{3D} = \Omega_d^{3D}$, the deposit shape. Using the divergence theorem and the Maxwell equations, we also have :

$$\begin{aligned}
\Delta Z_{kl} &= \frac{1}{I^2}\int_{\Omega_d^{3D}} \operatorname{div}\left(\mathbf{E}_l^0 \times \mathbf{H}_k - \mathbf{E}_k \times \mathbf{H}_l^0\right) \mathrm{d}x \\
&= \frac{1}{I^2}\int_{\Omega_d^{3D}} \left(\mathbf{curl}\ \mathbf{E}_l^0 \cdot \mathbf{H}_k - \mathbf{E}_l^0 \cdot \mathbf{curl}\ \mathbf{H}_k - \mathbf{curl}\ \mathbf{E}_k \cdot \mathbf{H}_l^0 + \mathbf{E}_k \cdot \mathbf{curl}\ \mathbf{H}_l^0\right) \mathrm{d}x \\
&= \frac{1}{i\omega I^2}\int_{\Omega_d^{3D}} \left(\left(\frac{1}{\mu} - \frac{1}{\mu^0}\right)\mathbf{curl}\ \mathbf{E}_k \cdot \mathbf{curl}\ \mathbf{E}_l^0 - \left(i\omega(\sigma - \sigma^0) + \omega^2(\varepsilon - \varepsilon^0)\right)\mathbf{E}_k \cdot \mathbf{E}_l^0\right) \mathrm{d}x
\end{aligned}$$

where $I$ is the intensity of the current flowing in the coils. Note that the probes measure, for different pulsations $\omega$, a linear combination of different $\Delta Z_{kl}$ that we call in the following $Z$.

## 2.2 Axisymmetric geometry

To lay the basis of the inversion algorithm, we consider an axisymmetric domain as it simplifies the problem. The natural extension will be the derivation of the algorithm for non axisymmetric configurations : presence of support plates, use of different types of probes (SMX probes).

For a vector $\mathbf{a}$ in cylindrical coordinates, note $\mathbf{a}_m = a_r\mathbf{e}_r + a_z\mathbf{e}_z$, the meridian component and $\mathbf{a}_\theta = a_\theta\mathbf{e}_\theta$, the azimuthal component. Following the work of [4], 3D Maxwell equations can then be decoupled in two systems, one for $(\mathbf{H}_m, \mathbf{E}_\theta)$ and the other $(\mathbf{H}_\theta, \mathbf{E}_m)$.

If the current density $\mathbf{J}$ is axisymmetric, the second system vanishes. In the following, we consider that hypothesis valid. After substitution of $\mathbf{H}_m$, the 3D Maxwell equations can then come down to the following scalar equation verified by $E_\theta$ :

$$\partial_r\left(\frac{1}{\mu r}\partial_r(rE_\theta)\right) + \partial_z\left(\frac{1}{\mu}\partial_z E_\theta\right) + \omega^2\left(\varepsilon + i\frac{\sigma}{\omega}\right)E_\theta = -i\omega J_\theta \text{ in } \mathbb{R}_+^2 \tag{2.2.1}$$

Where $\mathbb{R}_+^2 := \{(r,z)\,/\,r > 0, z \in \mathbb{R}\}$. Due to symmetry properties, $E_{\theta|r=0} = 0$ needs to be imposed, as well as a decay condition for $r^2 + z^2 \to +\infty$.

**Notations** : On the $Orz$ plan, the tube is represented by $\Omega_t := \{(r,z) \in \Omega : r_1 < r < r_2\}$ with $0 < r_1 < r_2$ the inner and outer radius of the tube wall. We denote by $\Omega_s$ the domain inside the tube ($r < r_1$) which contains the support of the source : $\operatorname{supp} J_\theta \subset \Omega_s$. The deposit is on the tube wall that is to say $\Omega_d \subset \Omega_v := \{(r,z) \in \Omega : r > r_2\}$. Hence the computational domain will be $\Omega = \cup_{i\in\Lambda}\Omega_i$ where $\Lambda = \{s,t,d,v\}$.

## 2.3 Eddy-current problem

In presence of a conductive material, the electromagnetic field induces a current on its surface called **eddy current**. The presence of these currents implies that $\sigma \gg \omega\varepsilon$. Note the operators $\nabla := (\partial_r, \partial_z)^t$ and $\operatorname{div} := (\nabla\cdot\ )$ on the half-plane $\mathbb{R}_+^2$. We make use of the eddy-current approximation to simplify the Maxwell equation :

$$\begin{cases} -\operatorname{div}\left(\dfrac{1}{\mu r}\nabla(rE_\theta)\right) - i\omega\sigma E_\theta = i\omega J_\theta \text{ in } \mathbb{R}_+^2 \\ E_\theta = 0 \qquad\qquad \text{for } r = 0 \\ E_\theta \longrightarrow 0 \qquad\qquad \text{as } r^2 + z^2 \to +\infty \end{cases} \tag{2.3.1}$$

We shall assume that $\mu$ and $\sigma$ are in $L^\infty(\mathbb{R}^2_+)$ such that $\mu \geq \mu_0 > 0$ on $\mathbb{R}^2_+$ and that $\sigma \geq 0$ and $\sigma = 0$ for $r \geq r_0$ sufficiently large. For $\lambda > 1$ and $\Omega \subset \mathbb{R}^2_+$, we define the weighted functions spaces $L^2_{1/2,\lambda}(\Omega)$, $H^1_{1/2,\lambda}(\Omega)$ with the associated norms :

$$L^2_{1/2,\lambda}(\Omega) := \left\{ v : r^{1/2}(1+r^2)^{-\lambda/2} v \in L^2(\Omega) \right\}, \qquad H^1_{1/2,\lambda}(\Omega) := \left\{ v \in L^2_{1/2,\lambda}(\Omega) : r^{-1/2}\nabla(rv) \in L^2(\Omega) \right\},$$
$$||v||_{L^2_{1/2,\lambda}(\Omega)} = \left|\left| \sqrt{\frac{r}{(1+r^2)^\lambda}} v \right|\right|_{L^2(\Omega)}, \qquad ||v||^2_{H^1_{1/2,\lambda}(\Omega)} = ||v||^2_{L^2_{1/2,\lambda}(\Omega)} + \left|\left| r^{-1/2}\nabla(rv) \right|\right|^2_{L^2(\Omega)}$$

The following Lemma and Proposition were based on [1], chapter 1.

**Lemma 2.3.1.** *Let $\lambda > 1$. Any function $v$ in $H^1_{1/2,\lambda}(\mathbb{R}^2_+)$ satisfies $v = 0$ for $r = 0$ and the decay condition at infinity. Moreover, there exists a constant $C_\lambda$ such that for all $v$ in $H^1_{1/2,\lambda}(\mathbb{R}^2_+)$,*

$$||v||^2_{H^1_{1/2,\lambda}(\mathbb{R}^2_+)} \leq C_\lambda \left|\left| r^{-1/2}\nabla(rv) \right|\right|^2_{L^2(\mathbb{R}^2_+)}. \tag{2.3.2}$$

*Proof* : For $\lambda = 0$, we define :

$$L^2_{1/2}(\Omega) := L^2_{1/2,0}(\Omega) = \{ v : v\sqrt{r} \in L^2(\Omega) \}$$
$$H^1_{1/2}(\Omega) := H^1_{1/2,0}(\Omega) = \{ v \in L^2_{1/2}(\Omega) : r^{-1/2}\nabla(rv) \in L^2(\Omega) \}$$

We also introduce the semi-norm

$$|v|^2_{H^1_{1/2}(\Omega)} = \left|\left| r^{-1/2}\nabla(rv) \right|\right|^2_{L^2(\Omega)}$$

For $r_* > 0$, note $I = \{ r \in \mathbb{R} : 0 < r < r_* \}$. We define

$$L^2_{1/2}(I) := \{ \Phi : \Phi\sqrt{r} \in L^2(I) \} \qquad H^1_{1/2}(I) := \{ \Phi \in L^2_{1/2}(I) : r^{-1}\nabla(r\Phi) \in L^2(I) \}$$

Given $0 < \varepsilon < r_*$, we set $B^\varepsilon_{r_*} := \{ (r,z) \in B_{r_*} : r \geq \varepsilon \}$ and $I^\varepsilon := \{ r \in \mathbb{R} : \varepsilon < r < r_* \}$. Consider $v \in H^1_{1/2,\lambda}(B^\varepsilon_{r_*}) \subset H^1(B^\varepsilon_{r_*}) \subset L^2(H^1(I^\varepsilon), \mathbb{R})$. Note that since $H^1_{1/2}(I^\varepsilon) \subset \mathcal{C}(I^\varepsilon)$, for $0 < \varepsilon < r < r' < r_*$ and for almost all $z \in \mathbb{R}$,

$$|r'v(r',z) - rv(r,z)| = \left| \int_r^{r'} \frac{\partial}{\partial s}(sv(s,z))\,\mathrm{d}s \right| \leq |r'-r|^{1/2} \left( \int_r^{r'} s \left| s^{-1/2} \frac{\partial}{\partial s}(sv(s,z)) \right|^2 \mathrm{d}s \right)^{1/2}$$
$$\leq |r'-r|^{1/2} \sqrt{r_*}\, |v(\cdot,z)|_{H^1_{1/2}(I^\varepsilon)}$$
$$\int_{\mathbb{R}} |r'v(r',z) - rv(r,z)|^2 \,\mathrm{d}z \leq |r'-r| r_* \int_{\mathbb{R}} |v(\cdot,z)|^2_{H^1_{1/2}(I^\varepsilon)} \,\mathrm{d}z \leq |r'-r| r_* |v|^2_{H^1_{1/2}(B^\varepsilon_{r_*})}$$

Thus, for $r_n \to 0\,(n \to \infty)$, $\{ r_n v(r_n, \cdot) \}_{n\in\mathbb{N}}$ is a Cauchy sequence in $L^2(\mathbb{R})$. Since $L^2(\mathbb{R})$ is complete, the sequence converges to a limit of $L^2(\mathbb{R})$-norm $l \leq 0$. We want to prove that the limit is equal to 0, in other words that $l = 0$. If it's not, then

$$\exists C > 0,\ \forall \delta > 0,\ (0 < r < \delta) \text{ and } (||rv(r,\cdot)||^2_{L^2(\mathbb{R})} \geq C)$$

For $0 < \varepsilon < \delta < r_*$, with Fubini's theorem,

$$||v||^2_{L^2_{1/2,\lambda}(B^\varepsilon_{r_*})} \geq ||v||^2_{L^2_{1/2,\lambda}(B^\varepsilon_\delta)}$$
$$= \int_{\mathbb{R}} \left( \int_\varepsilon^\delta \frac{1}{r(1+r^2)^\lambda} |rv(r,z)|^2 \,\mathrm{d}r \right) \mathrm{d}z = \int_\varepsilon^\delta \frac{1}{r(1+r^2)^\lambda} \left( \int_{\mathbb{R}} |rv(r,z)|^2 \,\mathrm{d}z \right) \mathrm{d}r$$
$$\geq C \frac{1}{(1+\delta^2)^\lambda} \int_\varepsilon^\delta \frac{1}{r} \,\mathrm{d}r \xrightarrow[\varepsilon\to 0]{} \infty$$

which is impossible since $v \in L^2_{1/2,\lambda}(B^\varepsilon_{r_*}) \subset L^2_{1/2,\lambda}(\mathbb{R}^2_+)$. Hence,

$$\lim_{r\to 0} ||rv(r,\cdot)||_{L^2(\mathbb{R})} = l = 0$$

This leads to $rv|_{r=0} = 0$ for almost all $z \in \mathbb{R}$. Therefore, for $v \in H^1_{1/2,\lambda}(B^\varepsilon_{r_*}) \subset L^2(H^1(I^\varepsilon), \mathbb{R})$ and almost all $z \in \mathbb{R}$ :

$$\begin{aligned}
|v(r,z)|^2 = \frac{1}{r^2}|rv|^2 = \frac{1}{r^2}\left|\int_0^r \frac{\partial}{\partial s}(sv(s,z))\,\mathrm{d}s\right|^2 &\le \frac{1}{r}\left|\int_0^r \frac{1}{\sqrt{s}}\frac{\partial}{\partial s}(sv(s,z))\,\mathrm{d}s\right|^2 \\
&\le \frac{1}{r}r\int_0^r \left|\frac{1}{\sqrt{s}}\frac{\partial}{\partial s}(sv(s,z))\right|^2 \mathrm{d}s = \int_0^r \left|\frac{1}{\sqrt{s}}\frac{\partial}{\partial s}(sv(s,z))\right|^2 \mathrm{d}s \\
&\le \int_0^{+\infty} \left|\frac{1}{\sqrt{s}}\frac{\partial}{\partial s}(sv(s,z))\right|^2 \mathrm{d}s
\end{aligned}$$

We have

$$||v(r,\cdot)||^2_{L^2(\mathbb{R})} = \int_{\mathbb{R}} |v(r,z)|^2\,\mathrm{d}z \le \int_{\mathbb{R}}\int_0^r \left|\frac{1}{\sqrt{s}}\frac{\partial}{\partial s}(sv(s,z))\right|^2 \mathrm{d}s\,\mathrm{d}z$$

By the dominated convergence theorem, for $r \to 0$, the above inequality leads to $v|_{r=0} = 0$ almost everywhere. The inequality (2.3.2) comes from :

$$\begin{aligned}
&\int_{\mathbb{R}^2_+} \frac{r}{(1+r^2)^\lambda}|v|^2\,\mathrm{d}r\,\mathrm{d}z = \int_{-\infty}^{+\infty}\int_0^{+\infty} \frac{r}{(1+r^2)^\lambda}|v(r,z)|^2\,\mathrm{d}r\,\mathrm{d}z \\
&\le \int_{-\infty}^{+\infty}\left(\int_0^{+\infty}\frac{r}{(1+r^2)^\lambda}\,\mathrm{d}r\int_0^{+\infty}\left|\frac{1}{\sqrt{s}}\frac{\partial}{\partial s}(sv(s,z))\right|^2 \mathrm{d}s\right)\mathrm{d}z \\
&= \int_0^{+\infty}\frac{r}{(1+r^2)^\lambda}\,\mathrm{d}r\int_{\mathbb{R}^2_+}\left|\frac{1}{\sqrt{s}}\frac{\partial}{\partial s}(sv(s,z))\right|^2 \mathrm{d}s\,\mathrm{d}z = \left(\int_0^{+\infty}\frac{r}{(1+r^2)^\lambda}\,\mathrm{d}r\right)|v|^2_{H^1_{1/2}(\mathbb{R}^2_+)}
\end{aligned}$$

Therefore the inequality is proved by setting

$$C_\lambda = \sqrt{1 + \int_0^{+\infty}\frac{r}{(1+r^2)^\lambda}\,\mathrm{d}r}$$

The decay condition at infinity is a consequence of $r^{-1/2}\nabla(rv) \in L^2(\Omega)$.

□

Hence, using integration by parts, the solution $E_\theta$ of (2.3.1) is equivalent to the solution $u \in H^1_{1/2,\lambda}(\mathbb{R}^2_+)$ of following variational problem :

$$\alpha(u,v) := \int_{\mathbb{R}^2_+}\frac{1}{\mu r}\nabla(ru)\cdot\nabla(r\bar{v})\,\mathrm{d}r\mathrm{d}z - \int_{\mathbb{R}^2_+} i\omega\sigma ru\bar{v}\,\mathrm{d}r\mathrm{d}z = \int_{\mathbb{R}^2_+} i\omega J_\theta r\bar{v}\,\mathrm{d}r\mathrm{d}z,\ \forall v \in H^1_{1/2,\lambda}(\mathbb{R}^2_+) \qquad (2.3.3)$$

**Proposition 2.3.2.** *Assume that $J_\theta \in L^2_{1/2,\lambda}(\mathbb{R}^2_+)$ has a compact support. Then the variational problem (2.3.3) admits a unique solution in $H^1_{1/2,\lambda}(\mathbb{R}^2_+)$ for all $\lambda > 1$.*

*Proof* : The proof is a consequence of the Lax-Milgram theorem.

The compactly supported $J_\theta$ guarantees the continuity of the right-hand side :

$$\begin{aligned}
\forall v \in H^1_{1/2,\lambda}(\mathbb{R}^2_+),& \\
|l(v)| &:= \left| \int_{\mathbb{R}^2_+} i\omega J_\theta r\bar{v}\,\mathrm{d}r\mathrm{d}z \right| \leq \omega \left| \int_{\mathbb{R}^2_+} (\sqrt{r}J_\theta)(\sqrt{r}\bar{v})\,\mathrm{d}r\mathrm{d}z \right| \\
&= \omega \left| \int_{\mathrm{supp}(J_\theta)} (\sqrt{r}J_\theta)(\sqrt{r}\bar{v})\,\mathrm{d}r\mathrm{d}z \right| \\
&\leq \frac{\omega}{\min_{\mathrm{supp}(J_\theta)}\left(\frac{1}{(1+r^2)^\lambda}\right)} \left| \int_{\mathrm{supp}(J_\theta)} \left(\frac{\sqrt{r}}{(1+r^2)^{\lambda/2}}J_\theta\right)\left(\frac{\sqrt{r}}{(1+r^2)^{\lambda/2}}\bar{v}\right)\mathrm{d}r\mathrm{d}z \right| \\
&\leq C||J_\theta||_{L^2_{1/2,\lambda}(\mathrm{supp}(J_\theta))}||v||_{L^2_{1/2,\lambda}(\mathrm{supp}(J_\theta))} \leq C||J_\theta||_{L^2_{1/2,\lambda}(\mathbb{R}^2_+)}||v||_{H^1_{1/2,\lambda}(\mathbb{R}^2_+)}
\end{aligned}$$

The coercivity of the bilinear form is a consequence of **Lemma 2.3.1** :

$$\forall v \in H^1_{1/2,\lambda}(\mathbb{R}^2_+),\ \alpha(v,v) \geq \Re\alpha(v,v) = \int_{\mathbb{R}^2_+} \frac{1}{r}|\nabla(rv)|^2\,\mathrm{d}r\,\mathrm{d}z \geq \frac{1}{||\mu||_\infty C^2_\lambda}||v||^2_{H^1_{1/2,\lambda}(\mathbb{R}^2_+)}$$

□

Here the current density is supported by the coils, **Proposition 2.3.2** ensures the well-posedness of our variational problem.

To solve the problem numerically, the computational domain is restricted to a bounded domain $\Omega$ : note $\Gamma_1 = \{(r,z) \in \mathbb{R}^2_+ / r = 0\}$, $\Gamma_2 = \{(r,z) \in \mathbb{R}^2_+ / z = z_-\}$, $\Gamma_3 = \{(r,z) \in \mathbb{R}^2_+ / r = r_*\}$ and $\Gamma_4 = \{(r,z) \in \mathbb{R}^2_+ / z = z_+\}$. Following the developments in [1] (Chapter 1), imposing a Robin condition on the radial boundary ($\Gamma_3$) and a Dirichlet-to-Neumann condition on the longitudinal direction leads to a satisfying tradeoff. In this discussion, we use a Robin condition on the longitudinal direction, that can be seen as a DtN condition at order 1. Hence the numerical problem :

$$\begin{cases} -\mathrm{div}\left(\frac{1}{\mu r}\nabla(rE_\theta)\right) - i\omega\sigma E_\theta = i\omega J_\theta \text{ in } \Omega \\ E_\theta = 0 \qquad\qquad\qquad \text{on } \Gamma^1 \\ \frac{1}{\mu r}\partial_n(rE_\theta) = i\omega E_\theta \text{ on } \Gamma^2 \cup \Gamma^3 \cup \Gamma^4 \end{cases} \tag{2.3.4}$$

Using the same assumptions as for the problem (2.3.1), the problem (2.3.4) has a unique solution $E_\theta \in H(\Omega) := H^1_{1/2,\lambda}(\Omega)$ and is equivalent to the following variational formulation, called **direct problem** :

$$\underbrace{\int_\Omega \frac{1}{\mu r}\nabla(ru)\cdot\nabla(r\bar{v})\,\mathrm{d}r\mathrm{d}z - \int_\Omega i\omega\sigma ru\bar{v}\,\mathrm{d}r\mathrm{d}z - \int_{\Gamma_2\cup\Gamma_3\cup\Gamma_4} i\omega ur\bar{v}\,\mathrm{d}s}_{a(u,v)} = \int_\Omega i\omega J_\theta r\bar{v}\,\mathrm{d}r\mathrm{d}z \tag{2.3.5}$$

In the 2D-axisymmetric eddy-current setting, the impedance has the following expression :

$$\Delta Z_{kl} = \frac{2\pi}{i\omega I^2}\int_{\Omega_d}\left(\left(\frac{1}{\mu}-\frac{1}{\mu^0}\right)\frac{1}{r}\nabla(rE_{\theta,k})\cdot\nabla(rE^0_{\theta,l}) - i\omega(\sigma-\sigma^0)E_{\theta,k}E^0_{\theta,l}r\right)\mathrm{d}r\,\mathrm{d}z \tag{2.3.6}$$

## 2.4 Scattering approach

The aim is to compute an impedance signal on a given $z$ interval. It requires to solve (2.3.5) for different coil positions. In this formulation, the right-hand side is function of $J_\theta$, supported by the coils. Hence each $z$ position calls for an updated domain with the proper coil position, that is to say that numerically we re-mesh the whole computational domain to compute the new source term. To remove that costly operation, we propose to use a scattering approach to solve the direct problem.

Consider the total field $E_\theta$. It can be seen as the superposition of the incident field $E_\theta^0$ and the diffraction of that incident field by the deposit $E_\theta^s$. Consider the variational problem for the incident field, for a given coil position :

$$\int_\Omega \frac{1}{\mu^0 r}\nabla(rE_\theta^0)\cdot\nabla(r\bar{v})\,\mathrm{d}r\mathrm{d}z - \int_\Omega i\omega\sigma^0 rE_\theta^0\bar{v}\,\mathrm{d}r\mathrm{d}z - \int_{\Gamma_2\cup\Gamma_3\cup\Gamma_4} i\omega E_\theta^0 r\bar{v}\,\mathrm{d}s = \int_\Omega i\omega J_\theta r\bar{v}\,\mathrm{d}r\mathrm{d}z \tag{2.4.1}$$

$E_\theta^0$ is considered as an input data that can be computed offline for any coil position. Subtracting (2.4.1) to (2.3.5) leads to :

$$\begin{aligned}\int_\Omega \frac{1}{\mu r}\nabla(rE_\theta)\cdot\nabla(r\bar{v})\,\mathrm{d}r\mathrm{d}z - \int_\Omega i\omega\sigma rE_\theta\bar{v}\,\mathrm{d}r\mathrm{d}z \\ - \int_\Omega \frac{1}{\mu^0 r}\nabla(rE_\theta^0)\cdot\nabla(r\bar{v})\,\mathrm{d}r\mathrm{d}z + \int_\Omega i\omega\sigma^0 rE_\theta^0\bar{v}\,\mathrm{d}r\mathrm{d}z - \int_{\Gamma_2\cup\Gamma_3\cup\Gamma_4} i\omega E_\theta^s r\bar{v}\,\mathrm{d}s = 0\end{aligned}$$

Hence,

$$a(E_\theta^s, v) = -\int_\Omega \left(\frac{1}{\mu}-\frac{1}{\mu^0}\right)\frac{1}{r}\nabla(rE_\theta^0)\cdot\nabla(r\bar{v})\,\mathrm{d}r\mathrm{d}z + \int_\Omega i\omega(\sigma-\sigma^0)rE_\theta^0\bar{v}\,\mathrm{d}r\mathrm{d}z \tag{2.4.2}$$

The source term depends now on $E_\theta^0$ and is supported on the deposit as $1/\mu - 1/\mu^0$ and $\sigma - \sigma^0$ are non zero solely inside $\Omega_d$. For each coil position, the re-meshing operation can then be replaced with the injection of the proper $E_\theta^0$ onto (2.4.2). Calculation of $E_\theta^0$ for each coil position is fast and easy : we compute a generic solution for a given coil position, for instance at $z = 0$, $E_\theta^0$ and transpose to any coil position by a translation.

## 2.5 Addition of a plate

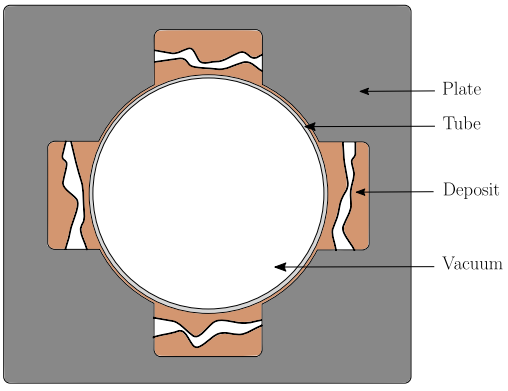


Figure 2.5.1: Sketch of a clogging deposit between the plate and the tube

Inside the steam generators, the U-tubes may oscillate due to the water flowing inside or their height 1000 times greater that its diameter. To stay still, support plates are added to the structure. Made out of a magnetic and conductive material, they are drilled accordingly to Figure 2.5.1, to maintain the tubes and let the vapor flow upwards to the turbine.

When deposits form in the area between the plate and the tube wall, they can clog the hole, preventing the vapor from flowing. This area is the main focus of the deposit detection in the industrial process, which is why we add it to our domain.

According to the data provided by the operator, the plate has a conductivity $\sigma_p = 3 \cdot 10^6\, S \cdot m^{-1}$ and a magnetic permeability $\mu_p = 50\mu_v$. Unlike Figure 2.5.1, we chose the distance between the tube and the plate to be constant, to remain in an axisymmetric configuration. The average radius for the plate is $r_p = 0.01683\, m$ and the height, $2z_p = 0.030\, m$. Note that is the 3D case the plate is not axisymmetric, as its radius actually varies with the angle.

Let $\delta = 1/\sqrt{\sigma_p \mu_p \omega}$ be the skin depth of the plate for the field. It represents the distance the electromagnetic penetrates in the plate before vanishing. Due to the high conductivity of the material, $\delta$ is more than 1000 times smaller than the plate thickness : it would be more cost efficiently to replace it by a condition on its boundary, rather that meshing it since the fields are non zero on a thin layer of elements inside the material.

### 2.5.1 Impedance condition

For reading purposes, $u$ stands for $rE_\theta$. Consider a semi-infinite plane alongside $z$, at radius $r_p$. $u^-$ is the solution outside of the plate and $u^+$, the solution in the plate. Note $\Omega_p$ and $\Gamma_p$, the plate and its boundary.

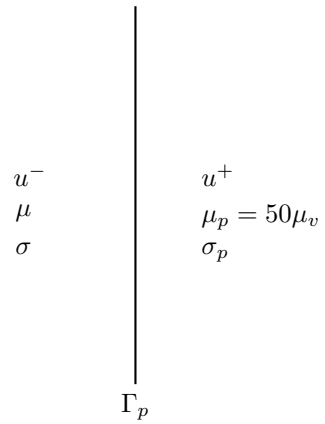


Figure 2.5.2: Solutions for a semi-infinite plate

The total field $u$ (defined as $u_{|\Omega\setminus\Omega_p} = u^-$ and $u_{|\Omega_p} = u^+$) verifies the following problem :

$$\begin{cases} -\mathrm{div}\left(\dfrac{1}{\mu}\dfrac{1}{r}\nabla u\right) - \dfrac{i\omega\sigma u}{r} = i\omega J_\theta & \text{in } \Omega \\ u^- = u^+ & \text{on } \Gamma_p \\ \dfrac{1}{\mu}\dfrac{1}{r_p}\dfrac{\partial u^-}{\partial r} = \dfrac{1}{\mu_p}\dfrac{1}{r_p}\dfrac{\partial u^+}{\partial r} & \text{on } \Gamma_p \\ u \xrightarrow[r^2+z^2\to+\infty]{} 0 \end{cases} \tag{2.5.1}$$

In particular, for the field $u^+$, the source $J_\theta$ vanishes. The divergence equation becomes :

$$\frac{\partial^2 u^+}{\partial r^2} - \frac{1}{r}\frac{\partial u^+}{\partial r} + \frac{i}{\delta^2}u^+ + \frac{\partial^2 u^+}{\partial z^2} = 0 \tag{2.5.2}$$

Consider the following change of variables $\xi = \frac{r-r_p}{\delta}$. For all $\xi$ and $z$, we write $u^+(\delta\xi + r_p) = \tilde{u}^+(\xi, z)$. (2.5.1) and (2.5.2) yields :

$$\begin{cases} \dfrac{\partial^2 \tilde{u}^+}{\partial \xi^2} + i\tilde{u}^+ - \dfrac{\delta}{\delta\xi + r_p}\dfrac{\partial \tilde{u}^+}{\partial \xi} - \delta^2 \dfrac{\partial^2 \tilde{u}^+}{\partial z^2} = 0 & \text{in } \Omega_p \\ \tilde{u}^+ = u^- & \text{on } \Gamma_p \\ \dfrac{1}{\mu_p}\dfrac{1}{r_p}\dfrac{\partial \tilde{u}^+}{\partial \xi}_{|\xi=0} = \dfrac{\delta}{\mu^0}\dfrac{1}{r_p}\dfrac{\partial u^-}{\partial r}_{|r=r_p} & \text{on } \Gamma_p \\ \tilde{u}^+ \xrightarrow[\xi^2+z^2\to+\infty]{} 0 \end{cases} \tag{2.5.3}$$

Since the skin depth $\delta$ is a small parameter ($\approx 10^{-4}$), $\tilde{u}^+$ and $u^-$ can be expanded into asymptotic series with respect to $\delta$ :

$$\begin{aligned} \tilde{u}^+ &= \tilde{u}_0^+ + \delta\tilde{u}_1^+ + \delta^2\tilde{u}_2^+ + \dots \\ u^- &= u_0^- + \delta u_1^- + \delta^2 u_2^- + \dots \end{aligned} \tag{2.5.4}$$

At the order 0 with respect to $\delta$, $\tilde{u}_0^+$ is solution of the problem :

$$\begin{cases} \dfrac{\partial^2 \tilde{u}_0^+}{\partial \xi^2} + i\tilde{u}_0^+ = 0 & \text{in } \Omega_p \\ \tilde{u}_0^+ = u_0^- & \text{on } \Gamma_p \\ \dfrac{1}{\mu_p}\dfrac{1}{r_p}\dfrac{\partial \tilde{u}_0^+}{\partial \xi}_{|\xi=0} = 0 & \text{on } \Gamma_p \\ \tilde{u}_0^+ \xrightarrow[\xi^2+z^2\to+\infty]{} 0 \end{cases} \tag{2.5.5}$$

The condition at the infinity yields $\tilde{u}_0^+(\xi, z) = \tilde{u}_0^+(0, z)\exp^{i\sqrt{i}\xi}$, where $\sqrt{i} = +(1/\sqrt{2} + i/\sqrt{2})$, and the Neumann condition at $\xi = 0$ imposes $\tilde{u}_0^+ \equiv 0$. Hence at order 0 with respect to $\delta$, the boundary condition to impose is a Dirichlet : $u_0 = 0$ on $\Gamma_p$. In other words, it is equivalent to model the plate by a perfect conductor ($\sigma_p = +\infty$).

At order 1 with respect to $\delta$, $\tilde{u}_1^+$ is solution of the problem :

$$\begin{cases} \dfrac{\partial^2 \tilde{u}_1^+}{\partial \xi^2} + i\tilde{u}_1^+ = 0 & \text{in } \Omega_p \\ \tilde{u}_1^+ = u_1^- & \text{on } \Gamma_p \\ \dfrac{1}{\mu_p}\dfrac{1}{r_p}\dfrac{\partial \tilde{u}_1^+}{\partial \xi}_{|\xi=0} = \dfrac{1}{\mu}\dfrac{1}{r_p}\dfrac{\partial u_0^-}{\partial r}_{|r=r_p} & \text{on } \Gamma_p \\ \tilde{u}_1^+ \xrightarrow[\xi^2+z^2\to+\infty]{} 0 \end{cases} \tag{2.5.6}$$

As before, the condition at the infinity yields $\tilde{u}_1^+(\xi, z) = \tilde{u}_1^+(0, z)\exp^{i\sqrt{i}\xi}$. Therefore the boundary condition on the derivative yields $\frac{1}{\mu_p} i\sqrt{i}\tilde{u}_1^+(0, z) = \frac{1}{\mu}\frac{1}{r_p}\frac{\partial u_0^-}{\partial r}(r_p, z)$. Hence :

$$\frac{1}{\mu}\frac{\partial u_1}{\partial r}(r_p, z) = \frac{1}{\mu_p}\frac{i\sqrt{i}}{\delta}u_1(r_p, z) \text{ on } \Gamma_p$$

For a semi-infinite plate at the altitude $z_p$, the same calculations lead to :

$$\frac{1}{\mu}\frac{\partial u_1}{\partial z}(r, z_p) = \frac{1}{\mu_p}\frac{i\sqrt{i}}{\delta}u_1(r, z_p) \text{ on } \Gamma_p$$

In conclusion, we impose on the plate boundary the following impedance condition :

$$\frac{1}{\mu}\frac{\partial(rE_\theta)}{\partial n} = \frac{1}{\mu_p}\frac{1}{\delta}\left(-\frac{\sqrt{2}}{2}+i\frac{\sqrt{2}}{2}\right)(rE_\theta) \text{ on } \Gamma_p \tag{2.5.7}$$

### 2.5.2 Variational formulation

Consider the scattering approach defined in subsection 2.4. In the presence of a plate, the incident field $E_\theta^0$ is scattered by the deposit and the plate. Let us write the variational formulation verified by $E_\theta^s$.

Let $\Omega$ be the computational domain with the plate excluded, $\Omega_p$, the plate and $\Omega^0$, the computational domain for the incident field. $E_\theta^0$ verifies the 2D axisymmetric eddy-current Maxwell equation in $\Omega^0$, which remains true in $\Omega \subset \Omega^0$. Therefore, $\forall v \in H(\Omega)$ :

$$\int_\Omega \left(\frac{1}{\mu^0}\frac{1}{r}\nabla(rE_\theta^0)\cdot\nabla(r\overline{v}) - i\omega\sigma^0 rE_\theta^0\overline{v}\right)\mathrm{d}r\mathrm{d}z - \int_{\partial\Omega_p}\frac{1}{\mu_v}\frac{1}{r}\frac{\partial(rE_\theta^0)}{\partial n}r\overline{v}\,\mathrm{d}s = \int_\Omega i\omega J_\theta r\overline{v}\,\mathrm{d}r\,\mathrm{d}z \tag{2.5.8}$$

The total field $E_\theta$ verifies Maxwell in $\Omega$ and the impedance condition (2.5.7) ont $\partial\Omega_p$. Hence, $\forall v \in H(\Omega)$

$$\int_\Omega \left(\frac{1}{\mu r}\nabla(rE_\theta)\cdot\nabla(r\overline{v}) - i\omega\sigma rE_\theta\overline{v}\right)\mathrm{d}r\mathrm{d}z - \int_{\partial\Omega_p}\frac{1}{\mu_p\delta}\left(-\frac{\sqrt{2}}{2}+i\frac{\sqrt{2}}{2}\right)rE_\theta\overline{v}\,\mathrm{d}s = \int_\Omega i\omega J_\theta r\overline{v}\,\mathrm{d}r\,\mathrm{d}z \tag{2.5.9}$$

Subtracting (2.5.8) to (2.5.9) leads to the following variational problem for the scattered field :

$$\begin{aligned}
&\int_\Omega \left(\frac{1}{\mu}\frac{1}{r}\nabla(rE_\theta^s)\cdot\nabla(r\overline{v}) - i\omega\sigma rE_\theta^s\overline{v}\right)\mathrm{d}r\mathrm{d}z - \int_{\partial\Omega_p}\frac{1}{\mu_p}\frac{1}{\delta}\left(-\frac{\sqrt{2}}{2}+i\frac{\sqrt{2}}{2}\right)rE_\theta^s\overline{v}\,\mathrm{d}s \\
&= -\int_{\partial\Omega_p}\left(\frac{1}{\mu_v}\frac{1}{r}\frac{\partial(rE_\theta^0)}{\partial n} - \frac{1}{\mu_p}\frac{1}{\delta}\left(-\frac{\sqrt{2}}{2}+i\frac{\sqrt{2}}{2}\right)E_\theta^0\right)rv\,\mathrm{d}s \\
&\quad + \int_\Omega\left(-\left(\frac{1}{\mu}-\frac{1}{\mu^0}\right)\frac{1}{r}\nabla(rE_\theta^0)\cdot\nabla(rE_\theta^0) + i\omega(\sigma-\sigma^0)rE_\theta^0\overline{v}\right)\mathrm{d}r\,\mathrm{d}z
\end{aligned} \tag{2.5.10}$$

### 2.5.3 Impedance

In presence of a support plate, the impedance signal definition changes to :

$$\begin{aligned}
\Delta Z_{kl} = &\frac{1}{I^2}\int_{\partial\Omega_d^{3D}}(\mathbf{E}_l^0\times\mathbf{H}_k - \mathbf{E}_k\times\mathbf{H}_l^0)\cdot\mathbf{n}\,\mathrm{d}s \\
&+\frac{1}{I^2}\int_{\partial\Omega_p^{3D}}(\mathbf{E}_l^0\times\mathbf{H}_k - \mathbf{E}_k\times\mathbf{H}_l^0)\cdot\mathbf{n}\,\mathrm{d}s
\end{aligned}$$

For a 2D axisymmetric eddy-current configuration, that formula becomes :

$$\begin{aligned}
\Delta Z_{kl} = &\frac{2\pi}{i\omega I^2}\int_{\Omega_d}\left(\left(\frac{1}{\mu}-\frac{1}{\mu^0}\right)\frac{1}{r}\nabla(rE_{\theta,k})\cdot\nabla(rE_{\theta,l}^0) - i\omega(\sigma-\sigma^0)E_{\theta,k}E_{\theta,l}^0 r\right)\mathrm{d}r\,\mathrm{d}z \\
&+\frac{2\pi}{i\omega I^2}\int_{\partial\Omega_p}\left(-\frac{1}{\mu_p}\frac{1}{\delta}i\sqrt{i}E_{\theta,l}^0 + \frac{1}{\mu_v}\frac{1}{r}\frac{\partial(rE_{\theta,l}^0)}{\partial n}\right)(rE_{\theta,k})\,\mathrm{d}s
\end{aligned} \tag{2.5.11}$$

## 2.6 Tube thickness variation

Manufacturing a steam generator is a highly complex process that needs to be precise to the utmost in order to guarantee reliability on the structure. Thorough investigations on the structure showed small variations of the tube thickness, of order less than 50 $\mu m$. Since the tube is highly conductive (of conductivity equal to $0.97 \cdot 10^6\, S \cdot m^{-1}$), even a thin variation in its thickness can significantly modify the impedance signal.

To take into account these variations at a low cost, we propose to use an asymptotical model, using the maximum amplitude, called $\delta$, of the variation ($\approx 50\mu m$) as a small parameter.

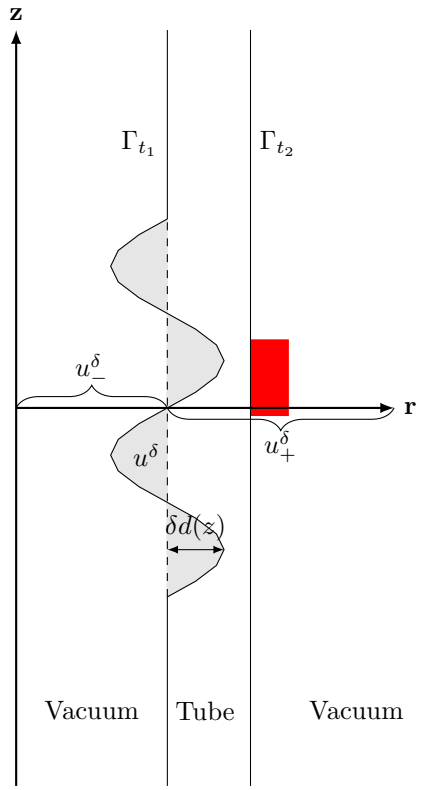


Figure 2.6.1: Representation of a non-constant tube thickness

### 2.6.1 Calculation of the transmission conditions

Consider the domain represented on Figure 2.6.1. Note $u_-^\delta$, the solution of the 2D axisymmetric eddy current Maxwell equation from $r = 0$ to the tube wall ($\Omega_-^\delta$), $u^\delta$, the solution in the tube thickness variation ($\Omega^\delta$) and $u_+^\delta$, the solution from the tube wall to $+\infty$ ($\Omega_+^\delta$). The objective here is to find an asymptotic model that can transform the thickness variation into a transmission condition at the interface $\Gamma_{t_1}$ between $u_-^\delta$ and $u_+^\delta$.

Using $\delta$ as a small parameter, the following asymptotic series can be introduced in $\Omega^\delta$ (gray areas on Figure 2.6.1) :

$$\tilde{u} = \sum_{n=0}^{+\infty} \delta^n u^n,\ u_-^\delta = \sum_{n=0}^{+\infty} \delta^n u_-^n,\ u_+^\delta = \sum_{n=0}^{+\infty} \delta^n u_+^n \tag{2.6.1}$$

Assume the tube is between the interfaces at $r = r_1 - \delta d(z)$ and at $r = r_2$, where $d(z)$, a function that describes the thickness variation. Following the work of [1], we assume the tube conductivity $\sigma_t$ can be rescaled : $\sigma_t = \frac{\sigma_1}{\delta}$ and note $k_1^2 = i\omega\mu_t\sigma_1$.
The field $u^\delta \in \Omega^\delta$ verifies the equation with no source, which can be rewritten as :

$$-u^\delta + r\partial_r u^\delta + r^2\partial_r^2 u^\delta + r^2\partial_z^2 u^\delta + \frac{k_1^2 r^2}{\delta} u^\delta = 0 \tag{2.6.2}$$

Let $\rho = \frac{r_1 - r}{\delta}$ be a new space variable in $\Omega^\delta$ and $\tilde{u}(\rho, z) = u^\delta(r_1 - \rho\delta, z), \forall(\rho, z) \in \Omega^\delta$, which leads to the following equation for $\tilde{u}$ :

$$\begin{aligned}
&\partial_\rho^2\tilde{u} = (-\delta\mathcal{B}_1 - \delta^2\mathcal{B}_2 - \delta^3\mathcal{B}_3 - \delta^4\mathcal{B}_4)\tilde{u} \\
&\text{Where } \mathcal{B}_1 = -\frac{1}{r_1}\partial_\rho - \frac{2\rho}{r_1}\partial_\rho^2 + k_1^2 \\
&\qquad \mathcal{B}_2 = \frac{\rho}{r_1^2}\partial_\rho + \frac{\rho^2}{r_1^2}\partial_\rho^2 - \frac{1}{r_1^2} + \partial_z^2 - \frac{2\rho}{r_1}k_1^2 \\
&\qquad \mathcal{B}_3 = -\frac{2\rho}{r_1}\partial_z^2 + \frac{\rho^2}{r_1^2}k_1^2 \\
&\qquad \mathcal{B}_4 = \frac{\rho^2}{r_1^2}\partial_z^2
\end{aligned} \tag{2.6.3}$$

For readability purposes, we assume the thickness variation is on **one side of the interface** $\Gamma_1$, for instance : $d(z) \geq 0$, $\forall z$. The negative case can be done identically (by inverting the roles of $u_-^\delta$ and $u_+^\delta$), and the general case can be seen as a succession of $z$-intervals where $d$ is either positive or negative.
In addition to the equation (2.6.3), $\tilde{u}$ verifies two boundary conditions : on $\rho = 0$, there is continuity of the fields and their normal derivative, which can be written as

$$\begin{cases}
\tilde{u}_{|\rho=0} = u^\delta_{+|r=r_1} \\
\tilde{u}_{|\rho=0} - \dfrac{r_1}{\delta}\partial_\rho\tilde{u}_{|\rho=0} = \partial_r(ru^\delta_+)_{|r=r_1}
\end{cases} \tag{2.6.4}$$

On the $\rho = d(z)$ interface, the quantities $u$ et $\frac{1}{\mu}\frac{1}{r}\partial_n(ru)$ are continuous. The continuity of the field yields the continuity of the tangential gradient $\tau \cdot \nabla(ru)$. The normal and the tangent to the surface is given by :

$$\tau = \begin{pmatrix} -\delta d'(z) \\ 1 \end{pmatrix} \frac{1}{1 + (\delta d'(z))^2}, \quad n = \begin{pmatrix} 1 \\ \delta d'(z) \end{pmatrix} \frac{-1}{1 + (\delta d'(z))^2} \tag{2.6.5}$$

Combining the continuities of the field, the tangential gradient and of $\frac{1}{\mu}\frac{1}{r}\nabla(ru)$, we obtain the following conditions :

$$\begin{cases}
u^\delta_{|r_1-\delta d} = u^\delta_{-|r_1-\delta d} \\
\partial_r(ru^\delta)_{|r_1-\delta d} = \left( \dfrac{\frac{\mu_t}{\mu_v} + (\delta d'(z))^2}{1 + (\delta d'(z))^2}\partial_r(ru^\delta_-) + \left(-1 + \dfrac{\mu_t}{\mu_v}\right)\dfrac{\delta d'(z)}{1 + (\delta d'(z))^2}\partial_z(ru^\delta_-) \right)_{|r_1-\delta d}
\end{cases} \tag{2.6.6}$$

The boundary condition gives information on $u_-^\delta$ at $r = r_1 - \delta d(z)$. A extension between $r - \delta d(z)$ and $r_1$ is required in order to get information on the $\Gamma_1$.
Between $r - \delta d(z)$ and $r_1$, $u_-^\delta$ verifies the 2D axisymmetric Maxwell equation in the vacuum. Introducing a new variable $\nu = r_1 - r$, we can find five operators $\mathcal{A}_i(\nu\partial_\nu, \partial_z)$, $i \in [|0, 4|]$ (see [1] for more details) so that the equation becomes :

$$\sum_{j=0}^{4} \nu^j \mathcal{A}_j(\nu\partial_\nu, \partial_z) u_-^\delta = 0 \tag{2.6.7}$$

From the asymptotic series from (2.6.1) and Taylor series on $u_-^n$ comes :

$$\begin{aligned} u_-^n(r,z) &= u_-^n(r_1-\nu, z) \\ &= \sum_{k=0}^{+\infty} \nu^k \underbrace{\frac{(-1)^k}{k!}(\partial_r^k u_-^n)(r_1,z)}_{u_-^{n,k}(z)}, \ \forall n,k \in \mathbb{N}, \ \forall (r,z) \in \Omega^\delta \end{aligned} \tag{2.6.8}$$

Note that $\nu\partial_\nu(\nu^k u_-^{n,k}) = k\nu^k u_-^{n,k}$. The operator $\mathcal{A}$ can then be seen as a function of $k$ and $\partial_z$, as long as it is applied to $\nu^k u_-^{n,k}$, $\forall k \in \mathbb{N}$.

Each term $u_+^\delta$, $\forall n \in \mathbb{N}$ verifies (2.6.7), which means :

$$\sum_{j=0}^{4}\sum_{k=0}^{+\infty} \mathcal{A}_j(k, \partial_z)(\nu^{k+j} u_-^{n,k}) = 0 \tag{2.6.9}$$

At order $k$, since that $\mathcal{A}_0(k,\partial_z) = k(k-1), \forall k \geq 2$ is invertible, there comes the following recurrence relation :

$$u_-^{n,k} = -\mathcal{A}_0^{-1}(k,\partial_z)\left(\sum_{j=1}^{4} \mathcal{A}_j(k-j,\partial_z) u_-^{n,k-j}\right) \tag{2.6.10}$$

With initial conditions $u_-^{n,0}(z) = u_-^n(r_1,z)$, $\forall z$, $\forall n$ and $u_-^{n,1}(z) = -\partial_r u_-^n(r_1,z)$, $\forall z$, $\forall n$ :

$$\begin{aligned} &u_-^{n,k}(z) = S_k^0(\partial_z) u_-^n(r_1,z) + S_k^1(\partial_z)\partial_r u_-^n(r_1,z) \\ &\text{With } S_0^0(\partial_z) = \mathrm{Id},\ S_0^1(\partial_z) = 0,\ S_1^0(\partial_z) = 0,\ S_1^1(\partial_z) = -\mathrm{Id} \\ &S_k^0(\partial_z) = -\mathcal{A}_0^{-1}(k,\partial_z)\left(\sum_{j=1}^{4} \mathcal{A}_j(k-j,\partial_z) S_{k-j}^0(\partial_z)\right) \\ &S_k^1(\partial_z) = -\mathcal{A}_0^{-1}(k,\partial_z)\left(\sum_{j=1}^{4} \mathcal{A}_j(k-j,\partial_z) S_{k-j}^1(\partial_z)\right) \end{aligned} \tag{2.6.11}$$

Going back to the asymptotical series, $\forall \nu$, $\forall z$ (we drop the $\partial_z$ in front of $S_k$ for readability purposes) :

$$\begin{cases} u_-^n(r_1-\nu,z) = \displaystyle\sum_{k=0}^{+\infty} \nu^k \left(\tilde{S}_k^0 u_-^n(r_1,z) \ + \tilde{S}_k^1 \partial_r(r u_-^n)(r_1,z))\right) \\ \partial_r(r u_-^n)(r_1-\nu,z) = \displaystyle\sum_{k=0}^{+\infty} \nu^k (k+1)\Big((\tilde{S}_k^0 - r_1\tilde{S}_{k+1}^0) u_-^n(r_1,z) \\ \qquad\qquad +(\tilde{S}_k^1 - r_1\tilde{S}_{k+1}^1)\partial_r(r u_-^n)(r_1,z)\Big) \end{cases} \tag{2.6.12}$$

Where $\tilde{S}_k^0 = S_k^0 - \frac{S_k^1}{r_1}$ and $\tilde{S}_k^1 = \frac{S_k^1}{r_1}$.

At order 0, with respect to $\delta$, $u^0$ verifies :

$$\partial_\rho^2 u^0 = 0,\ u^0_{|\rho=0} = u^0_{+|r=r_1},\ \partial_\rho u^0{}_{|\rho=0} = 0 \tag{2.6.13}$$

Hence $u^0(\rho,z) = u^0_{+|r=r_1}$, $\forall \rho \in [0, d(z)]$. Which means at $\rho = d(z)$, using (2.6.6) and (2.6.12) at order 0 :

$$\boxed{u^0_{-|r_1} = u^0_{+|r_1}} \tag{2.6.14}$$

At order 1 with respect to $\delta$, $u^1$ verifies :

$$\begin{cases} \partial_\rho^2 u^1 = -\mathcal{B}_1 u^0 = -k_1^2 u^0_{+|r_1} \\ u^1_{|\rho=0} = u^1_{+|r=r_1} \\ \partial_\rho u^1{}_{|\rho=0} = \dfrac{1}{r_1}\left(u^0_{+|r_1} - \partial_r(r u^0_+)_{|r_1}\right) \end{cases}$$

Hence $\partial_\rho u^1(\rho,z) = \frac{1}{r_1}\left(u^0_{+|r_1} + \partial_r(r u^0_+)_{|r_1}\right) - \rho k_1^2 u^0_{+|r_1}$, $\forall \rho \in [0, d(z)]$.

Using (2.6.6) at order 1 with respect to $\delta$ and the extension of $u^\delta_-$ at (2.6.11) gives the following transmission condition on the derivative :

$$\begin{aligned} u^0_{|\rho=d(z)} - r_1 \partial_\rho u^1_{|\rho=d(z)} + \underbrace{d(z)\partial_\rho u^0_{|\rho=d(z)}}_{=0} &= \frac{\mu_t}{\mu_v}\partial_r(r u^0_-)_{|r=r_1-\delta d(z)} \\ &= \frac{\mu_t}{\mu_v}\left((\tilde{S}^0_0 - r_1\tilde{S}^0_1)u^0_{-|r=r_1} + (\tilde{S}^1_0 - r_1\tilde{S}^1_1)\partial_r(r u^0_-)_{|r=r_1}\right) \\ &= \frac{\mu_t}{\mu_v}\partial_r(r u^0_-)_{|r=r_1} \end{aligned}$$

Hence $\partial_\rho u^1_{|\rho=d(z)} = \frac{1}{r_1}\left(u^0_{-|r-r_1} - \frac{\mu_t}{\mu_v}\partial_r(r u^0_-)_{|r=r_1}\right)$, which yields the following transmission condition on the derivative (noting $f_\delta(z) = \delta d(z)$) :

$$\boxed{\frac{1}{\mu_t}\frac{1}{r_1}\partial_r(r u^0_+)_{|r_1} + i\omega\sigma_t f_\delta(z) u^0_{+|r_1} = \frac{1}{\mu_v}\frac{1}{r_1}\partial_r(r u^0_-)_{|r_1}} \tag{2.6.15}$$

### 2.6.2 Variational formulation

Let $E_\theta$, be the electrical field in the computational domain $\Omega$ and $E_{\theta,+}$ (resp. $E_{\theta,-}$) its restriction in $\Omega_+$ (resp. $\Omega_-$). According to (2.6.14), $E_\theta$ is continuous through $\Gamma_{t1}$ and verifies the following PDE :

$$\boxed{\begin{cases} -\mathrm{div}\left(\dfrac{1}{\mu_v}\dfrac{1}{r}\nabla(rE_\theta)\right) = i\omega J_\theta\,(\Omega_-) \\ -\mathrm{div}\left(\dfrac{1}{\mu_+}\dfrac{1}{r}\nabla(rE_\theta)\right) - i\omega\sigma_+ E_\theta = 0\,(\Omega_+) \\ \dfrac{1}{\mu_t}\dfrac{1}{r_1}\partial_r(rE_{\theta,+}) + i\omega\sigma_t f_\delta(z) E_{\theta,+} = \dfrac{1}{\mu_v}\dfrac{1}{r_1}\partial_r(rE_{\theta,-})\,(\Gamma_{t1}) \end{cases}} \tag{2.6.16}$$

Let $v \in H(\Omega_+ \cup \Omega_-)$ be a function test. Multiplying the Maxwell equations in $(\Omega_-)$ and $(\Omega_+)$ by $v$, integrating over the domains and applying the Green formula leads to :

$$\int_\Omega \left(\frac{1}{\mu}\frac{1}{r}\nabla(rE_\theta)\cdot\nabla(r\bar{v}) - i\omega\sigma r E_\theta \bar{v}\right)\mathrm{d}r\mathrm{d}z + \int_{\Gamma_{t1}}\left(-\frac{1}{\mu_v}\frac{1}{r}\partial_r(rE_{\theta,-}) + \frac{1}{\mu_t}\frac{1}{r}\partial_r(rE_{\theta,+})\right) r\bar{v}\,\mathrm{d}s = \int_\Omega i\omega J_\theta r\bar{v}\,\mathrm{d}r\mathrm{d}z$$

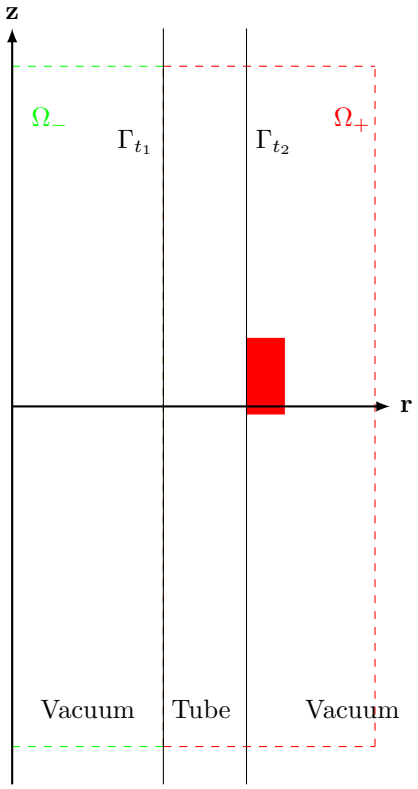


Figure 2.6.2: Representation of a non-constant tube thickness

Using the transmission condition finally yields :

$$\int_\Omega \left(\frac{1}{\mu}\frac{1}{r}\nabla(rE_\theta)\cdot\nabla(r\bar{v}) - i\omega\sigma rE_\theta\bar{v}\right)\mathrm{d}r\mathrm{d}z \; - i\omega\sigma_t\int_{\Gamma_{t1}} f_\delta(z)E_\theta r\bar{v}\,\mathrm{d}s = \int_\Omega i\omega J_\theta r\bar{v}\,\mathrm{d}r\mathrm{d}z \tag{2.6.17}$$

Hence the scattered field formulation :

$$\begin{aligned}&\int_\Omega \left(\frac{1}{\mu}\frac{1}{r}\nabla(rE^s_\theta)\cdot\nabla(r\bar{v}) - i\omega\sigma rE^s_\theta\bar{v}\right)\mathrm{d}r\mathrm{d}z \; - i\omega\sigma_t\int_{\Gamma_{t1}} f_\delta(z)E^s_\theta r\bar{v}\,\mathrm{d}s\\ &= i\omega\sigma_t\int_{\Gamma_{t1}} f_\delta(z)E^0_\theta r\bar{v}\,\mathrm{d}s\\ &\quad + \int_\Omega\left(-\left(\frac{1}{\mu}-\frac{1}{\mu^0}\right)\frac{1}{r}\nabla(rE^0_\theta)\cdot\nabla(rE^0_\theta) + i\omega(\sigma-\sigma^0)rE^0_\theta\bar{v}\right)\mathrm{d}r\,\mathrm{d}z\end{aligned} \tag{2.6.18}$$

### 2.6.3 Impedance signal

The tube thickness variation has a signature in the impedance signal that needs to be defined, as the measurements compare the electromagnetic field of the actual state to that of the incident field, where there is no tube variation.

We assume that the tube wall and the vacuum have the same permeability. For a tube thickness as represented on Figure 2.6.3, the impedance signal detected by the coils is :

$$\begin{aligned}\Delta Z_{kl} &= -\frac{2\pi}{I^2}\int_{\Omega_{t^+}}(\sigma_t-\sigma_v)rE_{\theta,k}E^0_{\theta,l}\,\mathrm{d}r\,\mathrm{d}z - \frac{2\pi}{I^2}\int_{\Omega_{t^-}}(\sigma_v-\sigma_t)rE_{\theta,k}E^0_{\theta,l}\,\mathrm{d}r\,\mathrm{d}z \\ &= -\frac{2\pi}{I^2}\int_{(z/f_\delta>0)}\int_{r_1-f_\delta}^{r_1}(\sigma_t-\sigma_v)rE_{\theta,k}E^0_{\theta,l}\,\mathrm{d}r\,\mathrm{d}z + \frac{2\pi}{I^2}\int_{(z/f_\delta<0)}\int_{r_1}^{r_1-f_\delta}(\sigma_t-\sigma_v)rE_{\theta,k}E^0_{\theta,l}\,\mathrm{d}r\,\mathrm{d}z\end{aligned}$$

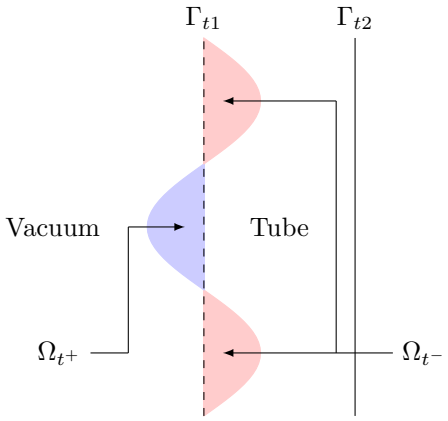


Figure 2.6.3: Representation of a non-constant tube thickness

Since the thickness variation is small ($\delta \ll 1$) and $E_\theta$ is continuous through the interface $\Gamma_{t1}$, $E_\theta(r,z) = E_\theta(r_1,z) + \mathcal{O}(\delta)\,\forall(r,z)\in\Omega_{t^+}\cup\Omega_{t^-}$. Hence,

$$\begin{aligned}\Delta Z_{kl} &= -\frac{2\pi}{I^2}\int_{(z/f_\delta>0)}(\sigma_t-\sigma_v)E_{\theta,k}|_{r_1}E^0_{\theta,l}|_{r_1}\left[\frac{r_1^2-(r_1-f_\delta(z))^2}{2}\right]\mathrm{d}z \\ &- \frac{2\pi}{I^2}\int_{(z/f_\delta<0)}(\sigma_t-\sigma_v)E_{\theta,k}|_{r_1}E^0_{\theta,l}|_{r_1}\underbrace{\left[\frac{r_1^2-(r_1-f_\delta(z))^2}{2}\right]}_{\sim f_\delta r_1+\mathcal{O}(\delta)}\mathrm{d}z + \mathcal{O}(\delta)\end{aligned}$$

$$\Delta Z_{kl} = -\frac{2\pi}{I^2}\int_{\Gamma_{t1}}(\sigma_t-\sigma_v)f_\delta E_{\theta,k}E^0_{\theta,l}r_1\,\mathrm{d}z + \mathcal{O}(\delta) \tag{2.6.19}$$

## 2.7 Thin deposits

Outside of the support plate area, it has been observed during inspections of steam generators that deposits may form, however with a thin thickness, of order ($\approx 100\,\mu m$). The formation of such longitudinal deposits is linked to the flow of vapor/liquid that goes upwards/backwards close to the tube wall, preventing the formation of volumetric shapes. The reconstruction of such deposits is costly as they require a fine mesh. As their shape is close to being one dimensional (alongside the $z$ axis), we choose here to model them using the same asymptotical model than in subsection 2.6.

This subsection is short as it has been developed in Chapter 3-4 of [1], we advise the reader to look there for more details.

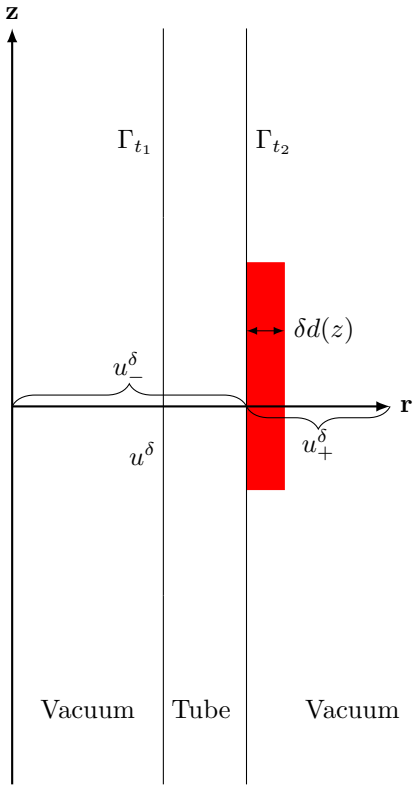


Figure 2.7.1: Representation of a thin deposit

Assume that the deposit is between the interfaces at $r = r_2$ and at $r = r_2 + \delta d(z)$, where $\delta$ is a small parameter (of order less that $100\,\mu m$) and $d(z)$, a function that describes the deposit thickness ($f_\delta(z) = \delta d(z)$). Following the work of [1], assume that the deposit conductivity $\sigma_d$ can be rescaled : $\sigma_d = \frac{\sigma_1}{\delta}$ and note $k_1^2 = i\omega\mu_d\sigma_1$. From the same asymptotic developments in Subsection 2.6 comes the following transmission between $u_-$ (the solution in the tube) and $u_+$ (the solution outside the tube) at order 0 with respect to $\delta$ :

$$\frac{1}{\mu_t}\frac{1}{r_2}\partial_r(ru_-)_{|r_2} - i\omega\sigma_d f_\delta(z)u_{-|r_2} = \frac{1}{\mu_v}\frac{1}{r_2}\partial_r(ru_+)_{|r_2} \tag{2.7.1}$$

## 2.8 Summary

On Figure 2.8.1 is a summary of the domain we consider for the inversion problem. In order to be as close as possible to the industry, a support plate is added to assess the presence of clogging deposits. Outside of the support plate, thin deposits can appear. Finally, a thin tube thickness variation is added as it has a significant influence for the impedance signal.

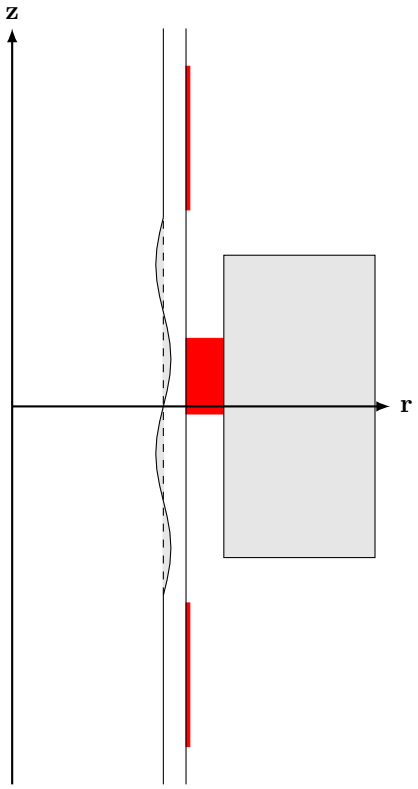


Figure 2.8.1: Actual domain

Note $f_t$, the tube thickness variation and $f_d$, the thin deposit thickness. The total field $E_\theta$ verifies the problem :

$$\begin{cases} -\text{div}\left(\dfrac{\nabla(rE_\theta)}{\mu r}\right) - i\omega\sigma E_\theta = i\omega J & \text{in } \Omega \\ \dfrac{1}{\mu}\dfrac{\partial(rE_\theta)}{\partial n} = \dfrac{1}{\mu_p}\dfrac{1}{\delta}\left(-\dfrac{\sqrt{2}}{2} + \dfrac{\sqrt{2}}{2}\right) E_\theta & \text{on } \partial\Omega_p \\ \dfrac{1}{\mu_t}\dfrac{\partial(rE_{\theta,+})}{\partial r} + i\omega\sigma_t f_t(z) r_1 E_{\theta,+} = \dfrac{1}{\mu_v}\dfrac{\partial(rE_{\theta,-})}{\partial r} & \text{on } \Gamma_{t1} \\ \dfrac{1}{\mu_t}\dfrac{\partial(rE_{\theta,-})}{\partial r} - i\omega\sigma_d f_d(z) r_1 E_{\theta,-} = \dfrac{1}{\mu_v}\dfrac{\partial(rE_{\theta,+})}{\partial r} & \text{on } \Gamma_{t2} \end{cases} \tag{2.8.1}$$

From the scattering approach defined in subsection 2.4 comes the following variational formulation for the scattered field :

$$
\begin{aligned}
&\forall v \in H(\Omega) := \left\{ v : r^{1/2}(1+r^2)^{-\lambda/2} v \in L^2(\Omega),\, r^{-1/2}\nabla(rv) \in L^2(\Omega) \right\}, \\
&\int_\Omega \left( \frac{1}{\mu}\frac{1}{r}\nabla(rE_\theta^s)\cdot\nabla(r\overline{v}) - i\omega\sigma r E_\theta^s \overline{v} \right) \mathrm{d}r\,\mathrm{d}z - \int_{\partial\Omega_p} \frac{1}{\mu_p}\frac{i\sqrt{i}}{\delta} r E_\theta^s \overline{v}\,\mathrm{d}s \\
&- i\omega\sigma_t \int_{\Gamma_{t1}} f_t(z) r E_\theta^s \overline{v}\,\mathrm{d}r - i\omega\sigma_d \int_{\Gamma_{t2}} f_d(z) r E_\theta^s \overline{v}\,\mathrm{d}r \\
&= -\int_\Omega \left( \frac{1}{\mu} - \frac{1}{\mu^0} \right) \frac{1}{r}\nabla(rE_\theta^0)\cdot\nabla(r\overline{v})\,\mathrm{d}r\mathrm{d}z + \int_\Omega i\omega(\sigma-\sigma^0) r E_\theta^0 \overline{v}\,\mathrm{d}r\,\mathrm{d}z \\
&+ \int_{\partial\Omega_p} \left( -\frac{1}{\mu_v}\frac{1}{r}\frac{\partial(rE_\theta^0)}{\partial n} + \frac{1}{\mu_p}\frac{i\sqrt{i}}{\delta} E_\theta^0 \right) (r\overline{v})\,\mathrm{d}s + i\omega\sigma_t \int_{\Gamma_{t1}} f_t(z) r E_\theta^0 \overline{v}\,\mathrm{d}r \\
&+ i\omega\sigma_d \int_{\Gamma_{t2}} f_d(z) r E_\theta^0 \overline{v}\,\mathrm{d}r
\end{aligned}
\tag{2.8.2}
$$

The impedance signal for a coil position then becomes :

$$
\begin{aligned}
\Delta Z_{kl} = &\frac{2\pi}{i\omega I^2} \int_{\Omega_d} \left( \left( \frac{1}{\mu} - \frac{1}{\mu^0} \right) \frac{1}{r}\nabla(rE_{\theta,k})\cdot\nabla(rE_{\theta,l}^0) - i\omega(\sigma-\sigma^0) E_{\theta,k} E_{\theta,l}^0 r \right) \mathrm{d}r\,\mathrm{d}z \\
&+ \frac{2\pi}{i\omega I^2} \int_{\partial\Omega_p} \left( -\frac{1}{\mu_p}\frac{1}{\delta} i\sqrt{i} E_{\theta,l}^0 + \frac{1}{\mu^0}\frac{1}{r}\frac{\partial(rE_{\theta,l}^0)}{\partial n} \right) (rE_{\theta,k})\,\mathrm{d}s \\
&- \frac{2\pi}{I^2} \int_{\Gamma_{t1}} (\sigma_t - \sigma_v) f_t E_{\theta,k} E_{\theta,l}^0 r_1\,\mathrm{d}z - \frac{2\pi}{I^2} \int_{\Gamma_{t1}} (\sigma_d - \sigma_v) f_d E_{\theta,k} E_{\theta,l}^0 r_2\,\mathrm{d}z
\end{aligned}
\tag{2.8.3}
$$

# 3 Optimization problem

In the previous section, we discussed the model used to compute the impedance $Z$ for a given domain configuration (that is to say for a given shape deposit $\Omega_d$, tube thickness variation $f_t$, and thin deposit thickness $f_d$). Consider now $N$ impedance mesures on a given $z$ interval, for different pulsations : $Z_{\text{mes}}$. The aim is to find the optimal shape $\Omega_d^*$, tube thickness variation $f_t^*$ and thin deposit thickness $f_d^*$ for which the corresponding signal matches these measures. In terms of optimization problem, this can be written as :

$$\text{Find } \Omega_d^*,\ f_t^* \text{ and } f_d^* \text{ solution of :}$$
$$\min_{\Omega_d, f_t, f_d} \left[ \mathcal{J}(\Omega_d, f_t, f_d) := \sum_{\omega} \left( \int_{-z_0}^{z_0} |Z(\Omega_d, f_t, f_d; \zeta; \omega) - Z_{\text{mes}}(\zeta; \omega)|^2 \, \mathrm{d}\zeta \right) \right] \tag{3.0.1}$$

We choose to solve (3.0.1) with a gradient descent simultaneously on the three unknowns that are $\Omega_d$, $f_t$, and $f_d$. To explain how the optimization works for each case, we consider sub-problems for each unknown where only one is allowed to change and the others are fixed. The actual optimization algorithm is a sum of these sub-problems.

Note that in the following, we write $E_\theta$ as $E$, for reading purposes.

## 3.1 Shape optimization

### 3.1.1 Shape derivative

Before explaining the optimization algorithm, there needs to introduce some notations to properly derivate the cost function with respect to the shape $\Omega_d$.

For $\mathcal{Q}$, a regular open subset of $\Omega$, we can define a domain deformation as a perturbation of the identity :

$$\mathrm{Id} + \theta : \mathcal{Q} \to \mathcal{Q}_\theta = (\mathrm{Id} + \theta)\mathcal{Q}$$

where $\theta \in W^{1,\infty}(\mathcal{Q}, \mathcal{Q})^2$ is a perturbation field such that its support is null inside $\Omega_s$ or $\Omega_t$ (invariant domains) : we focus on deformations at the vicinity of the deposit boundary and the vacuum.

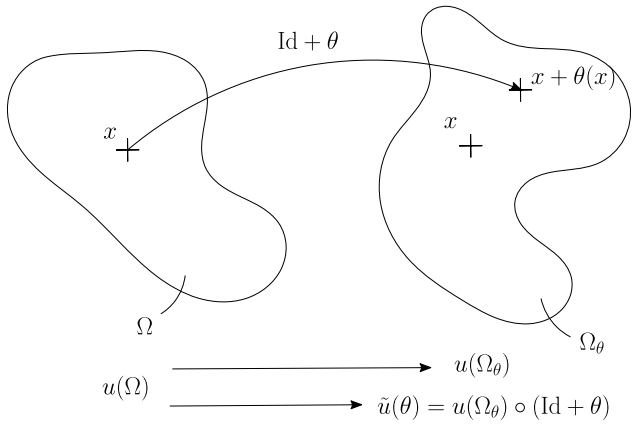


Figure 3.1.1: Derivation with respect to a shape

**Definition 3.1.1.** *Let $v = v(\mathcal{Q})$ be a shape-dependent function that belongs to some Banach space $B$ (that may depend on $\mathcal{Q}$). If $\tilde{v}(\theta) := v(\mathcal{Q}_\theta) \circ (Id + \theta) \in B$, then the* **material derivative** *(Lagrangian derivative) $V(\theta)$ of $v$ is defined as a linear functional with respect to $\theta$ with values in $B$ such that*

$$\tilde{v}(\theta) = \tilde{v}(0) + V(\theta) + o(\theta) \quad in\ \mathcal{Q}$$

*where* $\lim_{\theta\to 0} \frac{||o(\theta)||_B}{||\theta||_{1,\infty}} = 0$.

*The* **shape derivative** *(Eulerian derivative)* $v'(\theta)$ *of* $v$ *is defined by :*

$$v(\mathcal{Q}_\theta) = v(\mathcal{Q}) + v'(\theta) + o(\theta) \quad in\ \omega \in \mathcal{Q} \cap \mathcal{Q}_\theta$$

**Remark 3.1.2.** *Using the chain rule, a relation ties the material and shape derivative :*

$$V(\theta) = v'(\theta) + \theta \cdot \nabla v(\mathcal{Q}) \tag{3.1.1}$$

Similarly to solid or fluid mechanics, two definitions can be given to the derivative with respect to a shape $\mathcal{Q}$. The Eulerian approach (in a fixed domain) is the easiest one to understand : it compares for each point $x \in \mathcal{Q} \cap \mathcal{Q}_\theta$ the two functions $v(\mathcal{Q})$ and $v(\mathcal{Q}_\theta)$. The Lagrangian approach (in a moving domain) compares for a point $x \in \mathcal{Q}$ the value of $v(\mathcal{Q})$ at $x$ and the value of $v(\mathcal{Q}_\theta)$ at $x+\theta(x)$. Formula (3.1.1) can be read as the Lagrangian derivative is the combination of the Eulerian derivative and the domain displacement.

We apply to the optimization problem a gradient descent algorithm : the shape derivative of the cost function needs to be computed. Let $\theta$ be a perturbation of the domain $\Omega$. For one pulsation $\omega$ and one position $z$, we have :

$$\begin{aligned} |Z(\Omega) - Z_{\text{mes}}|^2 &= \overline{(Z(\Omega) - Z_{\text{mes}})}(Z(\Omega) - Z_{\text{mes}}) \\ &= |Z(\Omega)|^2 + |Z_{\text{mes}}|^2 - \overline{Z(\Omega)}Z_{\text{mes}} - Z(\Omega)\overline{Z_{\text{mes}}} \\ &= |Z(\Omega)|^2 + |Z_{\text{mes}}|^2 - 2\Re\left(Z(\Omega)\overline{Z_{\text{mes}}}\right) \end{aligned}$$

Given the definition above, the shape derivative of $|Z(\Omega) - Z_{\text{mes}}|^2$, for a perturbation $\theta$, writes :

$$\begin{aligned} |Z(\Omega_\theta) - Z_{\text{mes}}|^2 &= |Z(\Omega) + Z'(\theta)|^2 + |Z_{\text{mes}}|^2 - 2\Re\left((Z(\Omega) + Z'(\theta))\overline{Z_{\text{mes}}}\right) + o(\theta) \\ &= |Z(\Omega) - Z_{\text{mes}}|^2 \underbrace{-2\Re\left((Z'(\theta))\overline{Z_{\text{mes}}}\right)}_{\text{shape derivative}} + \underbrace{|Z'(\theta)|^2}_{o(\theta)} + o(\theta) \end{aligned}$$

Therefore, for the cost function :

$$\mathcal{J}'(\Omega_d)(\theta) = \sum_\omega \int_{z_{\min}}^{z_{\max}} 2\Re\left(Z'(\theta)\overline{(Z(\Omega_d, f_d, f_t; \zeta; \omega) - Z^{mes}(\zeta))}\right) \tag{3.1.2}$$

To compute the shape derivative of the impedance, we need to prove some preliminary results. In the following, we work with $w := rE_\theta \in \tilde{H}(\Omega) := \{v : rv \in H(\Omega)\}$. For any $\mathcal{Q} \subset \Omega$, let $\alpha(\mathcal{Q})$ be the following shape-dependent sesquilinear form :

$$\alpha(\mathcal{Q})(u(\mathcal{Q}), v(\mathcal{Q})) := \int_{\mathcal{Q}} \left(\frac{1}{\mu r}\nabla u \cdot \nabla \bar{v} - \frac{i\omega\sigma}{r} u\bar{v}\right) \mathrm{d}r\mathrm{d}z,\ \forall (u, v) \in \tilde{H}(\Omega)^2$$

**Lemma 3.1.3.** *Assume that* $\mu$ *and* $\sigma$ *are constant in* $\mathcal{Q}$*. Consider* $u(\mathcal{Q}) \in \tilde{H}(\Omega)$ *satisfying in the weak sense*

$$-\operatorname{div}\left(\frac{1}{\mu r}\nabla u\right) - \frac{i\omega\sigma}{r}u = 0, \text{ in } \mathcal{Q}, \tag{3.1.3}$$

$v(\mathcal{Q}) \in \tilde{H}(\mathcal{Q})$ *and assume that their shape derivatives* $(u'(\theta), v'(\theta))$ *and material derivatives* $(U(\theta), V(\theta))$ *exist. We consider in addition that* $D^2u$ *and* $D^2v$ *are in* $L^2(\mathcal{Q} \cap \{\Omega_v \cup \Omega_d\})$*. Then the shape derivative of* $\alpha(\mathcal{Q})(u(\mathcal{Q}), v(\mathcal{Q}))$*, denoted by* $\beta(\theta)$ *exists for all admissible perturbations* $\theta$ *and is given by*

$$\begin{aligned} \beta(\theta) = {} & \alpha(\mathcal{Q})(u'(\theta), v(\mathcal{Q})) + \alpha(\mathcal{Q})(u(\mathcal{Q}), V(\theta)) \\ & + \int_{\partial\mathcal{Q}} \left\{(\theta \cdot \mathbf{n})\left(\frac{1}{\mu r}\nabla_\tau u \cdot \nabla_\tau \bar{v} - \frac{i\omega\sigma}{r}u\bar{v}\right) - \left(\frac{1}{\mu r}\partial_n u(\theta \cdot \nabla_\tau \bar{v})\right)\right\} \mathrm{d}s \end{aligned} \tag{3.1.4}$$

*Proof* : To compute the shape derivative, we consider $\alpha(\mathcal{Q}_\theta)(u(\mathcal{Q}_\theta), v(\mathcal{Q}_\theta))$ and the change of variables

$$(\mathrm{Id}+\theta)^{-1} : \Omega_\theta \to \Omega,\ y \mapsto x$$

Under that change of variables, we have the following chain rule:

$$(\nabla v)\circ(\mathrm{Id}+\theta) = (\mathrm{I}+\nabla\theta)^{-t}\nabla(v\circ(\mathrm{Id}+\theta)) \quad \forall v \in \tilde{H}(\Omega_\theta)$$

where $\nabla\theta$ is the Jacobian matrix of the deformation. Hence,

$$\begin{aligned}&\alpha(\mathcal{Q}_\theta)(u(\mathcal{Q}_\theta), v(\mathcal{Q}_\theta))\\ &= \int_{\mathcal{Q}} \left(\frac{1}{r} + \theta\cdot\nabla\left(\frac{1}{r}\right) + o(\theta)\right)\left(\frac{1}{\mu}\left[A(\theta)\nabla\tilde{u}(\theta)\right]\cdot\nabla\overline{\tilde{v}(\theta)} - i\omega\sigma\nabla\tilde{u}(\theta)\nabla\overline{\tilde{v}(\theta)}|\det(I+\nabla\theta)|\right)\mathrm{d}r\mathrm{d}z\end{aligned}$$

where $A(\theta) := |\det(I+\nabla\theta)|(I+\nabla\theta)^{-1}|(I+\nabla\theta)^{-t}$ and $\tilde{u}(\theta)$ is the notation introduced in Definition 2.1.1. By definition of the material derivative and expanding with respect to $\theta$, we have the developments :

$$\begin{aligned}\tilde{u}(\theta) &= u(\mathcal{Q}) + U(\theta) + o(\theta),\\ \tilde{v}(\theta) &= v(\mathcal{Q}) + V(\theta) + o(\theta),\\ \det(I+\nabla\theta) &= 1 + \mathrm{div}\,\theta + o(\theta),\\ (I+\nabla\theta)^{-1} &= I - \nabla\theta + o(\theta).\end{aligned}$$

which leads to :

$$\begin{aligned}&\alpha(\mathcal{Q}_\theta)(u(\mathcal{Q}_\theta), v(\mathcal{Q}_\theta))\\ &= \alpha(\mathcal{Q})(u(\mathcal{Q}), v(\mathcal{Q})) + \alpha(\mathcal{Q})(U(\theta), v(\mathcal{Q})) + \alpha(\mathcal{Q})(u(\mathcal{Q}), V(\theta))\\ &+ \int_{\mathcal{Q}}\left\{\frac{1}{\mu}\left(\left(\theta\cdot\nabla\left(\frac{1}{r}\right)\right)\mathrm{Id} + \frac{1}{r}((\mathrm{div}\ \theta)\mathrm{Id} - \nabla\theta - (\nabla\theta)^t)\right)\nabla u\cdot\nabla\bar{v} - i\omega\sigma\left(\theta\cdot\nabla\left(\frac{1}{r}\right) + \frac{\mathrm{div}\ \theta}{r}\right)u\bar{v}\right\}\mathrm{d}r\mathrm{d}z + o(\theta)\\ &= \alpha(\mathcal{Q})(u(\mathcal{Q}), v(\mathcal{Q})) + \alpha(\mathcal{Q})(U(\theta), v(\mathcal{Q})) + \alpha(\mathcal{Q})(u(\mathcal{Q}), V(\theta))\\ &+ \int_{\mathcal{Q}}\left\{\frac{1}{\mu}\left(\left(\mathrm{div}\left(\frac{\theta}{r}\right)\right)\mathrm{Id} - \frac{1}{r}(\nabla\theta + (\nabla\theta)^t)\right)\nabla u\cdot\nabla\bar{v} - i\omega\sigma\mathrm{div}\left(\frac{\theta}{r}\right)u\bar{v}\right\}\mathrm{d}r\mathrm{d}z + o(\theta)\end{aligned}$$

Using the definition of $\beta(\theta)$, one has :

$$\beta(\theta) = \alpha(\mathcal{Q})(U(\theta), v(\mathcal{Q})) + \alpha(\mathcal{Q})(u(\mathcal{Q}), V(\theta)) + \mathcal{I}_1 + \mathcal{I}_2 + \mathcal{I}_3 + \mathcal{I}_4$$

with

$$\begin{aligned}\mathcal{I}_1 &= \int_{\mathcal{Q}} \frac{1}{\mu}\mathrm{div}\left(\frac{\theta}{r}\right)\nabla u\cdot\nabla\bar{v}\,\mathrm{d}r\mathrm{d}z\\ \mathcal{I}_2 &= -\int_{\mathcal{Q}} \frac{1}{\mu}\frac{1}{r}(\nabla\theta\,\nabla u)\cdot\nabla\bar{v}\,\mathrm{d}r\mathrm{d}z\\ \mathcal{I}_3 &= -\int_{\mathcal{Q}} \frac{1}{\mu}\frac{1}{r}((\nabla\theta)^t\nabla u)\cdot\nabla\bar{v}\,\mathrm{d}r\mathrm{d}z\\ \mathcal{I}_4 &= -\int_{\mathcal{Q}} i\omega\sigma\mathrm{div}\left(\frac{\theta}{r}\right)u\bar{v}\,\mathrm{d}r\mathrm{d}z\end{aligned}$$

Using integration by parts, the first integral becomes :

$$\begin{aligned}
\mathcal{I}_1 &= -\int_{\mathcal{Q}} \frac{1}{\mu r}\theta\cdot\nabla(\nabla u\cdot\nabla\bar v)\,\mathrm{d}r\mathrm{d}z + \int_{\partial\mathcal{Q}}\frac{(\theta\cdot\mathbf{n})}{\mu r}\nabla u\cdot\nabla\bar v\,\mathrm{d}s\\
&= -\int_{\mathcal{Q}} \frac{1}{\mu r}\theta\cdot(D^2u\nabla\bar v + D^2\bar v\nabla u)\,\mathrm{d}r\mathrm{d}z + \int_{\partial\mathcal{Q}}\frac{(\theta\cdot\mathbf{n})}{\mu r}\nabla u\cdot\nabla\bar v\,\mathrm{d}s\\
&= -\int_{\mathcal{Q}} \frac{1}{\mu r}\theta\cdot(\nabla(\nabla u\cdot\theta) - (\nabla\theta)^t\nabla u\cdot\nabla\bar v + D^2\bar v\nabla u)\,\mathrm{d}r\mathrm{d}z + \int_{\partial\mathcal{Q}}\frac{(\theta\cdot\mathbf{n})}{\mu r}\nabla u\cdot\nabla\bar v\,\mathrm{d}s\\
&= -\int_{\mathcal{Q}} \frac{1}{\mu r}\theta\cdot(\nabla(\nabla u\cdot\theta) + D^2\bar v\nabla u)\,\mathrm{d}r\mathrm{d}z + \int_{\partial\mathcal{Q}}\frac{(\theta\cdot\mathbf{n})}{\mu r}(\partial_n u\,\partial_n\bar v + \nabla_\tau u\cdot\nabla_\tau\bar v)\,\mathrm{d}s - \mathcal{I}_3
\end{aligned}$$

and the second :

$$\begin{aligned}
\mathcal{I}_2 &= -\int_{\mathcal{Q}}\frac{1}{\mu r}((\nabla\theta_r\cdot\nabla u)\partial_r\bar v + (\nabla\theta_z\cdot\nabla u)\partial_z\bar v)\,\mathrm{d}r\mathrm{d}z\\
&= \int_{\mathcal{Q}}\frac{1}{\mu}\left(\mathrm{div}\left(\frac{\nabla u}{r}\partial_r\bar v\right)\theta_r + \mathrm{div}\left(\frac{\nabla u}{r}\partial_z\bar v\right)\theta_z\right)\mathrm{d}r\mathrm{d}z - \int_{\partial\mathcal{Q}}\frac{1}{\mu r}(\theta\cdot\nabla\bar v)\partial_n u\,\mathrm{d}s\\
&= \int_{\mathcal{Q}}\frac{1}{\mu}\left\{\mathrm{div}\left(\frac{\nabla u}{r}\right)(\theta\cdot\nabla\bar v) + \frac{1}{\mu r}\nabla u\cdot(\nabla(\partial_r\bar v)\theta_r + \nabla(\partial_z\bar v)\theta_z)\right\}\mathrm{d}r\mathrm{d}z - \int_{\partial\mathcal{Q}}\frac{1}{\mu r}(\theta\cdot\nabla\bar v)\partial_n u\,\mathrm{d}s\\
&= \int_{\mathcal{Q}}\frac{1}{\mu}\left\{\mathrm{div}\left(\frac{\nabla u}{r}\right)(\theta\cdot\nabla\bar v) + \frac{1}{\mu r}\nabla u\cdot\left(D^2\bar v\theta\right)\right\}\mathrm{d}r\mathrm{d}z - \int_{\partial\mathcal{Q}}\frac{1}{\mu r}((\theta\cdot\mathbf{n})\partial_n\bar v + (\theta\cdot\nabla_\tau\bar v))\partial_n u\,\mathrm{d}s\\
&= \int_{\mathcal{Q}}\frac{1}{\mu}\left\{-\frac{i\omega\sigma}{r}u(\theta\cdot\nabla\bar v) + \frac{1}{\mu r}(D^2\bar v\nabla u)\cdot\theta\right\}\mathrm{d}r\mathrm{d}z - \int_{\partial\mathcal{Q}}\frac{1}{\mu r}((\theta\cdot\mathbf{n})\partial_n\bar v + (\theta\cdot\nabla_\tau\bar v))\partial_n u\,\mathrm{d}s
\end{aligned}$$

The last equality uses the equation (3.1.3) verified by $u$ in the weak sense. Finally :

$$\begin{aligned}
\mathcal{I}_2 &= \int_{\mathcal{Q}}\frac{i\omega\sigma}{r}\theta\cdot\nabla(u\bar v)\,\mathrm{d}r\mathrm{d}z - \int_{\partial\mathcal{Q}}(\theta\cdot\mathbf{n})\frac{i\omega\sigma}{r}u\bar v\,\mathrm{d}s\\
&= \int_{\mathcal{Q}}\frac{i\omega\sigma}{r}((\theta\cdot\nabla u)\bar v + (\theta\cdot\nabla\bar v)u)\,\mathrm{d}r\mathrm{d}z - \int_{\partial\mathcal{Q}}(\theta\cdot\mathbf{n})\frac{i\omega\sigma}{r}u\bar v\,\mathrm{d}s
\end{aligned}$$

To summarize the previous calculations, one gets :

$$\begin{aligned}
\mathcal{I}_1+\mathcal{I}_2+\mathcal{I}_3+\mathcal{I}_4 = &-\int_{\mathcal{Q}}\left\{\frac{1}{\mu r}\nabla(\theta\cdot\nabla u)\cdot\nabla\bar v - \frac{i\omega\sigma}{r}(\theta\cdot\nabla u)\bar v\right\}\mathrm{d}r\mathrm{d}z\\
&+\int_{\partial\mathcal{Q}}\left\{(\theta\cdot\mathbf{n})\left(\frac{1}{\mu r}\nabla_\tau u\cdot\nabla_\tau\bar v - \frac{i\omega\sigma}{r}u\bar v\right) - \frac{1}{\mu r}\partial_n u(\theta\cdot\nabla_\tau\bar v)\right\}\mathrm{d}s
\end{aligned}\tag{3.1.5}$$

Since by definition $U(\theta) - \theta\cdot\nabla u = u'(\theta)$, substituting (3.1.5) in (3.1.1) yields the result (3.1.4). □

We remind that in our model, the impedance has the following expression :

$$\begin{aligned}
\Delta Z = &\frac{2\pi}{i\omega I^2}\int_{\Omega_d}\left(\left(\frac{1}{\mu}-\frac{1}{\mu^0}\right)\frac{1}{r}\nabla w\cdot\nabla w^0 - \frac{i\omega(\sigma-\sigma^0)}{r}ww^0\right)\mathrm{d}r\,\mathrm{d}z\\
&+\frac{2\pi}{i\omega I^2}\int_{\partial\Omega_p}\left(-\frac{1}{\mu_p}\frac{1}{r}\frac{1}{\delta}i\sqrt{i}w^0 + \frac{1}{\mu_v}\frac{1}{r}\frac{\partial w^0}{\partial n}\right)w\,\mathrm{d}s\\
&-\frac{2\pi}{I^2}\int_{\Gamma_{t1}}\frac{(\sigma_t-\sigma_v)}{r}f_t ww^0\,\mathrm{d}z - \frac{2\pi}{I^2}\int_{\Gamma_{t2}}\frac{(\sigma_d-\sigma_v)}{r}f_d ww^0\,\mathrm{d}z
\end{aligned}$$

Where $E = w/r$ is the solution of the direct problem (2.3.1) with coefficients $(\mu,\sigma)$ and $E^0 = w^0/r$, the solution in a deposit-free case with coefficients $(\mu^0,\sigma^0)$.

**Proposition 3.1.4.** *The shape derivative of the impedance $\Delta Z$ is well defined and is given by :*

$$\begin{aligned}\Delta Z'(\theta) = &\frac{2\pi}{i\omega I^2}\int_{\Omega_d}\left(\left(\frac{1}{\mu}-\frac{1}{\mu^0}\right)\frac{1}{r}\nabla w'(\theta)\cdot\nabla w^0 - \frac{i\omega(\sigma-\sigma^0)}{r}w'(\theta)w^0\right)\mathrm{d}r\,\mathrm{d}z\\ &-\frac{2\pi}{i\omega I^2}\int_{\Gamma_{t1}}\frac{i\omega(\sigma_t-\sigma_v)}{r}f_t w'(\theta)w^0\,\mathrm{d}z - \frac{2\pi}{i\omega I^2}\int_{\Gamma_{t2}}\frac{i\omega(\sigma_d-\sigma_v)}{r}f_d w'(\theta)w^0\,\mathrm{d}z\\ &+\frac{2\pi}{i\omega I^2}\int_{\partial\Omega_p}\left(-\frac{1}{\mu_p}\frac{1}{r}\frac{1}{\delta}\left(-\frac{\sqrt{2}}{2}+i\frac{\sqrt{2}}{2}\right)w^0 + \frac{1}{\mu_v}\frac{1}{r}\frac{\partial w^0}{\partial n}\right)w'(\theta)\,ds\\ &+\frac{2\pi}{i\omega I^2}\int_{\partial\Omega_d}(\theta\cdot\mathbf{n})\left(\left(\frac{1}{\mu}-\frac{1}{\mu^0}\right)\frac{1}{r}\nabla w\cdot\nabla w^0 - \frac{i\omega(\sigma-\sigma^0)}{r}ww^0\right)\mathrm{d}s\end{aligned} \tag{3.1.6}$$

*where $E'(\theta)$ is the shape derivative of the electric field.*

*Proof* : Consider a deformation $(\mathrm{Id}+\theta)$ of the deposit. This deformation leaves the incident field $w^0$ invariant : therefore its shape derivative is equal to zero and its material derivative is $W^0(\theta) = \theta\cdot\nabla w^0$. As $\theta$ is supported by $\overline{\Omega_d}\setminus\Gamma_{t2}$, it leaves $\partial\Omega_p$, $\Gamma_{t1}$ and $\Gamma_{t2}$ invariant.

We first consider the shape derivative of :

$$\begin{aligned}\mathcal{I}_1 = &\frac{2\pi}{i\omega I^2}\int_{\partial\Omega_p}\left(-\frac{1}{\mu_p}\frac{1}{r}\frac{1}{\delta}i\sqrt{i}w^0 + \frac{1}{\mu_v}\frac{1}{r}\frac{\partial w^0}{\partial n}\right)w\,\mathrm{d}s\\ &-\frac{2\pi}{I^2}\int_{\Gamma_{t1}}\frac{(\sigma_t-\sigma_v)}{r}f_t ww^0\,\mathrm{d}z - \frac{2\pi}{I^2}\int_{\Gamma_{t2}}\frac{(\sigma_d-\sigma_v)}{r}f_d ww^0\,\mathrm{d}z\end{aligned}$$

By definition of the shape derivative, $\mathcal{I}_1'(\theta)$ can be computed quite easily :

$$\begin{aligned}\mathcal{I}_1'(\theta) = &\frac{2\pi}{i\omega I^2}\int_{\partial\Omega_p}\left(-\frac{1}{\mu_p}\frac{1}{r}\frac{1}{\delta}i\sqrt{i}w^0 + \frac{1}{\mu_v}\frac{1}{r}\frac{\partial w^0}{\partial n}\right)w'(\theta)\,\mathrm{d}s\\ &-\frac{2\pi}{I^2}\int_{\Gamma_{t1}}\frac{(\sigma_t-\sigma_v)}{r}f_t w'(\theta)w^0\,\mathrm{d}z - \frac{2\pi}{I^2}\int_{\Gamma_{t2}}\frac{(\sigma_d-\sigma_v)}{r}f_d w'(\theta)w^0\,\mathrm{d}z\end{aligned}$$

We now consider the shape derivative of :

$$\mathcal{I}_2 = \frac{2\pi}{i\omega I^2}\int_{\Omega_d}\left(\left(\frac{1}{\mu}-\frac{1}{\mu^0}\right)\frac{1}{r}\nabla w\cdot\nabla w^0 - \frac{i\omega(\sigma-\sigma^0)}{r}ww^0\right)\mathrm{d}r\,\mathrm{d}z$$

It can be rewritten as : $\frac{i\omega I^2}{2\pi}\mathcal{I}_2 = \alpha(\Omega_d)(w,\bar{w}^0) - \alpha_0(\Omega_d)(w^0,\bar{w})$. Since $w$ verifies (3.1.3) in $\Omega_d$ with $\mu$ and $\sigma$ constant and $w^0$, the same problem with $(\mu,\sigma) = (\mu^0,\sigma^0)$, Lemma 2.1.3 implies :

$$\begin{aligned}\frac{i\omega I^2}{2\pi}\mathcal{I}_2'(\theta) = &\,\alpha(\Omega_d)(w'(\theta),\overline{w^0}) + \alpha(\Omega_d)(w,\overline{W^0}(\theta)) - \alpha(\Omega_d)(w^0,\overline{W}(\theta))\\ &+\int_{\partial\Omega_d}\left\{(\theta\cdot\mathbf{n})\left(\frac{1}{\mu r}\nabla_\tau w\cdot\nabla_\tau w^0 - \frac{i\omega\sigma}{r}ww^0\right) - \frac{1}{\mu r}\partial_n w(\theta\cdot\nabla_\tau w^0)\right\}\mathrm{d}s\\ &-\int_{\partial\Omega_d}\left\{(\theta\cdot\mathbf{n})\left(\frac{1}{\mu^0 r}\nabla_\tau w\cdot\nabla_\tau w^0 - \frac{i\omega\sigma^0}{r}ww^0\right) - \frac{1}{\mu^0 r}\partial_n w^0(\theta\cdot\nabla_\tau w)\right\}\mathrm{d}s\end{aligned}$$

We evaluate term by term the right-hand side of the equality above. By integration by parts and using the equation satisfied by $w$ in $\Omega_d$ :

$$\begin{aligned}\alpha(\Omega_d)(w,\overline{W^0}(\theta)) &= \alpha(\Omega_d)(w,\overline{(\theta\cdot\nabla w^0)})\\ &= \int_{\Omega_d}\left(\frac{1}{\mu r}\nabla w\cdot\nabla(\theta\cdot\nabla w^0)-\frac{i\omega\sigma}{r}w(\theta\cdot\nabla w^0)\right)\mathrm{d}r\mathrm{d}z\\ &= \int_{\Omega_d}\left(-\mathrm{div}\left(\frac{1}{\mu r}\nabla w\right)-\frac{i\omega\sigma}{r}w\right)(\theta\cdot\nabla w^0)\,\mathrm{d}r\mathrm{d}z+\int_{\partial\Omega_d}\frac{1}{\mu r}\partial_n w(\theta\cdot\nabla w^0)\,\mathrm{d}s\\ &= \int_{\partial\Omega_d}\frac{1}{\mu r}\partial_n w((\theta\cdot\mathbf{n})\partial_n w^0+(\theta\cdot\nabla w^0))\,\mathrm{d}s\end{aligned}$$

From the definition of the sesquilinear form,

$$\alpha_0(\Omega_d)(w^0,\overline{W}(\theta))=\alpha_0(\Omega_d)(W(\theta),\overline{w^0})$$

Using the equation verified by $w^0$ on $\Omega_d$, we get

$$\begin{aligned}&\int_{\partial\Omega_d}\frac{1}{\mu^0 r}\partial_n w^0(\theta\cdot\nabla_\tau w)\,\mathrm{d}s\\ &=\int_{\partial\Omega_d}\frac{1}{\mu^0 r}\partial_n w^0((\theta\cdot\nabla w)-(\theta\cdot n)\partial_n w)\,\mathrm{d}s\\ &=\int_{\Omega_d}\mathrm{div}\left(\frac{1}{\mu^0 r}\nabla w^0(\theta\cdot\nabla w)\right)\mathrm{d}r\mathrm{d}z-\int_{\partial\Omega_d}\frac{1}{\mu^0 r}(\theta\cdot n)\partial_n w^0\partial_n w\,\mathrm{d}s\\ &=\int_{\Omega_d}\left\{\mathrm{div}\left(\frac{1}{\mu^0 r}\nabla w^0\right)(\theta\cdot\nabla w)+\frac{1}{\mu^0 r}\nabla w^0\cdot\nabla(\theta\cdot\nabla w)\right\}\mathrm{d}r\mathrm{d}z-\int_{\partial\Omega_d}\frac{1}{\mu^0 r}(\theta\cdot\mathbf{n})\partial_n w^0\partial_n w\,\mathrm{d}s\\ &=\int_{\Omega_d}\left\{\left(-\frac{i\omega\sigma^0}{r}w^0\right)(\theta\cdot\nabla w)+\frac{1}{\mu^0 r}\nabla w^0\cdot\nabla(\theta\cdot\nabla w)\right\}\mathrm{d}r\mathrm{d}z-\int_{\partial\Omega_d}\frac{1}{\mu^0 r}(\theta\cdot\mathbf{n})\partial_n w^0\partial_n w\,\mathrm{d}s\\ &=\alpha_0(\Omega_d)(\theta\cdot\nabla w,\overline{w^0})-\int_{\partial\Omega_d}\frac{1}{\mu^0 r}(\theta\cdot\mathbf{n})\partial_n w^0\partial_n w\,\mathrm{d}s\end{aligned}$$

Finally, with the above results, one obtains :

$$\begin{aligned}\frac{i\omega I^2}{2\pi}\mathcal{I}_2'(\theta) &= \alpha(\Omega_d)(w'(\theta),\overline{w^0})-\alpha_0(\Omega_d)(W(\theta),\overline{w^0})+\alpha_0(\Omega_d)((\theta\cdot\nabla w),\overline{w^0})\\ &\quad+\int_{\partial\Omega_d}(\theta\cdot\mathbf{n})\left\{\left(\frac{1}{\mu}-\frac{1}{\mu^0}\right)(\nabla_\tau w\cdot\nabla_\tau w^0+\partial_n w\partial_n w^0)-\frac{i\omega(\sigma-\sigma^0)}{r}ww^0\right\}\mathrm{d}s\\ &= \alpha(\Omega_d)(w'(\theta),\overline{w^0})-\alpha_0(\Omega_d)(w'(\theta),\overline{w^0})\\ &\quad+\int_{\partial\Omega_d}(\theta\cdot\mathbf{n})\left\{\left(\frac{1}{\mu}-\frac{1}{\mu^0}\right)\nabla w\cdot\nabla w^0-\frac{i\omega(\sigma-\sigma^0)}{r}ww^0\right\}\mathrm{d}s\end{aligned}$$

□

As we want to solve the shape optimization problem with a gradient descent, we need to find a descent deformation $\theta$ such that the shape derivative of the cost function is strictly negative. (3.1.6) is partially implicit with respect to $\theta$, which makes the computation of the gradient descent highly costly.

A classical method to remove that difficulty used in inverse problem is to introduce a new variational problem called **adjoint problem**, where we want to find $p$ called the **adjoint state** solution of :

$$\begin{aligned}\overline{a(q,p)} =: a^*(p,q) = &\int_{\Omega_d} \frac{1}{r}\left(\left(\frac{1}{\mu}-\frac{1}{\mu^0}\right)\nabla\overline{w^0}\cdot\nabla\overline{q} + \frac{i\omega(\sigma-\sigma^0)}{r}\overline{w^0}\overline{q}\right)\mathrm{d}r\,\mathrm{d}z,\ \forall q\in\tilde{H}(\Omega)\\ &+\int_{\Gamma_{t1}}\frac{i\omega(\sigma_t-\sigma_v)f_t}{r}\overline{w^0}\overline{q}\,\mathrm{d}z + \int_{\Gamma_{t2}}\frac{i\omega(\sigma_d-\sigma_v)f_d}{r}\overline{w^0}\overline{q}\,\mathrm{d}z\\ &+\int_{\partial\Omega_p}\left(-\frac{1}{\mu_p}\frac{1}{\delta}\frac{1}{r}\left(-\frac{\sqrt{2}}{2}-i\frac{\sqrt{2}}{2}\right)\overline{w^0}+\frac{1}{\mu^0}\frac{1}{r}\partial_n\overline{w^0}\right)\overline{q}\,\mathrm{d}s\end{aligned} \tag{3.1.7}$$

In particular, $p$ satisfies in the weak sense :

$$\begin{cases}-\mathrm{div}\left(\frac{1}{\mu r}\nabla p\right)+\frac{i\omega\sigma}{r}p = -\mathrm{div}\ \left(\left(\frac{1}{\mu}-\frac{1}{\mu^0}\right)\frac{1}{r}\nabla\overline{w^0}\right)+\frac{i\omega(\sigma-\sigma^0)}{r}\overline{w^0} & \text{in } \Omega_d,\\ -\mathrm{div}\left(\frac{1}{\mu r}\nabla p\right)+\frac{i\omega\sigma}{r}p = 0 & \text{in } \Omega_d^{\mathsf{C}},\\ [p]=0 & \text{on } \partial\Omega_d,\\ [\mu^{-1}\partial_n p] = -\left(\frac{1}{\mu}-\frac{1}{\mu^0}\right)\partial_n\overline{w}^0 & \text{on } \partial\Omega_d,\\ \frac{1}{\mu_v}\partial_n p = \frac{1}{\mu_p}\left(-\frac{\sqrt{2}}{2}-i\frac{\sqrt{2}}{2}\right)\frac{1}{\delta}p-\frac{1}{\mu_v}\partial_n\overline{w^0}+\frac{1}{\mu_p}\left(-\frac{\sqrt{2}}{2}-i\frac{\sqrt{2}}{2}\right)\frac{1}{\tilde{\delta}}\overline{w^0} & \text{on } \partial\Omega_p,\\ \frac{1}{\mu_t}\partial_r p_+ - i\omega\sigma_t f_t(z)p = \frac{1}{\mu_v}\partial_r p_- - i\omega(\sigma_t-\sigma_v)f_t(z)\overline{w^0} & \text{on } \Gamma_{t1},\\ \frac{1}{\mu_t}\partial_r p_- + i\omega\sigma_d f_d(z)p = \frac{1}{\mu_v}\partial_r p_+ - i\omega(\sigma_d-\sigma_v)f_d(z)\overline{w^0} & \text{on } \Gamma_{t2}.\end{cases} \tag{3.1.8}$$

Similarly to the direct problem, we have :

**Proposition 3.1.5.** *Let $w^0\in\tilde{H}(\Omega)$ be the solution to the eddy-current problem in a deposit-free case. Then the variational formulation (3.1.7) has a unique solution $p\in\tilde{H}(\Omega)$.*

Using [1] work leads to :

**Proposition 3.1.6.** *Let $p$ be the adjoint state satisfying the adjoint problem (3.1.7), then the shape derivative of the impedance $\Delta Z$ has the following expression :*

$$\begin{aligned}\Delta Z'(\theta) = \frac{2\pi}{i\omega I^2}\int_{\partial\Omega_d}\frac{(\theta\cdot\mathbf{n})}{r}\Big\{&\left[\frac{1}{\mu}\right]\nabla_\tau w\cdot\nabla_\tau(\overline{p}-w^0)\\ &-[\mu](\mu^{-1}\partial_n w)\left((\mu^0)^{-1}(\partial_n\overline{p})_+-(\mu^0)^{-1}(\partial_n w^0)\right)-i\omega[\sigma]w\left(\overline{p}-w^0\right)\Big\}\,\mathrm{d}s\end{aligned} \tag{3.1.9}$$

Note that because $[\mu^{-1}\partial_n\overline{p}] = -(\mu_d^{-1}-\mu_v^{-1})\partial_n w^0$ and $[\mu^{-1}\partial_n w^0]=0$ on $\Gamma$, $[\mu^{-1}\partial_n(\overline{p}-w^0)]=0$. Therefore the quantity $\overline{p}-w^0$ is in $\tilde{H}(\Omega)$, unlike $p$. Formula (3.1.9) can then be rewritten as :

$$\Delta Z'(\theta) = -\frac{2\pi}{i\omega I^2}\int_{\partial\Omega_d}\frac{(\theta\cdot\mathbf{n})}{r}\left([\mu](\mu^{-1}\nabla w)\cdot(\mu^{0^{-1}}\nabla(\overline{p}-w^0))+i\omega[\sigma]w\left(\overline{p}-w^0\right)\right)\mathrm{d}s \tag{3.1.10}$$

$Z'(\theta)$ is a linear combination of $\Delta Z'_{kl}$ : the shape derivative of the cost functional $\mathcal{J}$ can be written as

$$\mathcal{J}'(\Omega_d)(\theta) = \sum_\omega \frac{2\pi}{\omega I^2}\int_{\partial\Omega_d}(\theta\cdot\mathbf{n})g\,\mathrm{d}s$$

where $g$ is a linear combination of $g_{kl}$ :

$$g_{kl} = -\int_{z_{\min}}^{z_{\max}} \Re\left\{ \overline{(Z(\Omega_d;\zeta) - Z^{mes}(\zeta))} \left( \frac{1}{r}[\mu]\left(\mu^{-1}\nabla(rE)\right) \cdot \left(\mu^{0^{-1}}\nabla\left(r\left(\overline{p} - E^0\right)\right)\right) + i\omega[\sigma]rE\left(\overline{p} - E^0\right)\right)\Big|_\zeta \right\} \mathrm{d}\zeta$$

Note in particular that if one chooses $\theta$ such that

$$\theta = -\gamma g \mathbf{n} \quad \text{on } \partial\Omega_d \tag{3.1.11}$$

where $\gamma$ is a positive constant, then

$$J'(\Omega_d)(\theta) = -\gamma \sum_\omega \frac{2\pi}{\omega I^2} \int_{\partial\Omega_d} |g|^2 \,\mathrm{d}s \leq 0$$

which means that this provides a descent direction for $\gamma$ sufficiently small.

### 3.1.2 Perimeter penalization

Inverse problems are known to be ill-conditionned : several different optimal shapes can fit with same precision the data. To discriminate unwanted optimal shapes, it is possible to add penalizations to the algorithm.

Perimeter penalization provides a natural filter by imposing solutions with the perimeter as small as possible. We seek the shape with the smallest perimeter satisfying the following data fitting criterion :

$$\mathcal{J}(\Omega_d) \leq \varepsilon \sum_\omega \left( \int_{-z_0}^{z_0} |Z_{\mathrm{mes}}(\zeta;\omega)|^2 \,\mathrm{d}\zeta \right)$$

where $\varepsilon > 0$ is a small perimeter determining the level of data fitting we want to impose and $\mathcal{J}(\Omega_d)$, the cost function defined in (3.0.1). The corresponding problem is then :

Find $\Omega_d^*$ solution of :

$$\min_{\Omega_d} \mathcal{P}(\Omega_d) := \int_{\partial\Omega_d} 1 \,\mathrm{d}s$$
$$\text{subject to } \mathcal{J}(\Omega_d) \leq \varepsilon \sum_\omega \left( \int_{-z_0}^{z_0} |Z_{\mathrm{mes}}(\zeta;\omega)|^2 \,\mathrm{d}\zeta \right) \tag{3.1.12}$$

where $\mathcal{P}(\Omega_d)$ is the perimeter of the shape. Numerically, we prefer minimizing the Lagrangian of the problem ($\lambda$ is a parameter chosen empirically) :

$$\mathcal{L}(\Omega_d) = \mathcal{P}(\Omega_d) + \lambda \mathcal{J}(\Omega_d)$$

**Theorem 3.1.7.** *Let $\mathcal{Q} \subset \mathbb{R}^3$ be a shape, $\mathcal{P}(\mathcal{Q})$, the perimeter function defined above and $\theta$ a perturbation of $\mathcal{Q}$.*
*Then the shape derivative of the perimeter function writes :*

$$\mathcal{P}'(\mathcal{Q})(\theta) = \int_{\partial\mathcal{Q}} H(\theta \cdot \mathbf{n})\, ds \tag{3.1.13}$$

*where $H$ is the mean curvature of $\partial\mathcal{Q}$.*

*Proof* : Note $T = \mathrm{Id} + \theta$ the deformation of the domain.

$$\mathcal{P}(T(\mathcal{Q})) = \int_{\partial T(\mathcal{Q})} 1 \,\mathrm{d}\hat{s}$$

According to [5], the change of variables introduced by $T$ yields :

$$\mathcal{P}(T(\mathcal{Q})) = \int_{\partial\mathcal{Q}} |\det(\mathrm{d}T)|||(\mathrm{d}T)^{-T}\mathbf{n}||\,\mathrm{d}s$$

From $T = \mathrm{Id} + \theta$ comes the following Taylor expansions :

$$\begin{aligned}
\det(\mathrm{d}T) &= \det(\mathrm{I} + \nabla\theta) = 1 + \operatorname{div}\theta + o(\theta) \\
(\mathrm{d}T)^{-T}\mathbf{n} &= \mathbf{n} - (\nabla\theta)^T\mathbf{n} + o(\theta) \\
||(\mathrm{d}T)^{-T}\mathbf{n}|| &= ||\mathbf{n} - (\nabla\theta)^T\mathbf{n}|| = \underbrace{\mathbf{n}\cdot\mathbf{n}}_{=1} - \left[(\nabla\theta)^T\mathbf{n}\right]\cdot\mathbf{n} + o(\theta)
\end{aligned}$$

Hence the Taylor expansion of the perimeter function :

$$\begin{aligned}
\mathcal{P}((\mathrm{Id}+\theta)\mathcal{Q}) &= \int_{\partial\mathcal{Q}} (1 + \operatorname{div}\theta + o(\theta))(1 - [(\nabla\theta)\mathbf{n}]\cdot\mathbf{n} + o(\theta))\,\mathrm{d}s \\
&= \mathcal{P}(\mathcal{Q}) + \int_{\partial\mathcal{Q}} (\operatorname{div}\theta - [(\nabla\theta)\mathbf{n}]\cdot\mathbf{n})\,\mathrm{d}s + o(\theta) \\
&= \mathcal{P}(\mathcal{Q}) + \int_{\partial\mathcal{Q}} \operatorname{div}_{\partial\mathcal{Q}}\theta\,\mathrm{d}s + o(\theta)
\end{aligned}$$

where the operator $\operatorname{div}_{\partial\mathcal{Q}}$ is the surface divergence defined on the surface $\partial\mathcal{Q}$ as $\operatorname{div}_{\partial\mathcal{Q}}\mathbf{v} = (\operatorname{div}\tilde{\mathbf{v}} - (\nabla\tilde{\mathbf{v}})\mathbf{n}\cdot\mathbf{n})_{|\partial\mathcal{Q}}$, with $\tilde{\mathbf{v}}$ is a lifting of $\mathbf{v}$, a function defined on $\partial\mathcal{Q}$, in the neighborhood of $\partial\mathcal{Q}$.

Applying Proposition 5.4.9 from [5] leads to (3.1.13).

□

Note that $H = \operatorname{div}_{\partial\mathcal{Q}}\mathbf{n}$, where $\operatorname{div}_{\partial\mathcal{Q}}$ is the surface divergence. We use this formula to compute the mean curvature numerically.

The lifting of the normal is done using the gradient of the distance function

$$d_{\partial\mathcal{Q}}(x) = \begin{cases} d(x,\partial\mathcal{Q}),\ x \in \mathcal{Q} \\ -d(x,\partial\mathcal{Q}),\ x \in \mathcal{Q}^c \end{cases}$$

.

### 3.1.3 Level Set representation

The major issue with shape optimization is updating the shape as it can change its topology over the course of the algorithm. Numerically, it is part of the computational mesh, moving the shape implies re-meshing the whole domain : a highly costly operation assuming the gradient descent algorithm takes several iterations to converge. This motivates us to use a level-set function to model the shape for acceleration purposes.

Note $D \subset \mathbb{R}^d$ a space containing all admissible shapes $\Omega_d$ called **Region Of Interest** (ROI). We assume that the shape is contained in this subdomain. It is meshed uniformly and thinly at the beginning of the algorithm.

According to [2], the level-set function $\psi$ in $D$ associated to a shape $\Omega_d$ verifies :

$$\begin{cases} \psi(x) = 0 \Leftrightarrow x \in \partial\Omega_d \cap D \\ \psi(x) < 0 \Leftrightarrow x \in \Omega_d \\ \psi(x) > 0 \Leftrightarrow x \in (D\backslash\overline{\Omega_d}) \end{cases} \tag{3.1.14}$$

Over the course of the gradient descent algorithm, the shape $\Omega_d(t)$ evolves according to a fictitious time $t \in \mathbb{R}^+$. Note $\mathbf{V}$ the deformation speed of the $\Omega_d(t)$ and $V$, its norm. Consider a level-set of $\psi$ : $\psi(t, x(t)) = Cst$. Differentiating that equation leads to the following Hamilton-Jacobi transport equation :

$$\partial_t \psi + V|\nabla \psi| = 0 \quad \text{in } D \tag{3.1.15}$$

Solving the Hamilton-Jacobi equation for a given time step $\Delta t$ is equivalent to updating the shape. Note that $\Delta t$ plays the same role as $\gamma$ in (3.2.7) : it needs to be sufficiently small to actually descent in the algorithm and sufficiently big so that the convergence is fast enough.

One problem remains : the deformation speed $\mathbf{V}$ is only known on the shape boundary, where it is equal to $-g\mathbf{n}$. The Hamilton-Jacobi equation requires to know $\mathbf{V}$ in $D$. An extension of the deformation speed is required, here we choose to solve the following **regularization problem** :

$$-\alpha \Delta \tilde{\mathbf{V}} + \tilde{\mathbf{V}} = -g\mathbf{n}\,\delta_{\partial\Omega_d} \tag{3.1.16}$$

where $\tilde{\mathbf{V}}$ is the regularized and extended deformation speed we use to solve the Hamilton-Jacobi equation and $\alpha$, a regularization parameter chosen empirically. $\delta_{\partial\Omega_d}$ is the characteristic function of the shape boundary and is defined in the weak form as $\nabla(\mathrm{sgn}(\psi)) \cdot \mathbf{n}_{\partial\Omega_d}$, where $\mathbf{n}_{\partial\Omega_d} = \nabla\psi/||\nabla\psi||$ is the normal at the shape boundary.

## 3.2 Thickness optimization

In this subsection, we focus solely on tube thickness optimization, as all that will be said can be applied to the thin deposit thickness optimization.

Consider the interior tube wall $\Gamma_{t1}$ discretized by $N_1$ points. $f_t$ is discretized on these points, a linear interpolation is used to evaluate the function on any point of the boundary. This transform the problem to an optimization problem with respect to a vector unknown.

Note $h$ a perturbation of $f_t$ and $E'(f_t)(h)$, the derivative of $E$ with respect to $f_t$ defined by :

$$E(f_t + h) = E(f_t) + E'(f_t)(h) + o(h), \text{ where } \lim_{h\to 0} \frac{||o(h)||}{||h||_{L^2(\Gamma_{t1})}} = 0 \tag{3.2.1}$$

Using (3.2.1), the thickness derivative of the cost function writes :

$$\mathcal{J}'(f_t)(h) = \sum_{\omega} \int_{z_{\min}}^{z_{\max}} 2\Re\left( Z'(h)\overline{(Z(f_t;\zeta:\omega) - Z_{mes}(\zeta;\omega))} \right) \tag{3.2.2}$$

Similarly to the previous subsection, the thickness derivative $Z'(h)$ of the impedance writes :

$$\begin{aligned}
\Delta Z'(h) = {} & \frac{2\pi}{i\omega I^2} \int_{\Omega_d} \left( \left( \frac{1}{\mu} - \frac{1}{\mu^0} \right) \frac{1}{r} \nabla(rE'(h)) \cdot \nabla(rE^0) - i\omega(\sigma - \sigma^0) rE'(h) E^0 \right) \mathrm{d}r\,\mathrm{d}z \\
& - \frac{2\pi}{i\omega I^2} \int_{\Gamma_{t1}} i\omega(\sigma_t - \sigma_v) f_t r_1 E'(h) E^0 \,\mathrm{d}z - \frac{2\pi}{i\omega I^2} \int_{\Gamma_{t2}} i\omega(\sigma_d - \sigma_v) f_d r_2 E'(h) E^0 \,\mathrm{d}z \\
& + \frac{2\pi}{i\omega I^2} \int_{\partial\Omega_p} \left( -\frac{1}{\mu_p} \frac{1}{\delta} \left( -\frac{\sqrt{2}}{2} + i\frac{\sqrt{2}}{2} \right) E^0 + \frac{1}{\mu_v} \frac{1}{r} \frac{\partial(rE^0)}{\partial n} \right) (rE'(h)) \,\mathrm{d}s \\
& - \frac{2\pi}{i\omega I^2} \int_{\Gamma_{t1}} i\omega(\sigma_t - \sigma_v) h r_1 E E^0 \,\mathrm{d}z
\end{aligned} \tag{3.2.3}$$

As we want to solve the shape optimization problem with a gradient descent, we need to find a descent direction $h$ such that the shape derivative of the cost function is strictly negative. (3.2.3) is partially implicit with respect to $h$, which makes the computation of the gradient descent highly costly. To remove that issue, we use once again the adjoint problem introduced previously in (3.1.7) and $p$ the adjoint state.

**Proposition 3.2.1.** *Let $p$ be the adjoint state satisfying the adjoint problem (3.1.7), then the thickness derivative of the impedance $\Delta Z$ has the following expression :*

$$\Delta Z'(h) = -\frac{2\pi}{i\omega I^2} \int_{\Gamma_{t1}} h\sigma_t i\omega r_1 E \left( \overline{p} + E^0 \right) \mathrm{d}z \tag{3.2.4}$$

*Proof* : Consider the variational problem verified by $E$. Using the definition of the thickness derivative, $E'(h)$ verifies the following problem :

$$a(E'(h), v) = -\int_{\Gamma_{t1}} i\omega h r_1 E \overline{v}\,\mathrm{d}z \tag{3.2.5}$$

For $v = p$ in (3.2.5) and $q = E'(h)$ in (3.1.7), we have :

$$\begin{aligned}
-\int_{\Gamma_{t1}} i\omega h r_1 E\overline{p}\,\mathrm{d}z = a(E'(h), p) = \overline{a^*(p, E'(h))} \\
&= \int_{\Omega_d} \left( \left( \frac{1}{\mu} - \frac{1}{\mu^0} \right) \frac{1}{r} \nabla(rE'(h)) \cdot \nabla(rE^0) - i\omega(\sigma - \sigma^0) r E'(h) E^0 \right) \mathrm{d}r\,\mathrm{d}z \\
&- \int_{\Gamma_{t1}} i\omega(\sigma_t - \sigma_v) f_t r_1 E'(h) E^0\,\mathrm{d}z - \int_{\Gamma_{t2}} i\omega(\sigma_d - \sigma_v) f_d r_2 E'(h) E^0\,\mathrm{d}z \\
&+ \int_{\partial\Omega_p} \left( -\frac{1}{\mu_p} \frac{1}{\delta} \left( -\frac{\sqrt{2}}{2} + i\frac{\sqrt{2}}{2} \right) E^0 + \frac{1}{\mu_v} \frac{1}{r} \frac{\partial(rE^0)}{\partial n} \right) (rE'(h))\,\mathrm{d}s
\end{aligned}$$

Hence formula (3.2.4). □

$Z'(h)$ is a linear combination of $\Delta Z'_{kl}$, therefore the shape derivative of the cost functional $\mathcal{J}$ can be written as

$$\mathcal{J}'(f_t)(h) = \sum_{\omega} \frac{2\pi}{\omega I^2} \int_{\Gamma_{t1}} hg\,\mathrm{d}z$$

where $g$ is a linear combination of $g_{kl}$ :

$$g_{kl} = -\int_{z_{\min}}^{z_{\max}} \Re\left\{ \overline{(Z(f_t;\zeta) - Z^{mes}(\zeta))} \left( i\omega\sigma_t r_1 E \left( \overline{p} + E^0 \right) \right)\big|_\zeta \right\} \mathrm{d}\zeta \tag{3.2.6}$$

Note in particular that if one chooses $\theta$ such that

$$h = -\gamma g \quad \text{on } \Gamma_{t1} \tag{3.2.7}$$

where $\gamma$ is a positive constant, then

$$J'(f_t)(h) = -\gamma \sum_{\omega} \frac{2\pi}{\omega I^2} \int_{\Gamma_{t1}} |g|^2\,\mathrm{d}z \leq 0$$

which means that this provides a descent direction for $\gamma$ sufficiently small.

## 3.3 Inversion algorithm

The inversion algorithm is the following :

- Input data : $N$ impedance measures on $[-z_0, z_0]$.
- Initialization : Initial deposit $\Omega_d^0$ modelled by $\psi_0$, tube thickness variation and thin deposit thickness initialized to 0 : $f_d^0 = f_t^0 = 0$.
- Gradient descent : At iteration $k$
  1. Evaluate the stopping criterion : $J(\Omega_d^k, f_t^k, f_d^k) \leq \eta$
  2. Solve the adjoint problems for different coil positions
  3. Compute the resulting gradients $g$, $g_d$, $g_t$ for the current state

4. Regularize the shape gradient by solving the regularization problem
5. Solve the Hamilton-Jacobi problem for a time step $\Delta t_k$ to update the shape and update the thickness function for a given step $\gamma_k$ : $\Omega_d^{k+1}, f_t^{k+1}, f_d^{k+1}$
6. Solve the direct problem for each coil position to compute $Z(\Omega_d^{k+1}, f_t^{k+1}, f_d^{k+1})$ and $J(\Omega_d^{k+1}, f_t^{k+1}, f_d^{k+1})$.
7. – If $J(\Omega_d^{k+1}, f_t^{k+1}, f_d^{k+1}) < J(\Omega_d^k, f_t^k, f_d^k)$, the descent direction is accepted.
   – Else, go back to step 1 with smaller update steps $\Delta t_k \leftarrow \Delta t_k/2$ and $\gamma_k \leftarrow \gamma_k/2$.

Note that the update steps are chosen empirically.

## 3.4 Reconstruction of the deposit conductivity and permeability

For industry given signals, the physical properties of the deposit are generally unknown, as it is not possible to analyse the deposits inside the steam generator. That is the main motivation to briefly look into the reconstruction of $\mu$ and $\sigma$ when the deposit shape $\Omega_d$ is known.

The computational domain $\Omega$ is simplified as we consider there are no thin structures of support plate. The variational problem satisfied by $E_\theta$ becomes :

$$\begin{aligned} &\forall v \in H(\Omega) := \left\{ v : r^{1/2}(1+r^2)^{-\lambda/2} v \in L^2(\Omega),\, r^{-1/2}\nabla(rv) \in L^2(\Omega) \right\}, \\ &\int_\Omega \left( \frac{1}{\mu}\frac{1}{r}\nabla(rE_\theta)\cdot\nabla(r\overline{v}) - i\omega\sigma r E_\theta \overline{v} \right) \mathrm{d}r\,\mathrm{d}z = \int_\Omega i\omega J r\overline{v}\,\mathrm{d}r\,\mathrm{d}z \end{aligned} \tag{3.4.1}$$

As for the impedance signal :

$$\Delta Z_{kl} = \frac{2\pi}{i\omega I^2}\int_{\Omega_d}\left( \left(\frac{1}{\mu}-\frac{1}{\mu^0}\right)\frac{1}{r}\nabla(rE_{\theta,k})\cdot\nabla(rE^0_{\theta,l}) - i\omega(\sigma-\sigma^0)E_{\theta,k}E^0_{\theta,l}r \right)\mathrm{d}r\,\mathrm{d}z \tag{3.4.2}$$

We furthermore make the assumption that both $\mu$ and $\sigma$ are constant inside the deposit.

### 3.4.1 Derivation with respect to the conductivity

Consider a perturbation $\delta\sigma_d$ of the conductivity : $\sigma_d \leftarrow \sigma_d + \delta\sigma_d$. That yields a perturbation of the field, noted $\delta E_\theta$. We apply this to (3.4.1) :

$$\int_\Omega \left( \frac{1}{\mu}\frac{1}{r}\nabla(r(E_\theta+\delta E_\theta))\cdot\nabla(r\overline{v}) - i\omega(\sigma+\chi_{\Omega_d}\delta\sigma_d)r(E_\theta+\delta E_\theta)\overline{v} \right)\mathrm{d}r\,\mathrm{d}z = \int_\Omega i\omega J r\overline{v}\,\mathrm{d}r\,\mathrm{d}z$$

where $\chi_{\Omega_d}$ is the characteristic function of $\Omega_d$. At order 0 we find the variational formulation (3.4.1). For the first order terms, we introduce $\partial_\sigma E_\theta$ the derivative of $E_\theta$ with respect to $\sigma_d$ such that :

$$\partial_\sigma E_\theta := \lim_{\delta\sigma_d\to 0}\frac{\delta E_\theta}{\delta\sigma_d}$$

This definition leads to the following equation as $\delta\sigma_d$ tends to 0 :

$$\int_\Omega \left( \frac{1}{\mu}\frac{1}{r}\nabla(r\partial_\sigma E_\theta)\cdot\nabla(r\overline{v}) - i\omega\sigma r\partial_\sigma E_\theta\overline{v} \right)\mathrm{d}r\,\mathrm{d}z = \int_{\Omega_d} i\omega E_\theta r\overline{v}\,\mathrm{d}r\,\mathrm{d}z \tag{3.4.3}$$

Using the definition of $\partial_\sigma$, we can then compute $\partial_\sigma(\Delta Z_{kl})$ :

$$\partial_\sigma(\Delta Z_{kl}) = \frac{2\pi}{i\omega I^2}\int_{\Omega_d}\left( \left(\frac{1}{\mu}-\frac{1}{\mu^0}\right)\frac{\nabla(r\partial_\sigma E_{\theta,k})\cdot\nabla(rE^0_{\theta,l})}{r} - i\omega r E^0_{\theta,l}\left((\sigma-\sigma^0)\partial_\sigma E_{\theta,k}+E_{\theta,k}\right) \right)\mathrm{d}r\,\mathrm{d}z \tag{3.4.4}$$

Knowing the derivatives of $E_\theta$ and $\Delta Z_{kl}$ with respect to $\sigma_d$, we are eventually able to compute the derivative of the cost function $\mathcal{J}$ :

$$\partial_\sigma \mathcal{J} = \int_{z_{\min}}^{z_{\max}} 2\Re\left\{\partial_\sigma Z(\Omega_d;\zeta)\overline{(Z(\Omega_d;\zeta) - Z_{\text{meas}}(\zeta)}\right\} \mathrm{d}\zeta \tag{3.4.5}$$

To minimize the cost function with respect to $\sigma_d$, we use a descent gradient method based on the derivative of the cost function $\mathcal{J}$.

### 3.4.2 Derivation with respect to the permeability

Similarly to the previous subsection, consider a perturbation $\delta\mu_d$ of the conductivity : $\mu_d \leftarrow \mu_d + \delta\mu_d$. That yields a perturbation of the field, noted $\delta E_\theta$. We apply this to (3.4.1) :

$$\int_\Omega \left(\frac{1}{\mu + \chi_d \delta\mu_d}\frac{1}{r}\nabla(r(E_\theta + \delta E_\theta))\cdot\nabla(r\overline{v}) - i\omega\sigma r(E_\theta+\delta E_\theta)\overline{v}\right)\mathrm{d}r\,\mathrm{d}z = \int_\Omega i\omega J r\overline{v}\,\mathrm{d}r\,\mathrm{d}z$$

where $\chi_{\Omega_d}$ is the characteristic function of $\Omega_d$. At order 0 we find the variational formulation (3.4.1). For the first order terms, we introduce $\partial_\mu E_\theta$ the derivative of $E_\theta$ with respect to $\mu_d$ such that :

$$\partial_\mu E_\theta := \lim_{\delta\mu_d\to 0}\frac{\delta E_\theta}{\delta\mu_d}$$

This definition leads to the following equation as $\delta\sigma_d$ tends to 0 :

$$\int_\Omega \left(\frac{1}{\mu}\frac{1}{r}\nabla(r\partial_\mu E_\theta)\cdot\nabla(r\overline{v}) - i\omega\sigma r\partial_\mu E_\theta\overline{v}\right)\mathrm{d}r\,\mathrm{d}z = \int_{\Omega_d}\frac{1}{\mu^2 r}\nabla(rE_\theta)\cdot(r\overline{v})\,\mathrm{d}r\,\mathrm{d}z \tag{3.4.6}$$

Using the definition of $\partial_\mu$, we can then compute $\partial_\mu(\Delta Z_{kl})$ :

$$\partial_\sigma(\Delta Z_{kl}) = \frac{2\pi}{i\omega I^2}\int_{\Omega_d}\left(\left(\frac{1}{\mu}-\frac{1}{\mu^0}\right)\frac{\nabla(r\partial_\mu E_{\theta,k})\cdot\nabla(rE^0_{\theta,l})}{r} - i\omega(\sigma-\sigma^0)r\partial_\mu E_{\theta,k}E^0_{\theta,l} - \frac{1}{\mu^2 r}\nabla(rE_{\theta,k})\cdot\nabla(r\overline{v})\right)\mathrm{d}r\,\mathrm{d}z \tag{3.4.7}$$

Knowing the derivatives of $E_\theta$ and $\Delta Z_{kl}$ with respect to $\mu_d$, we are eventually able to compute the derivative of the cost function $\mathcal{J}$ :

$$\partial_\sigma \mathcal{J} = \int_{z_{\min}}^{z_{\max}} 2\Re\left\{\partial_\mu Z(\Omega_d;\zeta)\overline{(Z(\Omega_d;\zeta) - Z_{\text{meas}}(\zeta)}\right\} \mathrm{d}\zeta \tag{3.4.8}$$

To minimize the cost function with respect to $\mu_d$, we use a descent gradient method based on the derivative of the cost function $\mathcal{J}$.

# 4 Numerical tests

## Implementation of the algorithm

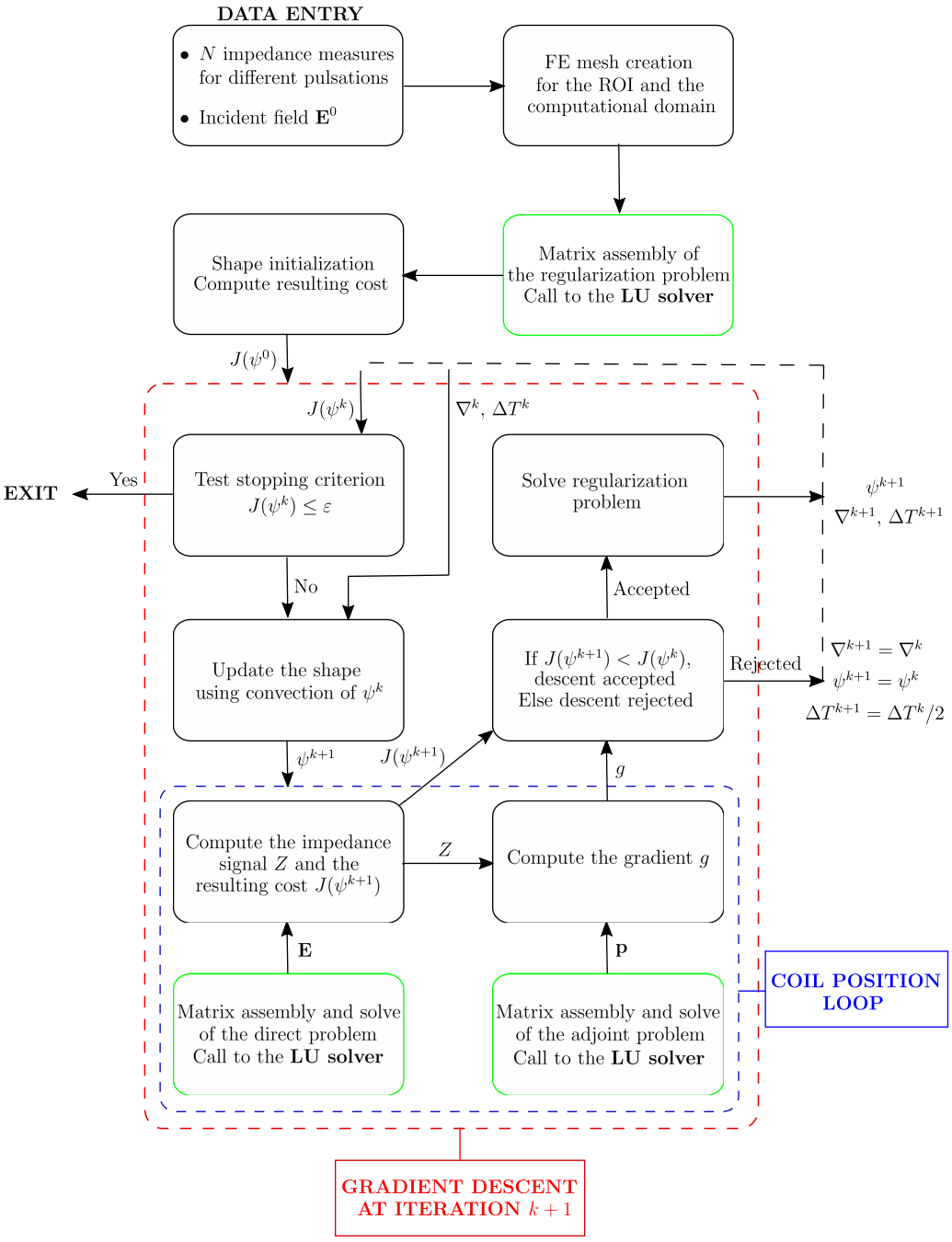


Figure 4.0.1: Organization diagram of the inversion algorithm

Figure 4.0.1 sums up the inversion algorithm described in Subsection 3.3. Its implementation is done using the Finite Elements language FreeFEM interfaced with C++, cf [6].

On the diagram, one can observe that for each iteration in the algorithm requires two FE matrix assemblies, as many RHS assembly as the number of coil positions and twice as much FE system to solve. However, in the direct problem, for each iteration, only the degrees of freedom of $\Omega_d$ change, due to the

convection of the level-set. In other words, we have :

$$\begin{aligned} a(u,v) :=& \int_\Omega \left(\frac{1}{\mu}\frac{1}{r}\nabla(ru)\cdot\nabla(r\overline{v}) - i\omega\sigma ru\overline{v}\right)\mathrm{d}r\,\mathrm{d}z \;- \int_{\partial\Omega_p}\frac{1}{\mu_p}\frac{i\sqrt{i}}{\delta}ru\overline{v}\,\mathrm{d}s \\ &- i\omega\sigma_t\int_{\Gamma_{t1}} f_t(z)ru\overline{v}\,\mathrm{d}r \;- i\omega\sigma_d\int_{\Gamma_{t2}} f_d(z)ru\overline{v}\,\mathrm{d}r \\ &= a_0(u,v) + a_d(u,v) \end{aligned}$$

where

$$\begin{aligned} a_0(u,v) =& \int_\Omega \left(\frac{1}{\mu^0}\frac{1}{r}\nabla(ru)\cdot\nabla(r\overline{v}) - i\omega\sigma^0 ru\overline{v}\right)\mathrm{d}r\,\mathrm{d}z \\ &- \int_{\partial\Omega_p}\frac{1}{\mu_p}\frac{i\sqrt{i}}{\delta}ru\overline{v}\,\mathrm{d}s - i\omega\sigma_t\int_{\Gamma_{t1}} f_t(z)ru\overline{v}\,\mathrm{d}r \;- i\omega\sigma_d\int_{\Gamma_{t2}} f_d(z)ru\overline{v}\,\mathrm{d}r \end{aligned}$$

and

$$a_d(u,v) = \int_\Omega \left(\left(\frac{1}{\mu}-\frac{1}{\mu^0}\right)\frac{1}{r}\nabla(ru)\cdot\nabla(r\overline{v}) - i\omega(\sigma-\sigma^0)ru\overline{v}\right)\mathrm{d}r\,\mathrm{d}z$$

The bilinear form $a_0$ does not depend on $\Omega_d$ and since $\frac{1}{\mu}-\frac{1}{\mu^0}$ and $\sigma-\sigma^0$ have their support inside $\Omega_d$, the assembly of $a_d$ involves solely degrees of freedom inside the deposit shape.

We can make use of these informations to accelerate the gradient descent : first, $a_0$ is assembled once before the algorithm and second, $a_d$ is assembled before the coil position loop, as it does not change with it, and on the degrees of freedom of the Region of Interest that contains $\Omega_d$. The bilinear form $a$ is then the superposition of $a_0$ and $a_d$.

For the right-hand side assembly that is done twice for each coil position (for the direct and adjoint problem) we observe that :

$$\begin{aligned} l(v) :=& -\int_\Omega \left(\frac{1}{\mu}-\frac{1}{\mu^0}\right)\frac{1}{r}\nabla(rE_\theta^0)\cdot\nabla(r\overline{v})\,\mathrm{d}r\mathrm{d}z \;+\int_\Omega i\omega(\sigma-\sigma^0)rE_\theta^0\overline{v}\,\mathrm{d}r\,\mathrm{d}z \\ &+\int_{\partial\Omega_p}\left(-\frac{1}{\mu_v}\frac{1}{r}\frac{\partial(rE_\theta^0)}{\partial n}+\frac{1}{\mu_p}\frac{i\sqrt{i}}{\delta}E_\theta^0\right)(r\overline{v})\,\mathrm{d}s \;+i\omega\sigma_t\int_{\Gamma_{t1}} f_t(z)rE_\theta^0\overline{v}\,\mathrm{d}r \;+i\omega\sigma_d\int_{\Gamma_{t2}} f_d(z)rE_\theta^0\overline{v}\,\mathrm{d}r \\ &= a_{RHS}(E_\theta^0, v) \end{aligned}$$

where

$$\begin{aligned} a_{RHS}(u,v) :=& -\int_\Omega \left(\frac{1}{\mu}-\frac{1}{\mu^0}\right)\frac{1}{r}\nabla(ru)\cdot\nabla(r\overline{v})\,\mathrm{d}r\mathrm{d}z \;+\int_\Omega i\omega(\sigma-\sigma^0)ru\overline{v}\,\mathrm{d}r\,\mathrm{d}z \\ &+\int_{\partial\Omega_p}\left(-\frac{1}{\mu_v}\frac{1}{r}\frac{\partial(ru)}{\partial n}+\frac{1}{\mu_p}\frac{i\sqrt{i}}{\delta}u\right)(r\overline{v})\,\mathrm{d}s \;+i\omega\sigma_t\int_{\Gamma_{t1}} f_t(z)ru\overline{v}\,\mathrm{d}r \;+i\omega\sigma_d\int_{\Gamma_{t2}} f_d(z)ru\overline{v}\,\mathrm{d}r \end{aligned}$$

The assembly of the right-hand side can be replaced by a matrix-vector product for each coil position, where $a_{RHS}$ is assembled once before the gradient descent.

The same reasoning can be applied to the computation of the adjoint state $p$. Note that there is no need to assemble a matrix for the adjoint problem as its bilinear form is the Hermitian transpose of that of the direct problem.

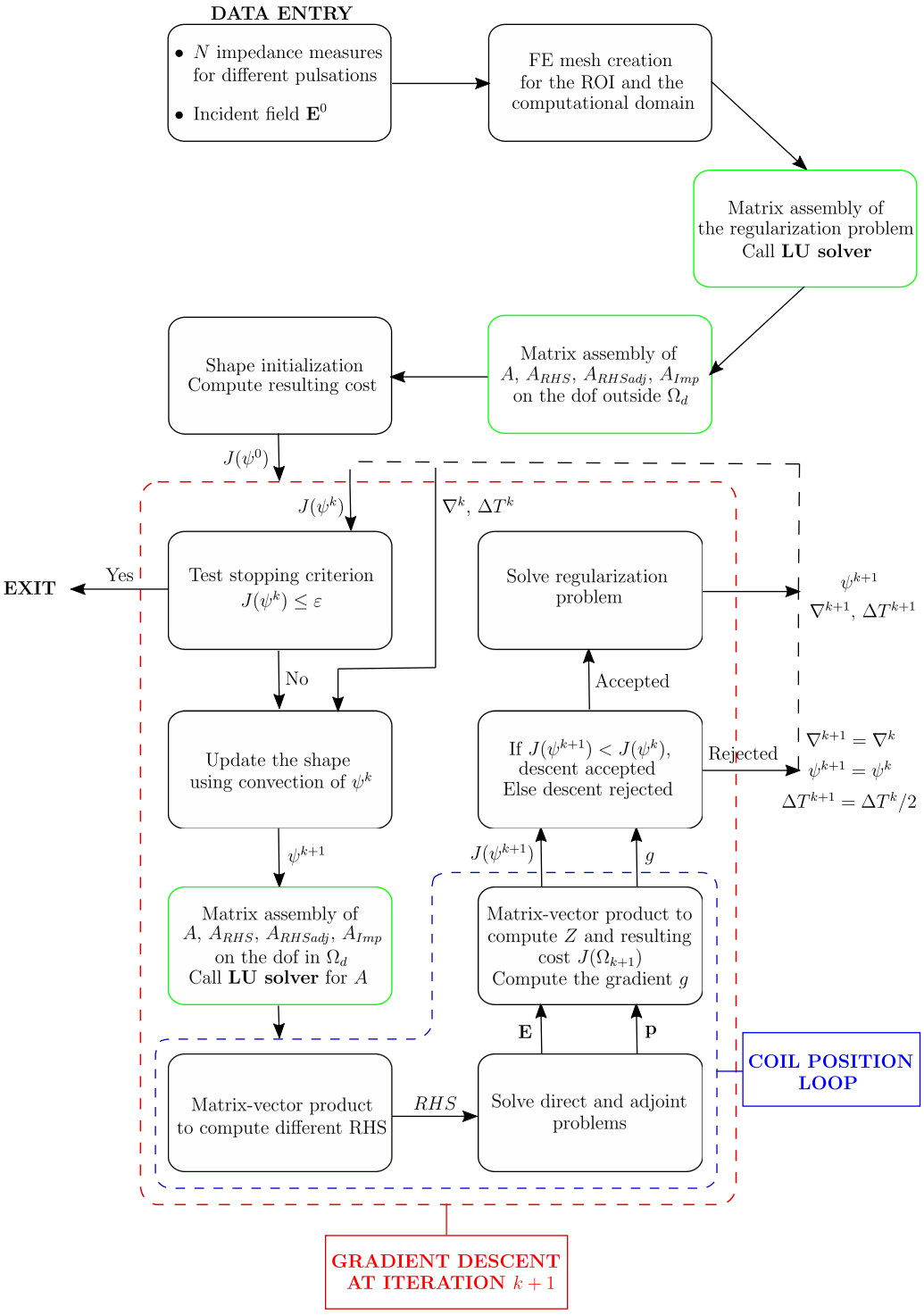


Figure 4.0.2: Organization diagram of the inversion algorithm

Finally, we can rewrite the impedance as :

$$\begin{aligned}\Delta Z_{kl} = &\frac{2\pi}{i\omega I^2}\int_{\Omega_d}\left(\left(\frac{1}{\mu}-\frac{1}{\mu^0}\right)\frac{1}{r}\nabla(rE_{\theta,k})\cdot\nabla(rE^0_{\theta,l}) - i\omega(\sigma-\sigma^0)E_{\theta,k}E^0_{\theta,l}r\right)\mathrm{d}r\,\mathrm{d}z\\ &+\frac{2\pi}{i\omega I^2}\int_{\partial\Omega_p}\left(-\frac{1}{\mu^P}\frac{1}{\delta}i\sqrt{i}E^0_{\theta,l}+\frac{1}{\mu^0}\frac{1}{r}\frac{\partial(rE^0_{\theta,l})}{\partial n}\right)(rE_{\theta,k})\,\mathrm{d}s\\ &-\frac{2\pi}{I^2}\int_{\Gamma_{t1}}(\sigma_t-\sigma_v)f_tE_{\theta,k}E^0_{\theta,l}r_1\,\mathrm{d}z-\frac{2\pi}{I^2}\int_{\Gamma_{t1}}(\sigma_d-\sigma_v)f_dE_{\theta,k}E^0_{\theta,l}r_2\,\mathrm{d}z\\ &=a_{Imp}(\overline{E^0_\theta},E_\theta)\end{aligned} \tag{4.0.1}$$

To accelerate even more the computations inside the coil position loop, we replace the explicit calculation of $\Delta Z_{kl}$ by the product $\overline{E^0_{\theta,l}}^t A_{Imp}E_{\theta,k}$.

## Impedance signals

In the following tests, we run the algorithm on synthetic data generated by solving the direct problem for a target shape. In the last part, we invert industrial data provided by EDF, using the experience gained on artificial tests.

Considering the probe we are using, we have two types of impedance signal, each giving different information about the configuration of the medium. These measures are different combinations of $\Delta Z_{kl}$ defined by (2.1.1) :

$$\begin{cases} Z_{FA} = \dfrac{i}{2}(\Delta Z_{11}+\Delta Z_{21}) & \text{absolute mode}\\ Z_{F3} = \dfrac{i}{2}(\Delta Z_{11}-\Delta Z_{22}) & \text{differential mode}\end{cases} \tag{4.0.2}$$

The differential modes are given for three pulsations $\omega_1 > \omega_2 > \omega_3$ and are written respectively $Z_{F1}$, $Z_{F2}$ and $Z_{F3}$. Due to the skin depth effect, each pulsation can give information of the medium at various thicknesses : the greater the pulsation, the less far the eletcromagnetic field goes. The absolute mode is only given for $\omega_3$.

Differential modes are sensitive to abrupt variations of the shape geometry whereas absolute modes detect smooth variations. These four industrial signals constitute the data we want to invert in order to reconstruct the deposit shape.

Note that in the different simulations, the deposit is non-magnetic. The magnetic case yields very similar results.

## Scattering : numerical error

We consider a rectangular non-magnetic deposit of thickness $0.015\,mm$ and height $0.01\,mm$, centered at the origin. The impedance signal is computed for 41 coil positions. Here we want to compare the field $E$ computed by solving (2.3.3), to the field $\tilde{E} = E^s + E^0$, where $E^s$ is solution of (2.4.2) and their resulting impedance signal, respectively $Z$ and $\tilde{Z}$. Figure 4.0.3 displays the relative error $||E-\tilde{E}||_{L^2(\Omega)}/||E||_{L^2(\Omega)}$ for different mesh sizes $h$.

Figure 4.0.4 is the relative difference between the impedance signal corresponding to each electric field for different $h$.

These plots show that the scattering approach is valid for any mesh size. Note that for a given mesh size, the error increases with the pulsation ($\omega_1 > \omega_2 > \omega_3$) as for great values, the deposit is barely seen by the coils (the skin depth is even smaller), which leads to a low amplitude signal more sensitive to noise.

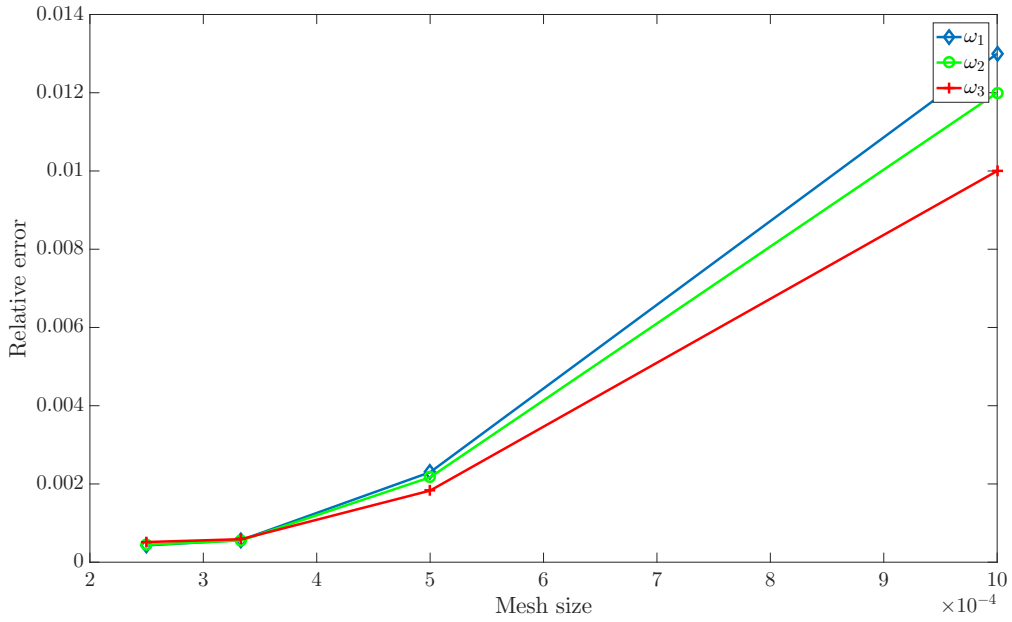


Figure 4.0.3: Relative error $||E - \tilde{E}||_{L^2(\Omega)}/||E||_{L^2(\Omega)}$ for the total field, for each pulsation

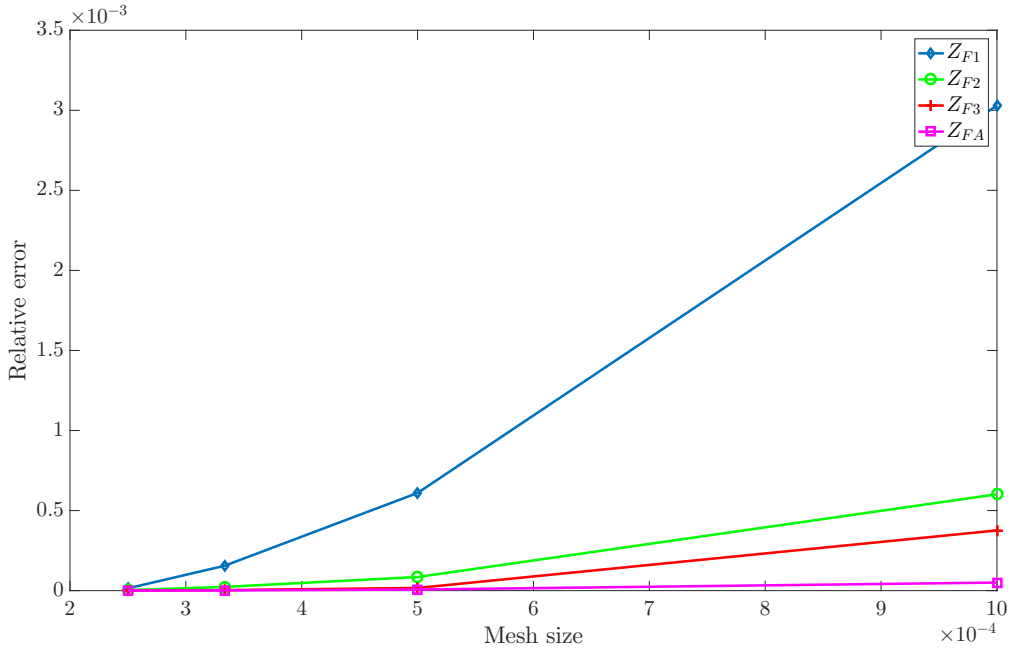


Figure 4.0.4: Relative error $||Z - \tilde{Z}||_{L^2([-z_0,z_0])}/||Z||_{L^2([-z_0,z_0])}$ for each impedance signal

## Initialization of the algorithm

From now on, we compute the total field using the diffraction approach, as we ensured in the last subsection that the numerical error of the method was small enough.

In a gradient descent method, the choice of the initialization is crucial as it needs to be close enough to the solution in order to ensure a fast convergence. And at the same time it needs to be as generic as possible to tackle any deposit shape. Considering the physical phenomenon responsible for the creation of deposits, the shape has to touch the exterior tube wall since water is flowing outside the tube.

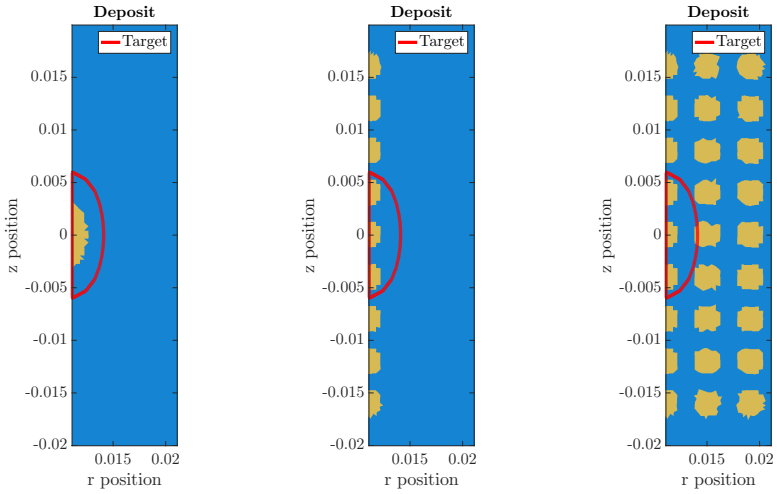


(a) One semi-ellipse (b) Nine semi-disks (c) 27 disks

Figure 4.0.5: Different initializations (in yellow) of the reconstruction algorithm. In red, the shape to reconstruct.

We first consider the following reconstruction tests (number of coil positions, 41) :

1. Target shape : semi-ellipse of radii $3\,mm$ and $6\,mm$, initialization : semi-ellipse of radii $1.5\,mm$ and $3\,mm$ on the exterior tube wall.

2. Target shape : semi-ellipse of radii $3\,mm$ and $6\,mm$, initialization : nine evenly spaced semi-circles of radius $1.33\,mm$ on the exterior tube wall.

3. Target shape : semi-ellipse of radii $3\,mm$ and $6\,mm$, initialization : three lines of nine evenly spaced semi-circles of radius $1.33\,mm$.

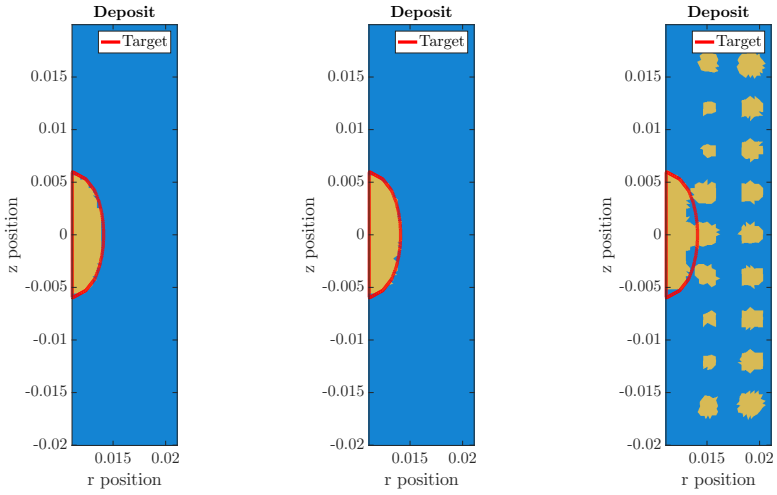


(a) One semi-ellipse (16 iterations) (b) Nine semi-disks (17 iterations) (c) 27 disks (17 iterations)

Figure 4.0.6: Optimal shape (in yellow) computed by the reconstruction algorithm for different initializations. In red, the shape to reconstruct.

Above is the optimal shape found by the algorithm for each initialization. As the first two initializations converge towards the target shape, the third case is more interesting : whereas the shape on the tube merge in the area where the target shape is located, the shapes floating in the vacuum are barely distorted by the gradient. Because these shapes have almost no impact on the impedance signal (the electric field vanishes close to the tube), the gradient has a very small impact on them. Moreover, experimentations on steam generators have proven that the expected deposits are glued to the tube wall. Therefore the third initialization should not be considered as the optimal shape found is not satisfying and it does not comply with the observations.

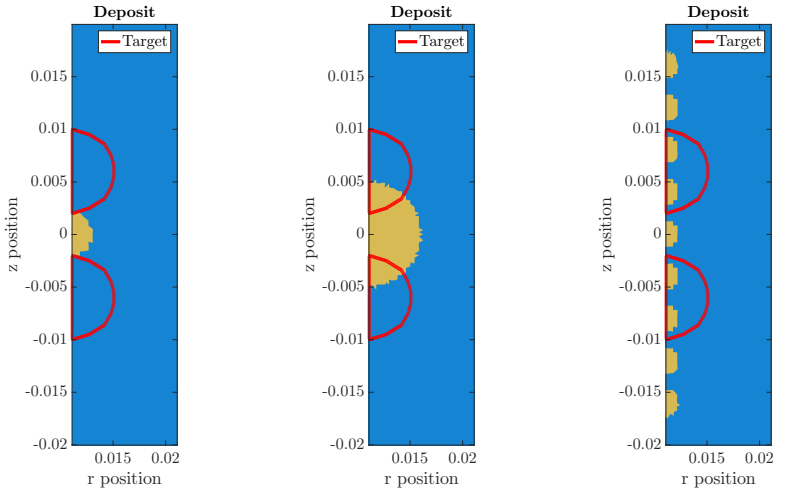


(a) Small semi-disk (b) Big semi-disk (c) Nine semi-disks

Figure 4.0.7: Different initializations (in yellow) of the reconstruction algorithm. In red, the shape to reconstruct.

If the target deposit has now more than one connected component, which initialization is the best suited to reconstruct the shape ? We consider the following tests (where the impedance signal is given for 61 coil positions) :

1. Target shape : two semi-disks of radius $4\,mm$, initialization : one small semi-disk of radius $1\,mm$ on the exterior tube wall.

2. Target shape : two semi-disks of radius $4\,mm$, initialization : one small semi-disk of radius $4\,mm$ on the exterior tube wall.

3. Target shape : two semi-disks of radius $4\,mm$, initialization : nine evenly spaced semi-circles of radius $1.33\,mm$ on the exterior tube wall.

Hereinafter is the optimal shape found by the algorithm for each initialization.

The first test shows that if the initialization is chosen poorly, here in an area where there is no target deposit, the gradient makes the initial deposit disappear as its signature on the impedance signal is not wanted.

The second test shows that a bigger initialization removes that problem as it converges towards the target. However, on Figure 4.0.8 we see that the optimal deposit has still one connected component. That is a consequence of the boundary conditions imposed on the gradient regularization equation : the deposit cannot penetrate the tube, therefore the r-component of the gradient has to be equal to zero on the tube wall. That condition imposes that component to decrease to zero close to the tube, which explains the thin layer of deposit between the two target shapes. Close to the tube, the gradient can only stretch the deposit.

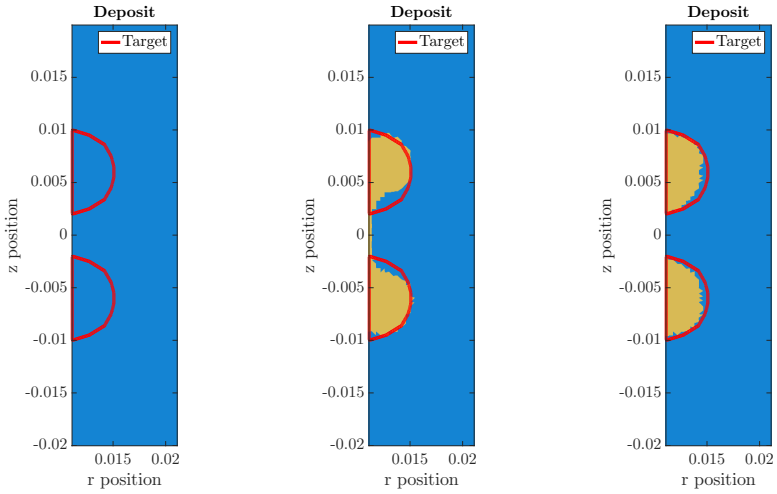


(a) Small semi-disk (7 iterations)

(b) Big semi-disk (14 iterations)

(c) Nine semi-disks (16 iterations)

Figure 4.0.8: Optimal shape (in yellow) computed by the reconstruction algorithm for different initializations. In red, the shape to reconstruct.

In conclusion, in order to cope with multiple connected components and to remain as general as possible (since we know nothing about the shape behind industrial signals), initializing the algorithm with nine semi-disks evenly spaced gives a good trade-off between fast convergence and reconstruction of the shape.

## Gradient regularization

As it was explained in last chapter, once the shape gradient is computed, to update the deposit shape we solve the Hamilton-Jacobi equation over a given time $\Delta t$ :

$$\partial_t \psi + V|\nabla \psi| = 0 \quad \text{in } D \tag{4.0.3}$$

where $V$ is the norm of the gradient. However it is known only on the shape boundary. Before solving the Hamilton-Jacobi, we first need to extend and regularize $\mathbf{V}$ by solving the following equation :

$$-\alpha \Delta \tilde{\mathbf{V}} + \tilde{\mathbf{V}} = -g\mathbf{n}\,\delta_{\partial\Omega_d}$$

where $\alpha$ is the regularization parameter we want to analyse. It needs to be small enough so that the regularized gradient is not too different from its actual value on the boundary and big enough to ensure regularity.

Below is the optimal shape found by the reconstruction algorithm for the elliptic target shape defined in the previous subsection, with the nine semi-disks initialization for different values of $\alpha$ :

For a value of order 1, the optimal shape displays some oscillations at its boundary that does not appear for a smaller value. For $\alpha \ll 1$, the gradient is little regularized which allows the algorithm to make high frequencies in the shape disappear. Conversely, for a value of order 1, the regularization prevents the gradient from dealing with high frequencies.

In conclusion, for the next cases, we consider $\alpha = 5 \cdot 10^{-7}$. Note that the low value comes from the size of the domain, which is at order $10^{-2}m$.

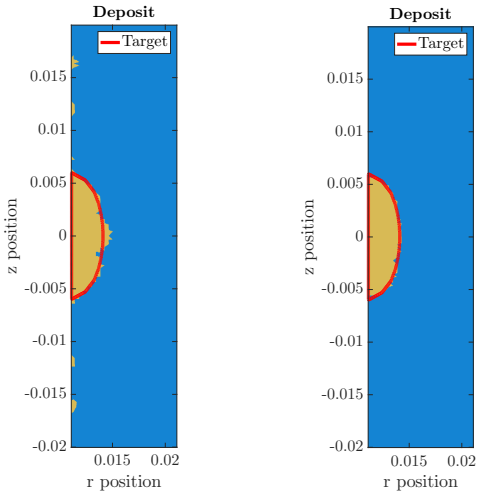


(a) $\alpha = 0.5$ (b) $\alpha = 5 \cdot 10^{-7}$

Figure 4.0.9: Optimal shape (in yellow) computed by the reconstruction algorithm for values of $\alpha$. In red, the shape to reconstruct.

## Impedance condition : field error

The aim is to compare the total field $E$ in a computational domain where the support plate is meshed to $E_{Pl}$, the solution of the problem with the impedance condition (plate excluded from the computation domain).

The plate has a magnetic permeability of $50\,\mu_0$ and a conductivity of $3 \cdot 10^6\, S \cdot m^{-1}$. Its inner radius is $0.01683\,m$ and its height, $0.03\,m$ (it will be centered around the origin). The impedance signal is computed for 71 coil positions. The mesh size of the computational domain for $E_{Pl}$ is fixed to $10^{-3}\,mm$ whereas it will vary for $E$.

Below are the relative error plots for the scattered field and the impedance signal. Figure 4.0.10 displays the relative L2-difference between the scattered field computed with impedance conditions on the plate boundary and the scattered field computed with the support plate meshed in the computational domain.

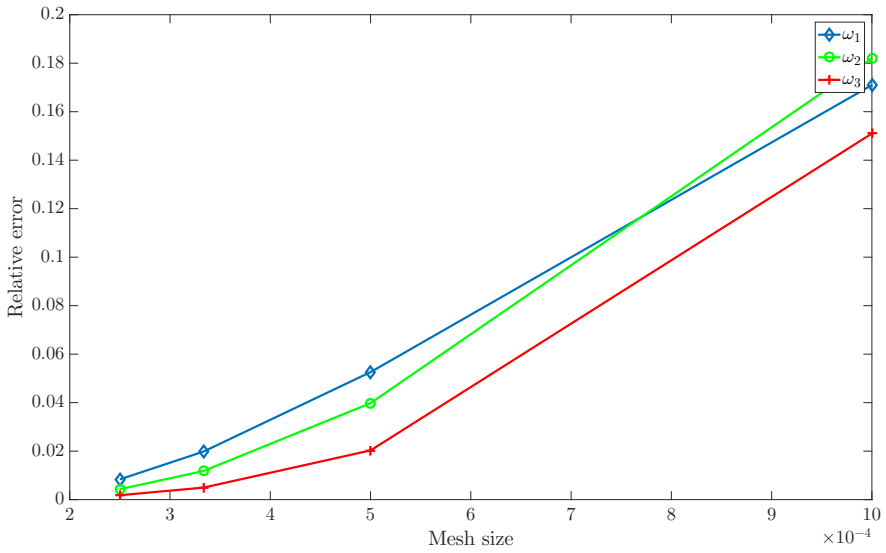


Figure 4.0.10: Relative error for the scattered field, for each pulsation

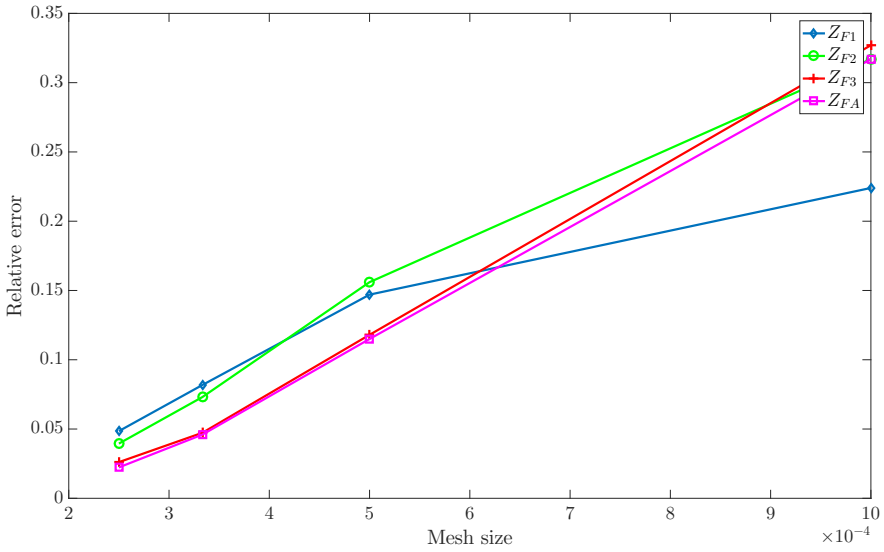


Figure 4.0.11: Relative error for the each impedance signal

For a given pulsation $\omega$, the skin depth inside the support plate is $\delta_p = 1/\sqrt{\omega\sigma_p\mu_p}$. Therefore, since $\omega_1 > \omega_2 > \omega_3$, the impedance condition is a better approximation for $\omega_3$. According to these plots, in order for the approximation to be satisfying, the mesh size needs to be small enough. That is because in order to capture the vanishing of the field inside the plate, the size of the mesh needs to be at least equal to the skin depth, which proves the asset of the impedance condition, as it requires a looser mesh.

## Initialization of the algorithm in presence of a support plate

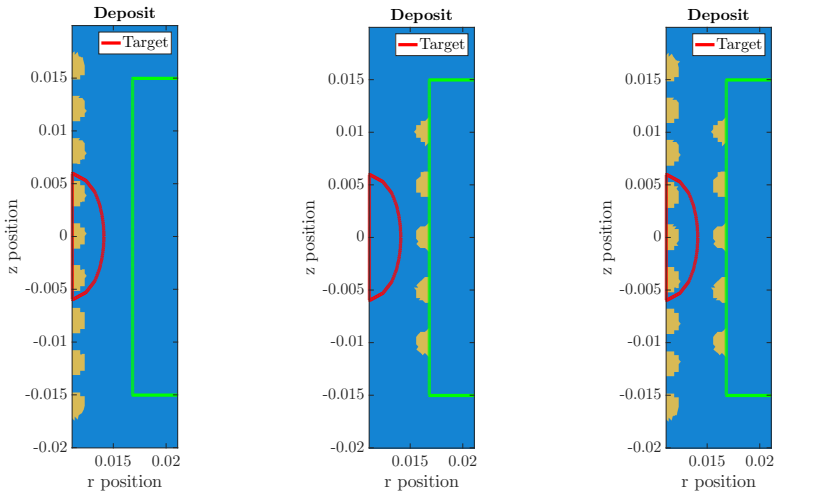


(a) Initialization on the tube wall

(b) Initialization on the support plate

(c) Mixed initialization

Figure 4.0.12: Different initializations (in yellow) of the reconstruction algorithm. In red, the shape to reconstruct and in green, the plate boundary.

Considering the generic initialization we chose at the beginning, what changes brings the presence of a plate ? In order to discuss that point, we consider the following tests (where the impedance signal is given for 81 coil positions) :

1. Target shape : semi-ellipse of radii 3 $mm$ and 6 $mm$ on the tube wall, initialization : nine evenly spaced semi-circles of radius 1.33 $mm$ on the tube wall.
2. Target shape : semi-ellipse of radii 3 $mm$ and 6 $mm$ on the tube wall, initialization : five evenly spaced semi-circles of radius 1.33 $mm$ on the tube wall.
3. Target shape : semi-ellipse of radii 3 $mm$ and 6 $mm$ on the tube wall, initialization : a combination of the first two initializations

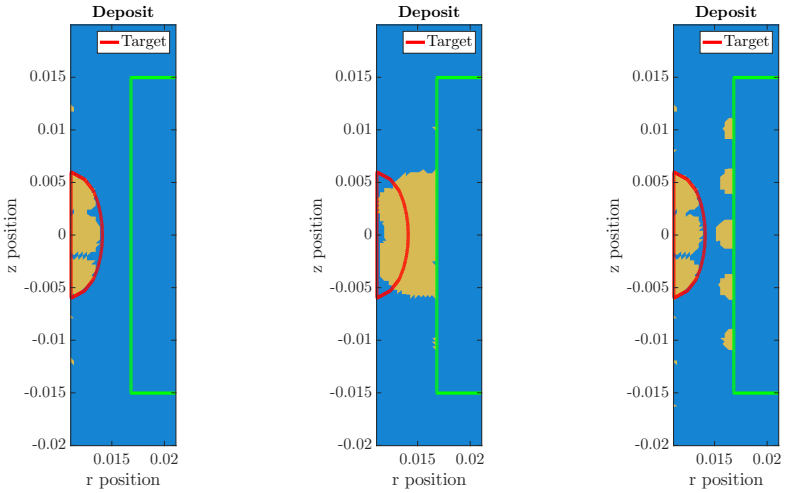


(a) Initialization on the tube wall (5 iterations)

(b) Initialization on the support plate (12 iterations)

(c) Mixed initialization (5 iterations)

Figure 4.0.13: Optimal shape (in yellow) computed by the reconstruction algorithm for different initializations. In red, the shape to reconstruct.

Figure 4.0.13 shows the optimal shape found by the algorithm for each initialization.

Whereas the first initialization converges towards the target, the last initialization demonstrates that the deposits on the support plate have a far smaller impedance signature than the deposits on the tube wall. This is a consequence of the vanishing of the field inside a conductive material (here the deposit), which explains the optimal solution found by the algorithm : the signal can be explained using only the deposits on the tube wall, those on the support plate induce insignificant perturbation.

The second initialization corroborates that observation : in order to explain the signal created by a deposit on the tube wall, the deposit on the support plate needs to expand until it reaches the tube wall. Note that because we impose the $r$-component of the gradient null on the tube and the plate, the deposit can neither leave the plate nor glue the tube.

## Perimeter penalization

In Figure 4.0.13a, the algorithm converged to an optimal shape close to the target shape. The differences are due to the ill-conditionned inverse problem : several different optimal shapes can fit with same precision the data.

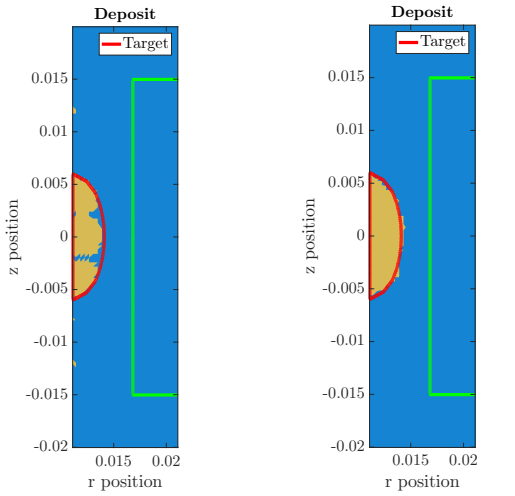


(a) Without perimeter penalization (5 iterations)

(b) With perimeter penalization (19 iterations)

Figure 4.0.14: Optimal shape (in yellow) computed by the reconstruction algorithm with or without perimeter penalization. In red, the shape to reconstruct.

On Figure 4.0.14 are the results for the following test case : an elliptic target shape on the tube wall and an initialization of nine semi-disks on the tube wall. For this case, $\lambda = 10$ empirically.

Both the algorithms converged to an optimum. With the penalization, to reach the same cost level than without it more iterations are required, as one can expect (cf Figure 4.0.15 and 4.0.16). The resulting tradeoff is a better shape at the end.

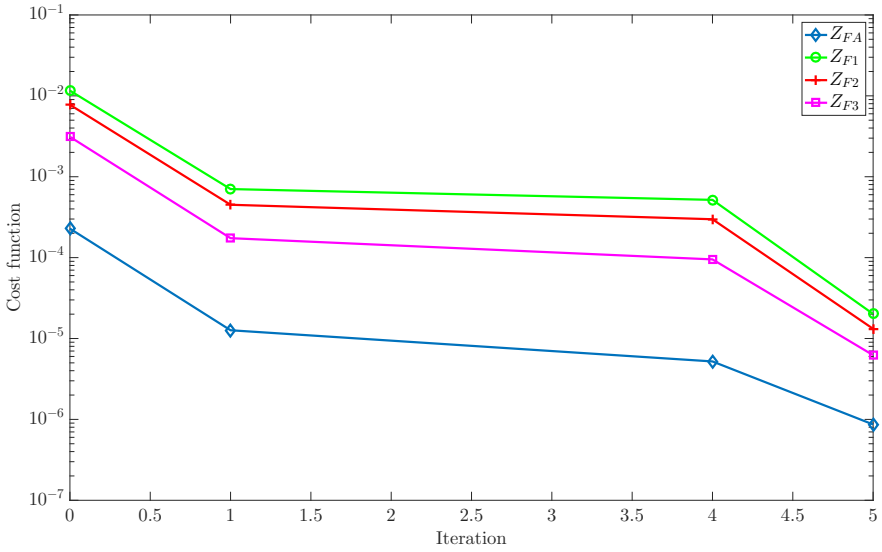


Figure 4.0.15: Evolution of the cost function, without perimeter penalization (5 iterations)

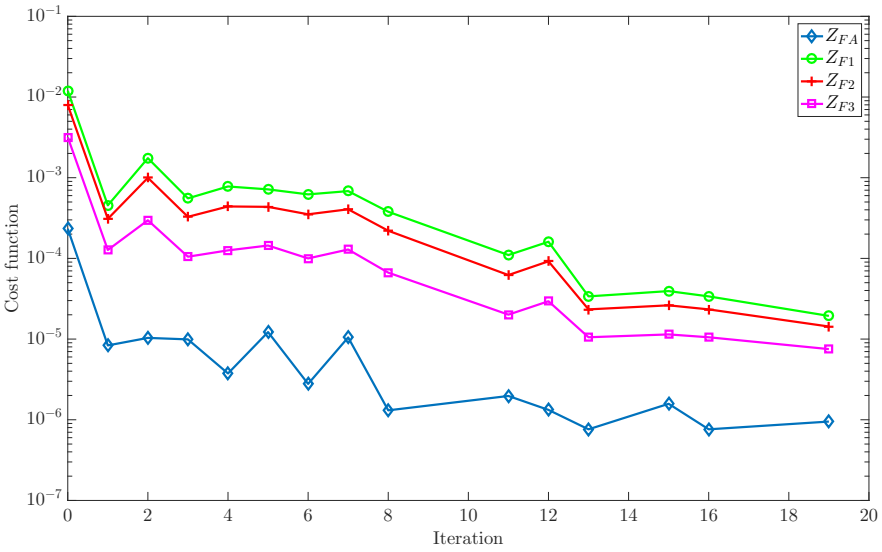


Figure 4.0.16: Evolution of the cost function, with perimeter penalization (19 iterations)

In addition to making the optimal shape smoother, the perimeter penalization is also a means to reduce the variability of the optimization problem. For completely different initializations, the constraint leads to optimal shapes that are less different.

For instance, on Figure 4.0.17, we initialized the algorithm with three rows of nine circles. On the left is the result presented before, on the right is the result obtained with perimeter penalization. The constraint forces the algorithm to converge towards a solution with the lowest perimeter, hence suppressing the small circles.

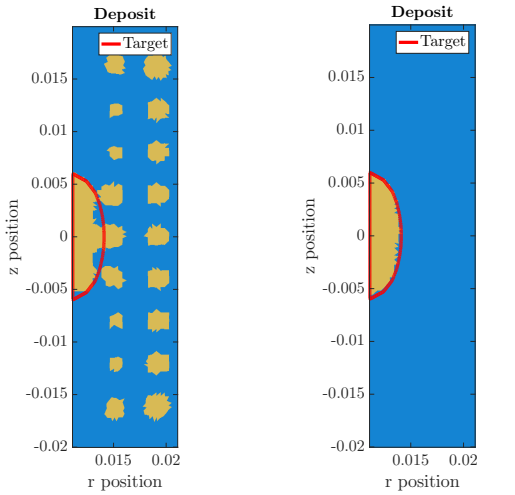


(a) Without perimeter penalization (17 iterations)

(b) With perimeter penalization (34 iterations)

Figure 4.0.17: Optimal shape (in yellow) computed by the reconstruction algorithm with or without perimeter penalization. In red, the shape to reconstruct.

## Asymptotic models : field error

### Tube thickness variation

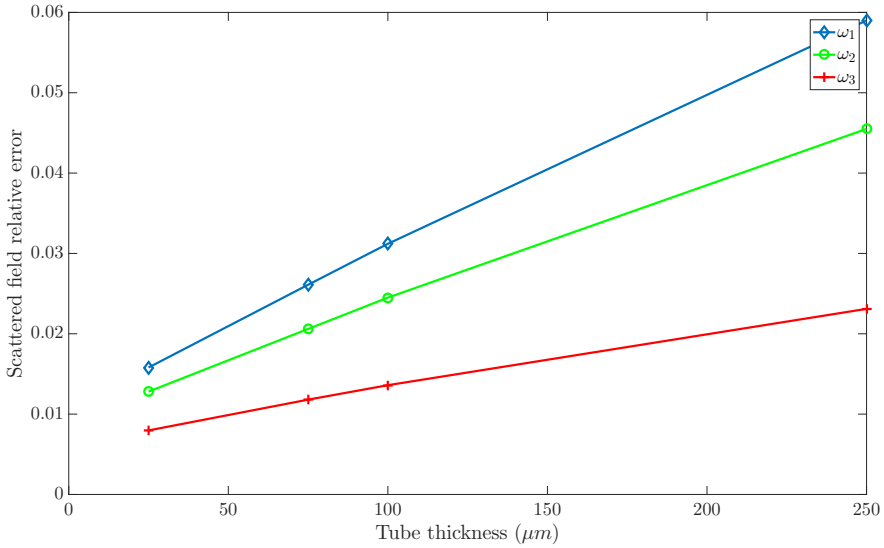


Figure 4.0.18: Relative error for the scattered field, for each pulsation

The aim is to compare the scattered field $E$ in a computational domain where the tube thickness variation is meshed to $E_{Tube}$, the solution of the problem with the asymptotic transmission condition on the straight tube wall, as well as the resulting impedances.

We consider the following test case for the error plots : no volumetric deposit and an elliptic tube excess, that is to say $f_t(z) = \delta_t\sqrt{1-(z/z_t)^2}, \forall z \in [-z_t, z_t]$, where the maximum thickness $\delta_t$ varies between $25\mu m$ and $250\mu m$ and $z_t = 0.010m$. The mesh size of the computational domain for $E_{Tube}$ is fixed to $10^{-3}\,mm$ and $4 \cdot 10^{-3} mm$ for $E$. Above is the relative error plot for the different different pulsations.

Below is the same error plot for the resulting different impedance signals.

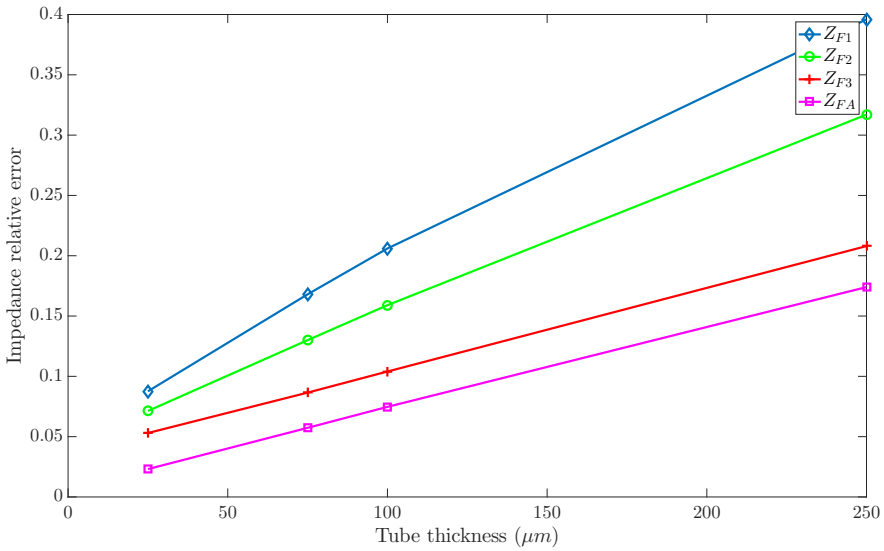


Figure 4.0.19: Relative error for the each impedance signal

According to these plots, in order for the approximation to be satisfying, the maximum thickness to pick

would be $50\mu m$, above even though the scattered field remains satisfying, the impedance signals are too different.

### Thin clogging deposit

The aim is to compare the total field $E$ in a computational domain where a thin clogging deposit is meshed to $E_{Thin}$, the solution of the problem with the asymptotic transmission condition on the straight tube wall, as well as the resulting impedances.

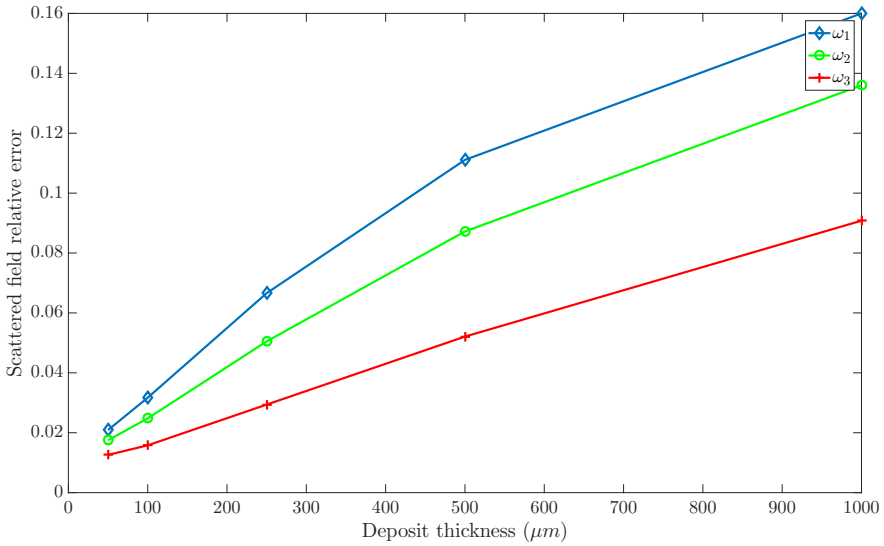


Figure 4.0.20: Relative error for the scattered field, for each pulsation

We consider the following test case for the error plots : no volumetric deposit and a thin clogging deposit, of a thickness $\delta_d$ varying from $50\mu m$ to $1000\mu m$. The impedance signal is computed for 71 coil positions. The mesh size of the computational domain for $E_{Thin}$ is fixed to $10^{-3}\,mm$ and $4 \cdot 10^{-3}$ for $E$. Below is the relative error plots for the scattered field.

Below is the same error plot for the resulting different impedance signals.

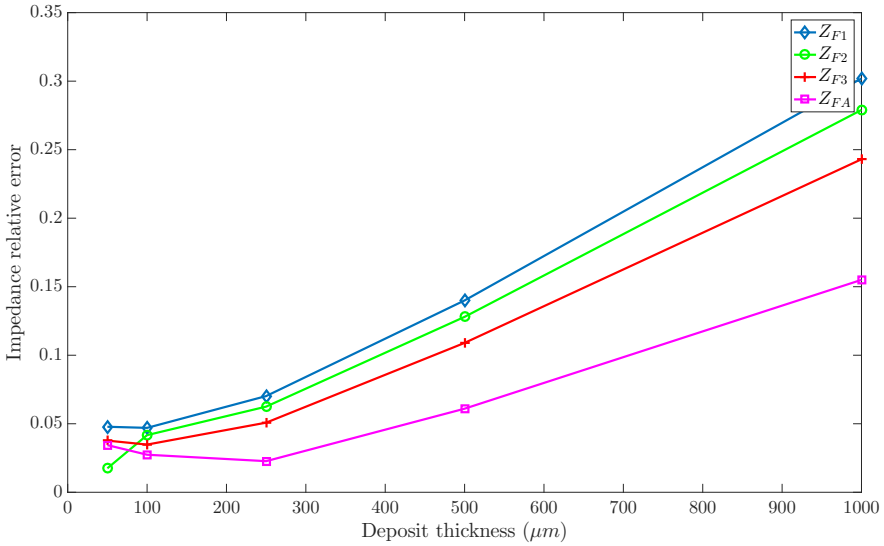


Figure 4.0.21: Relative error for the each impedance signal

According to these plots, in order for the approximation to be satisfying, the maximum thickness to pick would be $250\mu m$, above even though the scattered field remains satisfying, the impedance signals are too different.

**Inversion with tube thickness variation**

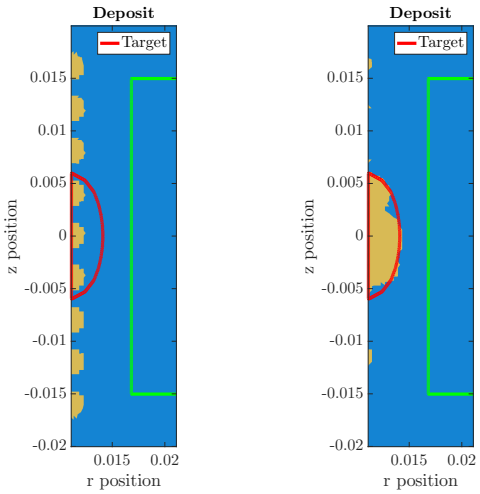


(a) Shape initialization (b) Optimal shape

Figure 4.0.22: Optimal solution (13 iterations) for a shape optimization with tube thickness variation.

We consider the following test case : the target configuration is an elliptic deposit on the tube wall, with an sinusoïdal tube thickness variation, of maximum thickness $25\mu m$. The shape optimization is initialized with nine semi-disks on the tube wall, the tube optimization with the null function.

In order to simplify the optimization problem, we assumed that the optimal thickness function $f_d^*$ was non zero in a chosen region of interest (namely, in the area around the support plate). Therefore, the following constraint is added : $f_d(z) = 0, \forall z \in ]-\infty, z_1] \cup [z_2, +\infty[$, where $z_2 = -z_1 = 0.020m$. Numerically, that constraint is taken into account using a projected gradient method.

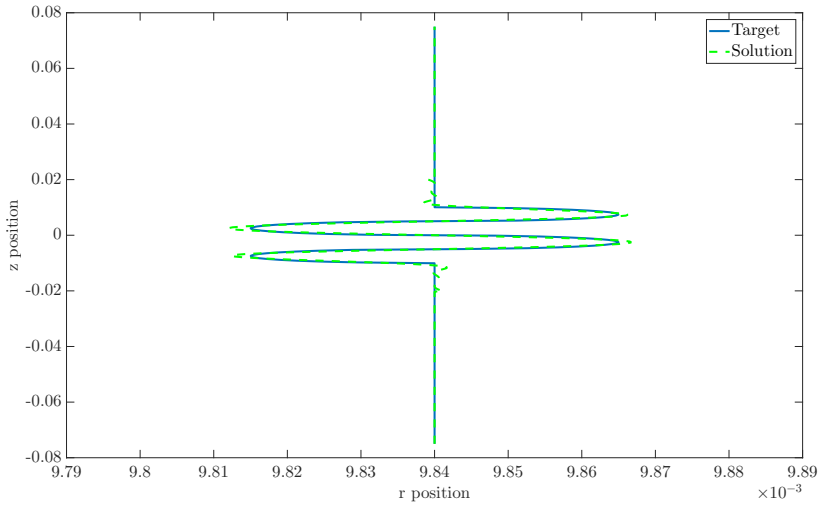


Figure 4.0.23: Optimal tube thickness (13 iterations) for a shape optimization with tube thickness variation.

On Figure 4.0.23, the optimal thickness function displays some high frequencies around the sudden variations. In order to remove that unwanted behavior, other constraints could be added to the thickness optimization problem.

The convergence of the shape is different from what we observed before : it would seem that the addition of a second variable to the algorithm leads to a different convergence. That is mainly caused by the fact that, in order to explain the same variation in the signal, we have two different levers.

### Inversion with thin clogging deposits

Clogging deposits appear outside of the support plate area. Therefore, we consider the following test case : the target configuration is an elliptic deposit on the tube wall, with two clogging deposits, above and below the support plate, of constant thickness $100\mu m$.

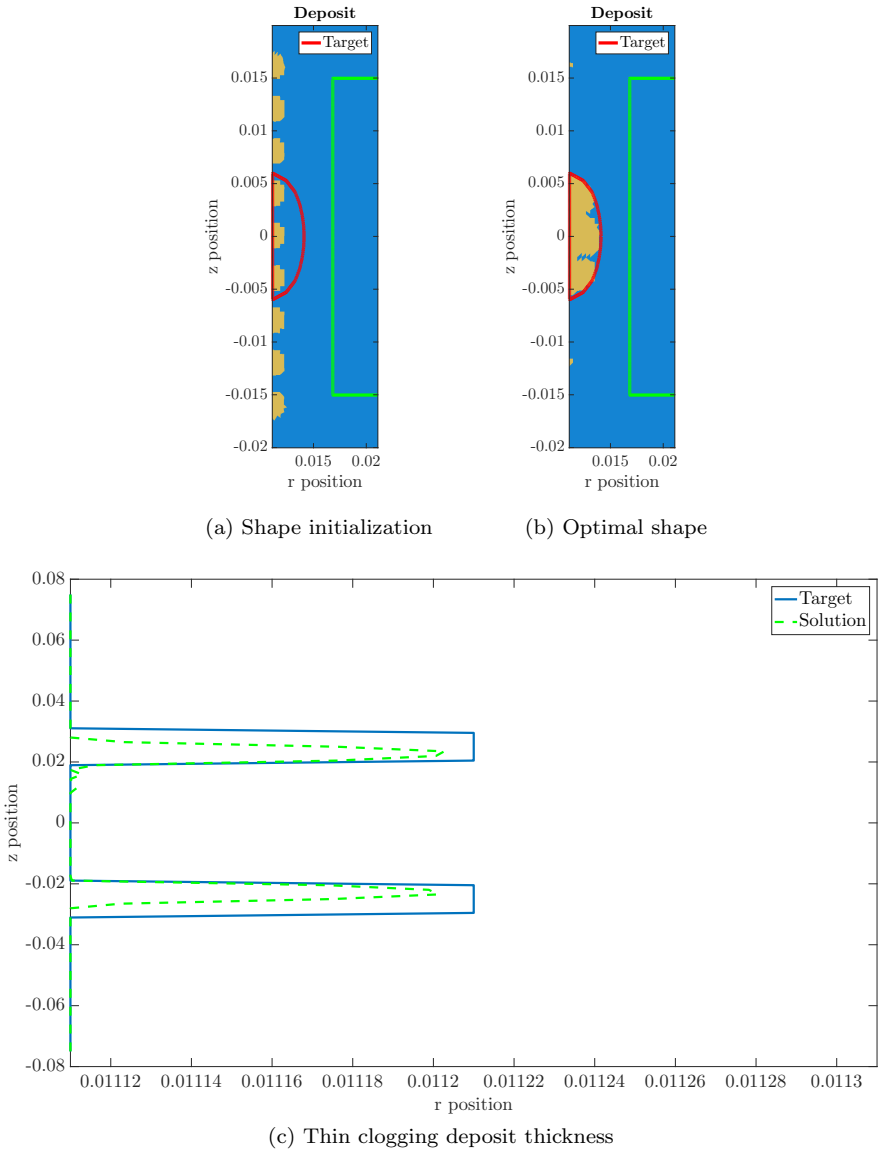


(a) Shape initialization (b) Optimal shape

(c) Thin clogging deposit thickness

Figure 4.0.24: Optimal solution (12 iterations) for a shape optimization problem with thin clogging deposits

Similarly to the tube thickness variation, we assumed that the clogging deposit could only form in a given area : $f_t(z) = 0, \forall z \in ]-\infty, z_3] \cup [z_4, +\infty[$, where $z_4 = -z_3 = 0.010m$. We add to that a second constraint,

as the thickness function can not be negative (the deposit has to be outside the tube wall.

Note that like the tube thickness variation case, another constraint could be added to the problem in order to remove the high frequencies in the optimal solution.

## Noise sensibility

As showed in previous subsections, the inverse algorithm converges on synthetic data computed without the asymptotical models or the impedance condition. However, due to various uncertainties during the industrial detection process, the actual impedance signals present noise. Therefore, to asses the robustness of our algorithm, it is important to test its response to various noises.

We consider here four different noises, modeling the different uncertainties that might be faced in industrial signals :

- Uncertainty in the coil position : during the detection process, the coils are being pulled alongside the tube at a constant speed. At regular heights $z$, they make an impedance measurement. However, as the speed is not constant in reality, there is a slight noise in the coil position.
- Uncertainty in the impedance signal, which corresponds to noise in the signal.
- Uncertainty in the tube thickness, which has been taken into account with an asymptotic model. However, we want here to see how the algorithm converges in presence of a tube thickness variation when we only reconstruct the deposit shape.

For each case, we consider the shape to reconstruct to be a semi-ellipse semi-ellipse of radii $3\,mm$ and $6\,mm$ and the initialization, nine semi-disks. We run the algorithm for different noise levels in order to see its response.

Next page are the results for different noise level.

Based on the following plots, it seems that our algorithm is robust towards noise created by either the coil position or the white noise in the signal. When looking at the fitting plots, it appears that the algorithm doesn't see the noise and does not try to fit every small variation.

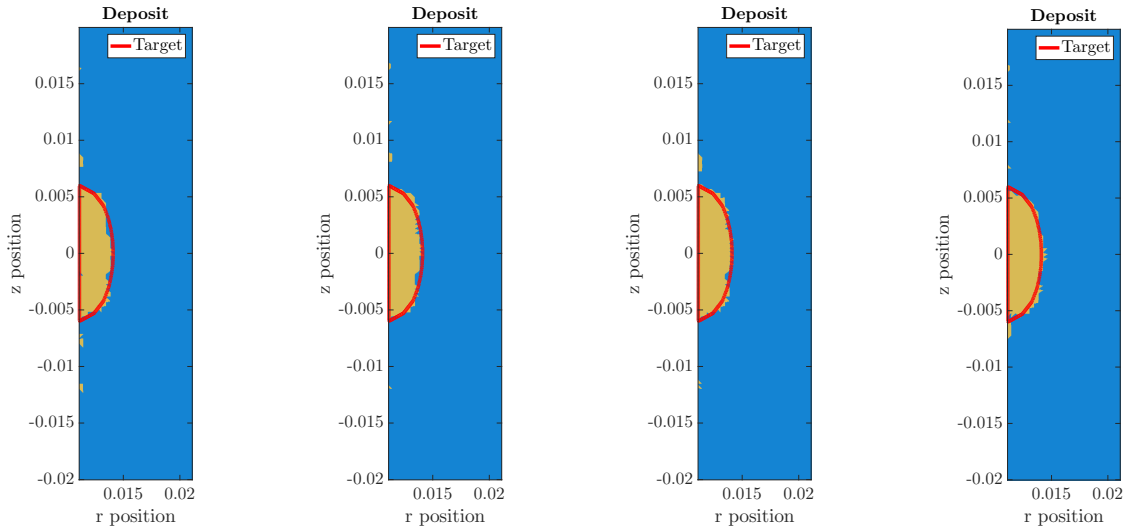


(a) Noise level 1% (b) Noise level 5% (c) Noise level 10% (d) Noise level 20%

Figure 4.0.25: Optimal solution for a shape optimization problem with different coil position noise level.

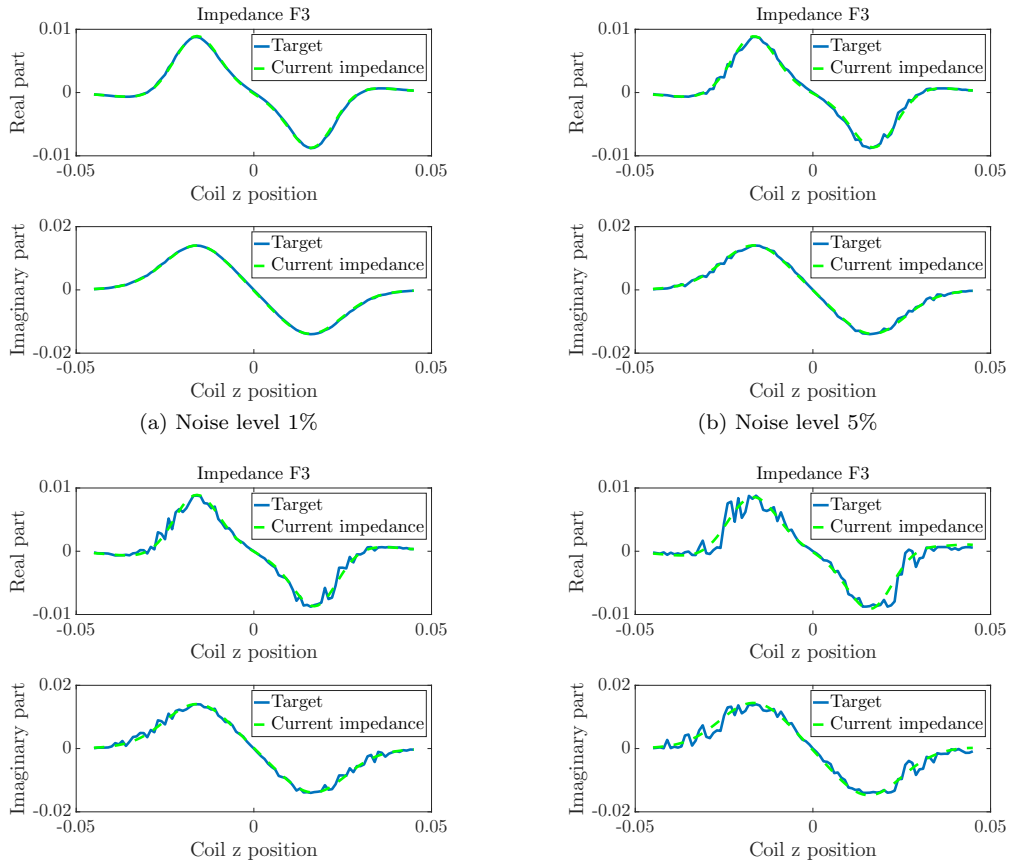


(a) Noise level 1%

(b) Noise level 5%

(c) Noise level 10%

(d) Noise level 20%

Figure 4.0.26: Data fitting for $Z_{F3}$ for a shape optimization problem with different coil position noise level.

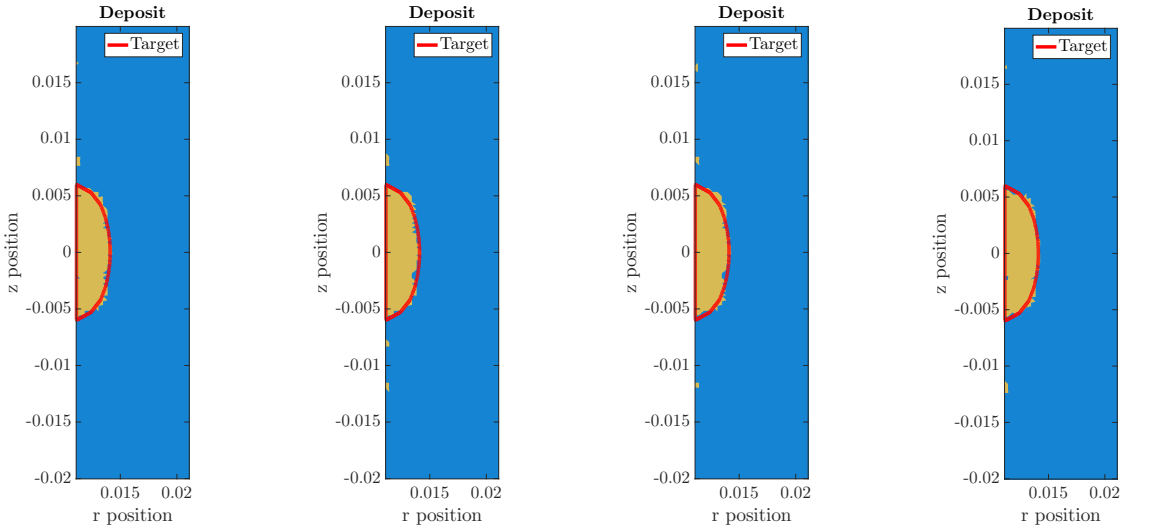


(a) Noise level 1%

(b) Noise level 5%

(c) Noise level 10%

(d) Noise level 20%

Figure 4.0.27: Optimal solution for a shape optimization problem with different data noise level.

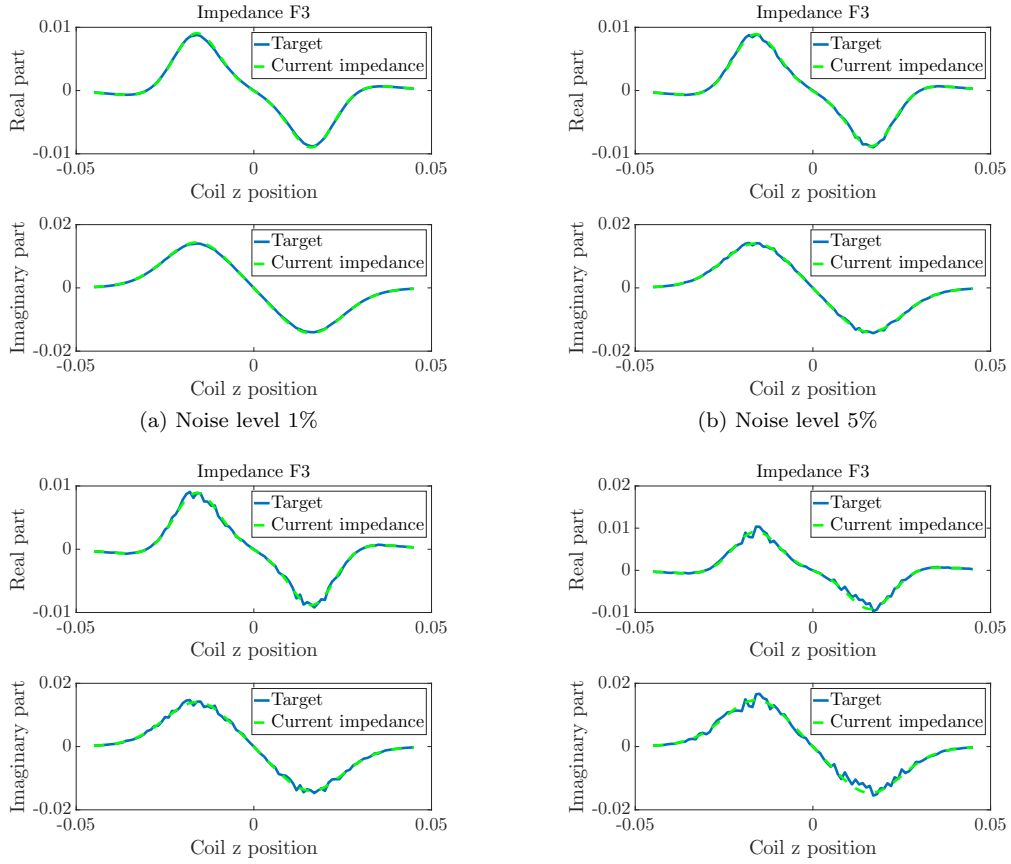


(a) Noise level 1%

(b) Noise level 5%

(c) Noise level 10%

(d) Noise level 20%

Figure 4.0.28: Data fitting for $Z_{F3}$ for a shape optimization problem with different data noise level.

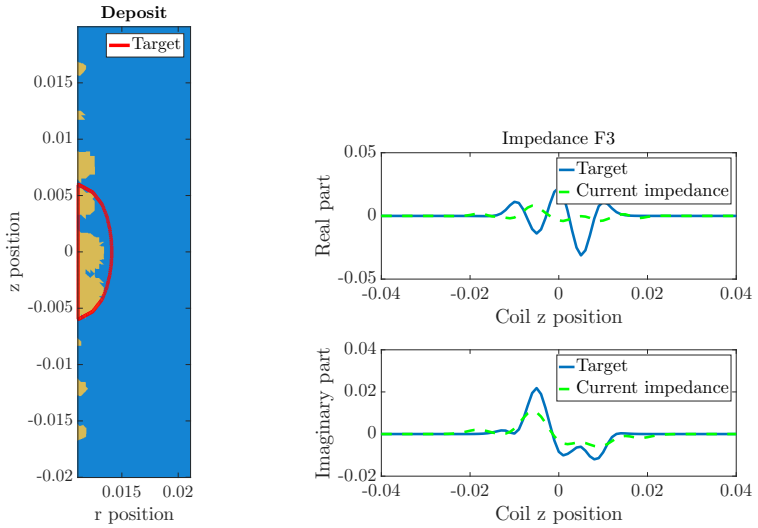


(a) Optimal shape

(b) Data fitting for $Z_{F3}$

Figure 4.0.29: Test case with an elliptic tube variation of maximum thickness $5\mu m$ as noise.

## Inversion of industrial signals

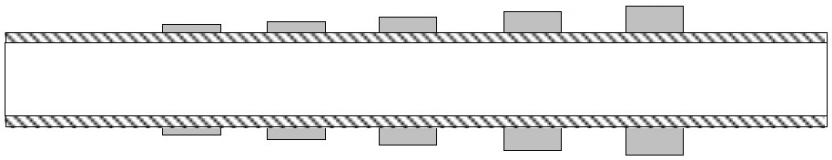

Figure 4.0.30: Configuration of the mock-up. Source : EDF.

In this subsection, we focus on the inversion of signals provided by EDF. The test case is the following : on a conductive mock-up tube, five annular deposits of known dimensions are located on its exterior wall ($0.1mm$, $0.2mm$, $0.3mm$, $0.5mm$ and $1mm$ of thickness, $28mm$ in length). There is here no support plate and the tube wall is supposed to be straight. The aim is to reconstruct the volumetric deposits. Note that the physical properties of the deposits $(\mu, \sigma)$ are unknown.

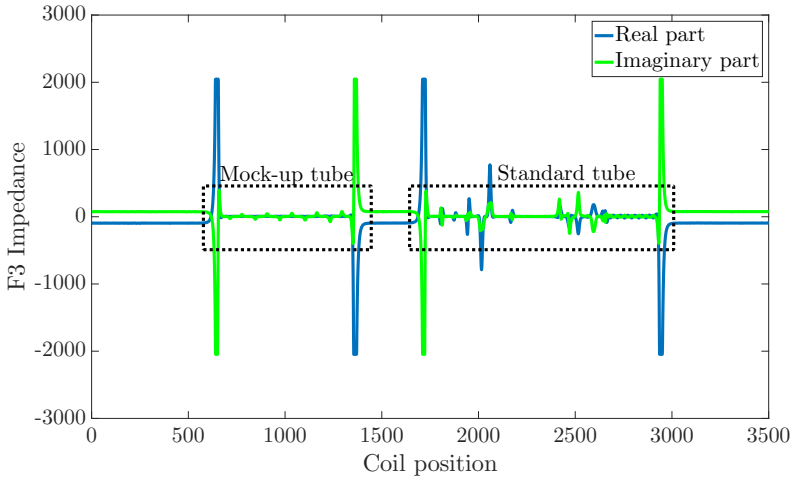


Figure 4.0.31: $Z_{F3}$ signal of the above mock-up configuration. Source : EDF.

The detection process is the following : the probe is inserted at one end of the tube and is pulled at a constant speed. Measurements are computed at given $z$ positions. It then goes through a standard tube with known defaults in order to calibrate (i.e. apply a transformation $\kappa e^{i\phi}$) the signal for post-processing purposes. That leads to the signal on Figure 4.0.31.

As the signal provided has been post-processed, we first need to apply the reverse transformation before inverting the signal (normalisation step). Using the standard tube dimensions, we are able to simulate the resulting impedances. By comparing the simulated impedances to the data, we obtain the transformation $\kappa e^{i\phi}$ to apply to the deposit signal. That leads to the signal on Figure 4.0.32.

Once the data renormalized, we need to reconstruct the physical properties $(\mu, \sigma)$ of the deposits, which are considered unknown. As the shape of the deposit is known, the reconstruction algorithm defined in Subsection 3.4 is computed for a fixed shape. To reduce the computational time, we only consider here the signal corresponding to the 1mm-thickness deposit.

Below are the fitting plots obtained for the optimal physical parameters. Imprecisions on the shape (non constant thickness, wrong length, ...) and presence of noise during the measurements can explain why the data fitting can not be better than this. Conversely, this gives us a good infimum for the fitting error in the shape reconstruction algorithm.

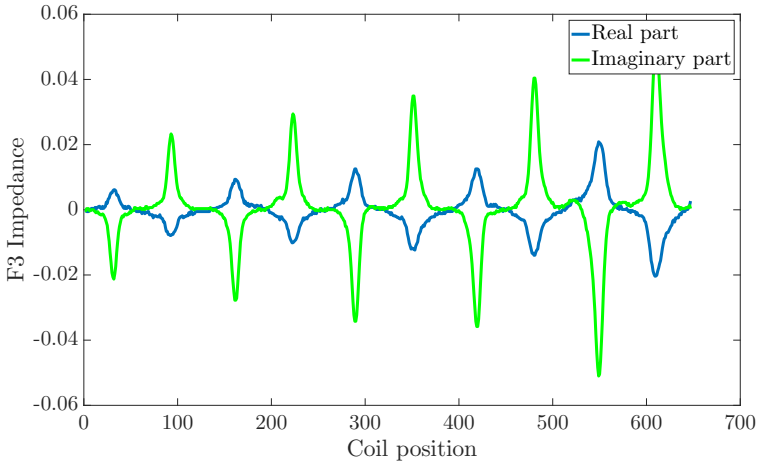


Figure 4.0.32: $Z_{F3}$ signal of the deposits after normalisation. Source : EDF.

As for the shape reconstruction algorithm, a consideration needs to be made beforehand : the deposits in the signal have a length that is at least 10 times greater than their thickness. Due to the boundary condition we impose on the shape gradient regularization, for a thickness small enough, the algorithm is bound to fail converging (as the gradient becomes null close to the tube wall).

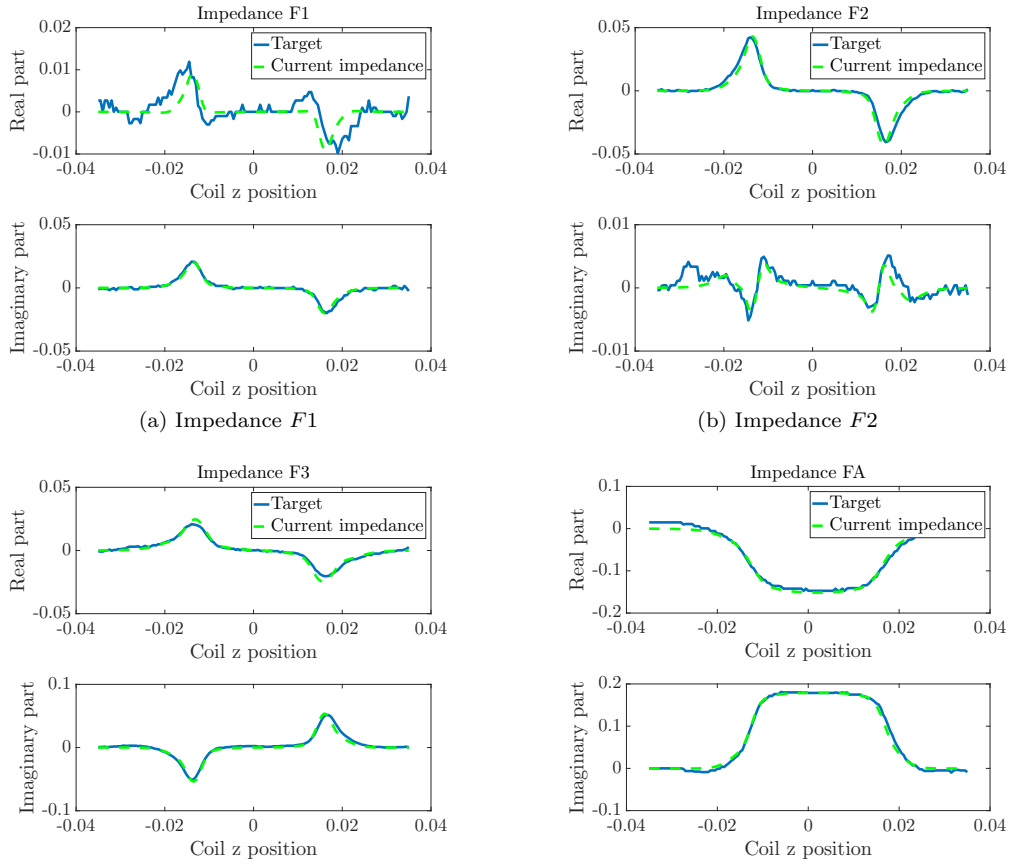


(a) Impedance $F1$

(b) Impedance $F2$

(c) Impedance $F3$

(d) Impedance $FA$

Figure 4.0.33: Data fitting for the impedance signals for the optimal $\mu$ and $\sigma$.

Once $\sigma$ and $\mu$ are retrieved, we move on to shape optimization.

Before showing actual results, an important remark needs to be done. In the course of the inversion of the different deposits, we observed that the algorithm as it is does not allow convergence on thicknesses lower than $1mm$. The reason behind that is the degenerate shape : while the thickness is quite small (less than a millimeter), the length in contrary is about $28mm$.

Therefore, due to the boundary condition imposed on the regularization of the shape gradient, that is to say its normal direction at the tube's wall is null, it is numerically impossible for the algorithm to decrease the level-set function to the actual thickness.

The next idea would be to use the asymptotical model for thin deposits to reconstruct the thicknesses lower than the millimeter, however that requires new calculations as we assumed in that model $\mu$ to be that of the vacuum. Therefore, we focus in the following on the reconstruction of the deposits of thickness $1mm$. This means the signal considered here is the rightmost on Figure 4.0.31. It is made out of 141 coil positions.

On Figure 4.0.34 are the optimal shapes found by the algorithm with or without perimeter penalization, because we observed that without penalization, even though the data fitting was satisfying, the optimal shape barely moved in the course of the iterations. What has been said above still holds true : due to the thin layer of deposit and the gradient regularization, the algorithm can only move the shapes in the area of the target shape, but it can hardly reduce their thickness.

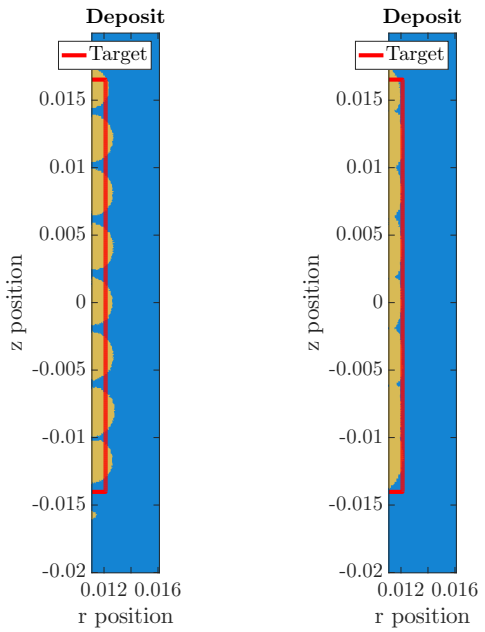


(a) Without penalization (15 iterations)

(b) With penalization (24 iterations)

Figure 4.0.34: Optimal solutions with or without perimeter penalization for the inversion of industrial signals

On the contrary, by adding perimeter penalization, we are able to actually merge the different shapes from the initialization. Once again, adding the constraint increases the number of iterations but neither the optimal cost function or the data fitting as it can be seen on Figure 4.0.35. On Figure 4.0.36 is the resulting data fitting for the optimal shape with perimeter penalization.

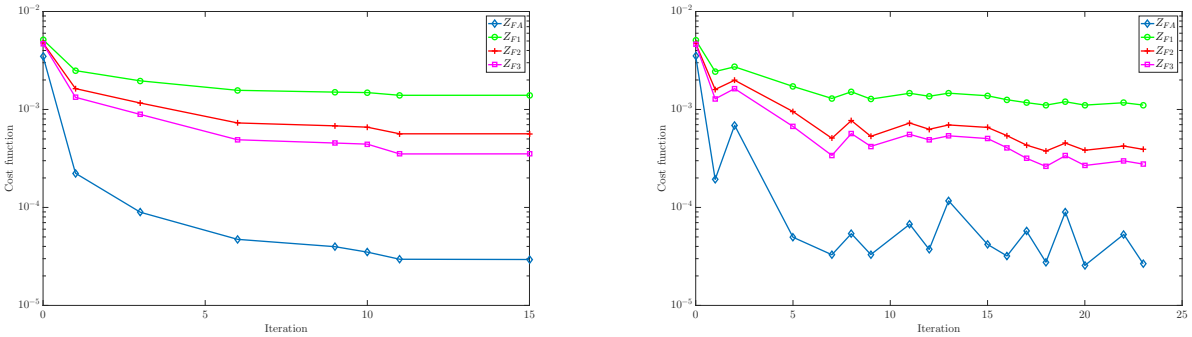


(a) Without penalization (15 iterations)

(b) With penalization (24 iterations)

Figure 4.0.35: Evolution of the cost function with or without perimeter penalization for the inversion of industrial signals

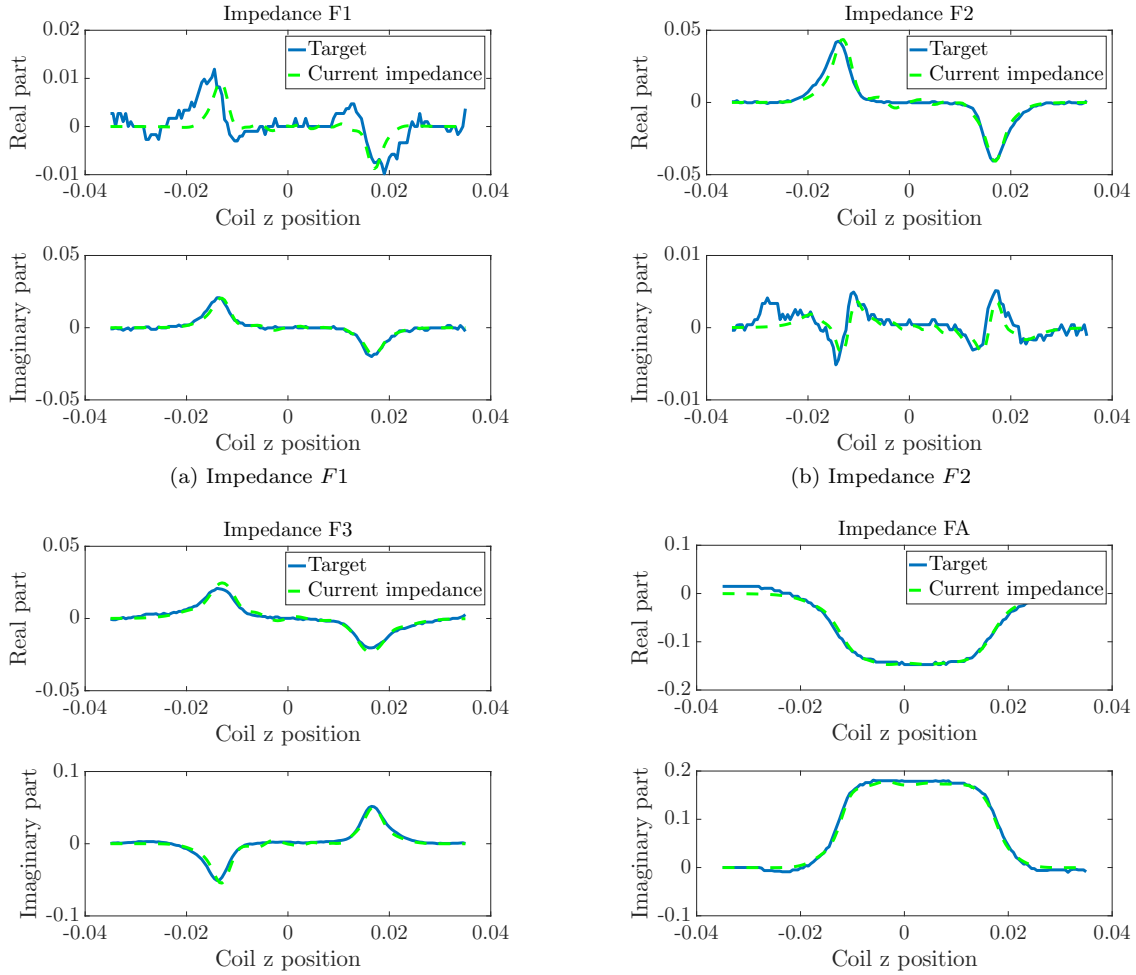


(a) Impedance $F1$

(b) Impedance $F2$

(c) Impedance $F3$

(d) Impedance $FA$

Figure 4.0.36: Data fitting for the impedance signals for the shape optimization problem with perimeter penalization (24 iterations).

# 5 Perspectives

Different trails have been considered in order to improve the 2D axisymmetric inversion algorithm.

Considering that the different impedance signals that are available give different information about the deposit shape, multi-criteria optimization may improve the convergence rate as depending on the configuration of the domain, some signals may see not see the defects. For now, we chose to optimize the same cost function for any configuration that is the weighted sum with weights of 1/4 of the four signals.

For the different optimization methods, different improvements can be made to enhance the performances. In the case of asymptotical models, as the problem is a usual one, adding a total variation like constraint should help removing the high frequencies in the optimal solution. However, shape optimization is trickier : one approach to be tested is the transposition of the Nesterov acceleration to shape optimization. The main issue to that method is that it needs to combine the solutions at two different iterations where the solutions are shapes. We thought of combining the underlying level-sets instead, but it has yet to be tested.

This preliminary study of the 2D-axisymmetric has the main purpose of preparing the 3D algorithm : using the functioning 2D algorithm, we will be able to determine if the 3D model and algorithm work. Moreover, in a first step, results from the 2D model (calculation of the incident field and/or the impedance signals) can be re-used for an 3D-axisymmetric domain. The final aim is then to move to a generic non axisymmetric domain. We are currently working on the first step of the 3D problem.

Parallel programming is also slowly being added to the 2D-axisymmetric and 3D problem. The main point that can be improved is the resolution of Finite Elements problems : at each coil position, we solve different Finite Elements problems where the right-hand side is the only part that changes. This motivates us to replace $N_P$ solve operations (where $N_P$ is the number of coil positions) by one where the right-hand side would be a rectangular matrix with $N_P$ columns. This motivates us to use PETSc as it offers a solver implementing this method. The second step currently at work now is to add domain decomposition to the algorithm.

# References

[1] Jiang Z., *Some inversion methods applied to non-destructive testings of steam generator via eddy current probe*, PhD thesis, École Polytechnique (2014).

[2] Allaire G., De Gournay F., Jouve F., Toader A.-M., Structural optimization using topological and shape sensitivity via a level set method, *Control and Cybernetics*, **34**(1):59-80, 2004.

[3] Auld, B. A. and Moulder, J. C., Review of Advances in Quantitative Eddy Current Nondestructive Evaluation, *Journal of Nondestructive Evaluation*, **18**(1):3-36, 1999.

[4] Assous F., Ciarlet P., Labrunie S., Theoretical tools to solve the axisymmetric Maxwell equations, *Mathematical methods in the applied sciences*, **25**:49-78, 2002.

[5] Henrot A., Pierre M., *Variation et optimisation de formes. Une analyse géom'etrique*, Springer, 2005.

[6] Hecht F., New development in FreeFem++, *Journal of numerical mathematics*, **20**(3-4):251-266, 2012.

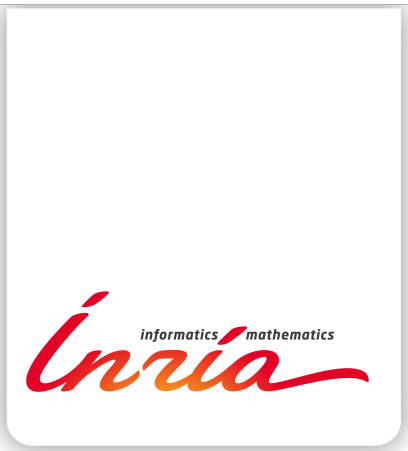


**RESEARCH CENTRE**
**SACLAY – ÎLE-DE-FRANCE**

1 rue Honoré d'Estienne d'Orves
Bâtiment Alan Turing
Campus de l'École Polytechnique

Publisher
Inria
Domaine de Voluceau - Rocquencourt
BP 105 - 78153 Le Chesnay Cedex
inria.fr

ISSN 0249-6399